Self-consistent Dust Modelling in Brown Dwarfs

Dissertation
zur Erlangung des Doktorgrades
des Fachbereichs Physik
der Universität Hamburg

vorgelegt von
Matthias Dehn
aus Reinbek

Hamburg
2007

Gutachter der Dissertation:	**Prof. Dr. Peter Hauschildt** **Dr. habil. Christiane Helling**
Gutachter der Disputation:	**Prof. Dr. Peter Hauschildt** **Prof. Dr. Jürgen Schmitt**
Datum der Disputation:	**16. März 2007**
Vorsitzender des Prüfungsausschusses:	**Prof. Dr. Günter Wiedemann**
Vorsitzender des Promotionsausschusses:	**Prof. Dr. Günter Huber**
Dekan der MIN-Fakultät:	**Prof. Dr. Arno Frühwald**
Departmentleiter:	**Prof. Dr. Robert Klanner**

Zusammenfassung

In aktuellen Staubmodellen, wird oft angenommen, daß ein Phasengleichgewicht bei der Staubbildung vorherrscht. Diese Bildung der Kondensate führt zu einer Abnahme von Elementhäufigkeiten. Diese Modelle wurden bisher erfolgreich bei der Berechnung von Opazitäten zur Lösung des Strahlungstransportproblems benutzt (z.B. Allard et al. (2001); Burrows et al. (2002); Marley et al. (2002); Tsuji (2002)).
In einer detaillierteren, selbstkonsistenten Behandlung des quasistatischen Staubproblems, die einem kinetischen Ansatz zugrunde liegt, wird hingegen ein chemisches Gleichgewicht angenommen und die Keimbildung von TiO_2-Partikeln, das heterogene Wachstum der Teilchen und dessen Bewegung durch die Gravitationskraft berücksichtigt (Woitke & Helling, 2004).
In diesen Modellen wurde der Einfluss des Staubes auf die Atmosphärenstruktur bislang vernachlässigt. Das Problem der Kopplung von Staubbildung und dessen Einfluß auf das Strahlungsfeld und das Energiegleichgewicht konnte in dieser Arbeit iterativ mit dem Atmosphärencode PHOENIX (Hauschildt & Baron, 1999) gelöst werden. PHOENIX löst das frequenzabhängige Strahlungstranportproblem und die Atmosphärenstruktur unter Annahme des hydrostatischen Gleichgewichts.
Das selbstkonsistente Staubmodell von Woitke & Helling (2003, 2004) und Helling & Woitke (2006) für sauerstoffreiche Zwerge nutzt die erhaltene Atmosphärenstruktur und berechnet die Eigenschaften des Staubes und dessen Opazitäten für die Lösung des Strahlungstransportproblems. In dieser Arbeit werden Atmosphären mit Staubteilchen bestehend aus TiO_2, Mg_2SiO_4, SiO_2, Fe, Al_2O_3, MgO, und $MgSiO_3$ für Effektivtemperaturen von 1500 bis 3000 K (entspricht Objekten des Spektraltyps M und L) präsentiert.
Die erhaltenen Eigenschaften des Staubes können vollständig durch dessen Keimbildungsrate, der Wachstumsgeschwindigkeit der Staubkörner, ihrer Driftgeschwindigkeit und durch die konvektive Mischung erklärt werden. Staubbildung tritt unterhalb von $T_{\rm eff} = 2800$ K auf und die Wolken werden ab $T_{\rm eff} \lesssim 2000$ K optisch dick. Staubteilchendichten erreichen Größenordnungen von bis zu 200 $\rm cm^{-3}$ und deren maximaler Radius erreicht Größen von $1.0 \pm 0.5\,\mu$m. In vorherigen Modellen, in denen das Strahlungsfeld nicht berücksichtigt wurde, erreichten die maximalen Radien Werte von bis zu $90\,\mu$m (Woitke & Helling, 2004). Die oberste Begrenzung einer Staubwolke wurde beim außen gelegenen Maximum der Keimbildungsrate definiert, wohingegen die untere Begrenzung durch die vollständige Verdampfung des Staubes definiert wurde. Bei Modellen mit $T_{\rm eff} = 1600$ K, $\log g = 5.0$ und [Fe/H]$= 0$ erstreckt sich die Wolke über zwei Größenordnungen des Druckes, was einer Dicke von 24 km entspricht.
Spektrale Merkmale zeigen sich nur in den Farbindizes $J - K$. Optisch dicke Staubwolken unterdrücken den austretenden Fluss in den Bändern J ($1.25\,\mu$m), H ($1.65\,\mu$m), and K ($2.16\,\mu$m) des nahen Infrarots. Die Farbindizes $J - K$ in den Modellen mit $\log g = 5.0$ and [Fe/H]$= 0.0$ liegen bei 0.8 ($T_{\rm eff} \gtrsim 2000$ K) und steigen auf bis zu 2.3 ($T_{\rm eff} = 1500$ K), was noch mit Werten von beobachteten Objekten übereinstimmt.
Ein direkter Vergleich mit einem beobachteten Spektrum von DENIS J0205-1159 legt nahe, daß in den vorliegenden Modellen etwas zuviel Staub produziert wird. Zukünftige Verbessungen in der Behandlung der konvektiven Mischung könnten das verhindern, da die Staubbildung stark davon abhängig ist: Änderungen des "Overshoot"-Parameters $\beta = 2.2$ (Woitke & Helling, 2004) um ca. $\pm 10\%$ führen zu einer Änderung der Staubteilchendichte um ca. $\mp 50\%$ ($T_{\rm eff} = 2300$ K). Aktuelle Ergebnisse tendieren zu $\beta = 2.4$ (Ludwig et al., 2006), was mit der notwendigen Verringerung der Staubmenge in künftigen Modellen gut in Übereinstimmung steht.

Abstract

Currently available dust models often assume phase–equilibrium for dust formation to deliver the depletion of gas phase elements which form condensed matter. These models have successfully been used to provide opacities in radiative transfer codes (e.g. Allard et al. (2001); Burrows et al. (2002); Marley et al. (2002); Tsuji (2002)).
A more detailed, self–consistent modeling of the quasi–static dust problem using a kinetic approach, assumes equilibrium chemistry and considers the nucleation of TiO_2 seed particles, a dirty growth, and gravitational drift of the particles (Woitke & Helling, 2003, 2004).
Until now, the feedback on atmospheric structures has not yet been taken into account. The problem of coupling the dust formation and its impact on the radiation field and the energy balance is iteratively being solved using the stellar atmosphere code PHOENIX (Hauschildt & Baron, 1999) by solving the frequency dependent radiative transfer and the structure of the atmosphere in hydrostatic equilibrium. The self–consistent dust model by Woitke & Helling (2003, 2004) and Helling & Woitke (2006) for oxygen–rich dwarfs builds upon an atmospheric structure and provides properties of the dust clouds, which, in turn, allows calculating dust opacities as input for the radiative transfer problem. Atmosphere models with dust consisting of solid TiO_2, Mg_2SiO_4, SiO_2, Fe, Al_2O_3, MgO, and $MgSiO_3$ for effective temperatures of $1500 \ldots 3000$ K (corresponding to late–type objects of spectral type M and L) are presented here.
The resulting dust properties are completely defined by the nucleation rate, the growth reaction speed, the drift velocity, and the convective mixing. Below $T_{\rm eff} = 2800$ K, dust clouds form and become optically thick at $T_{\rm eff} \lesssim 2000$ K. Dust number densities reach maxima of up to 200 grains per $\rm cm^3$ and maximum grain radii reach $1.0 \pm 0.5\,\mu$m. In contrast, previous models without radiative feedback found maximum grain radii of up to $90\,\mu$m (Woitke & Helling, 2004). The cloud deck is characterized by the outer maximum of the nucleation rate and the cloud base is characterized by the complete evaporation of dust grains. For $T_{\rm eff} = 1600$ K, $\log g = 5.0$, and [Fe/H]$= 0$, the cloud encompasses two orders of magnitude in pressure, which corresponds to a distance of 24 km.
Spectral features are only seen in terms of $J - K$ colour indices. The optically thick dust clouds clearly suppress emergent flux in the near infrared bands J ($1.25\,\mu$m), H ($1.65\,\mu$m), and K ($2.16\,\mu$m). Colour indices $J - K$ of models with $\log g = 5.0$ and [Fe/H]$= 0.0$ are approximately 0.8 ($T_{\rm eff} \gtrsim 2000$ K) and increase up to 2.3 ($T_{\rm eff} = 1500$ K), which still is in the range of observations.
Nevertheless, a direct comparison with an observed spectrum of DENIS J0205-1159 suggests, that present models produce slightly too much dust. This might be improved by a more detailed treatment of the convective mixing, because dust formation is very sensitive to the mixing time scale: Varying the overshoot parameter $\beta = 2.2$ (Woitke & Helling, 2004) by about $\pm 10\%$ results in different dust number densities by $\mp 50\%$ (for $T_{\rm eff} = 2300$ K). Recent results in Ludwig et al. (2006) also tend to a higher β of 2.4, which corresponds with the need of less dust formation in future models.

Contents

Chapter 1

Introduction

In the last decade, stellar astrophysics made enormous progress. Since the commissioning of the popular Hubble Space Telescope in 1990 and the Very Large Telescope in Chile in 1998, new discoveries have been made such as deep field exposures or very precise distance measurements to other galaxies, which creates a new view of the structure of our cosmos. Driven by the quest for extraterrestrial life, imaging of exosolar, jovian planets was attempted. Not only as side effect on the quest for exoplanets, but also in trying to determine the composition of galaxies, astronomers also discovered cooler and cooler stellar objects, beyond the spectral type M on the main sequence: These L and T-dwarfs which are apparently a link from cool stars to giant planets are called "brown dwarfs" (Tarter, 1976). They have been predicted by Kumar (1963) and Hayashi & Nakano (1963).
If initial masses of protostars not large enough ($\lesssim 0.1\ M_{\rm sun}$, Chabrier & Baraffe (2000)), stable hydrogen burning will not initiate. Nevertheless, while still collapsing over large timescales, gravitational energy is transported by radiation. Due to the lack of persistent nuclear energy sources and the ongoing gravitational collapse, these objects cool over large timescales (several Gyrs) transiting through several spectral types, from late-M to T.
In this thesis, an important property of the brown dwarfs is examined, which causes significant changes in their spectra: Matter condenses out of the gas phase into the solid phase due to decreasing temperature and forms dust particles. Its feedback on the atmospheric structure due to its opacity and the resulting backwarming effect is a major topic of this work.
In the remaining part of this chapter, the main characteristics of brown dwarfs, L, and T-dwarfs will be reviewed, followed by a summary of recent work concerning dust formation in these objects. In chapter 2.1, a method to model dust formation in brown dwarfs will be described, which was first presented by Woitke & Helling (2003, 2004). The dust model predicts properties, such as dust number densities and mean grain radii, which are used to calculate opacities for application in a stellar radiative transport code. How to compute the opacities is described in chapter 2.2 and the basics of radiative transfer are outlined in chapter 2.4. How results of dust model calculations are applied to the stellar model atmosphere code PHOENIX (Hauschildt & Baron, 1999) is given in chapter 3. Detailed results will be presented in chapter 4 and this work closes with an outlook given in chapter 5.

1.1 Brown dwarfs — the red end of the spectral sequence

It took over 30 years from the prediction to the first observed brown dwarf, which is Gliese 229B. The first image was taken by the Hubble Space Telescope based on a systematic survey (Nakajima et al., 1995). The first spectrum was taken by Oppenheimer et al. (1995) and analyses on the basis of model atmospheres have been performed by e.g. Allard et al. (1996) and Tsuji et al. (1996b). According to these publications, Gliese 229B has an effective temperature of $900 - 1000$ K, and a mass of $0.04 - 0.05\ M_{\rm sun}$. Evolutionary calculations estimate its age as approximately 5 Gyr (Allard et al., 1996). Nearly at the same time, infrared technology matured and provided a basis for several surveys. For example, the "Two Micrometer All Sky Survey" (2MASS, Skrutskie et al. (2006)) and the "Deep Near Infrared Survey of the Southern Sky" (DENIS, Epchtein et al. (1997)) provided the stellar community with infrared data of more than 400 and 300 million point sources respectively as well as with photometry data in the infrared, covering the entire sky (2MASS) or large parts of it (DENIS). The 2MASS collected photometric data in the J ($1.25\,\mu$m), H ($1.65\,\mu$m), and K ($2.16\,\mu$m) bands, whereas DENIS provides I ($0.8\,\mu$m), J, and K band data. Several of these sources were been selected for follow-up spectroscopy and were been identified as L and T dwarfs. Infrared colours are useful to decide very quickly if an object is an L or T-type dwarf. Colour indices $J - K > 1$ with $M_J < 16$ indicate L-dwarfs, where $J - K \approx 0$ and $M_J > 14$ indicate the cooler T-dwarfs (Kirkpatrick et al., 1999; Kirkpatrick, 2005). Thus, model calculations should also reproduce these criteria.

Stars and brown dwarfs have interesting spectral properties, as they both are found on the main sequence in a Hertzsprung-Russell Diagram. As seen in Figure 1.1, the spectral type sequence is an effective–temperature–sequence. The different spectral types (L8 - T3) at the same effective temperature (≈ 1500 K) are hints on dust features, which is discussed below. The characteristics of a temperature sequence can be explained in terms of atomic and molecular physics. At higher effective temperatures, ions dominate the spectrum. With decreasing effective temperature, atoms go into the neutral state, form molecules, and finally condense into liquid or solid phases. Cool stars with spectral type M show dominant features of TiO, VO, CO, FeH and H_2O in the near infrared regime ($\lambda = 1 \ldots 3\,\mu$m). Additionally, atomic lines of Al, Na, Fe, K, and Ca remain visible.

With lower effective temperatures, we enter the regime of L-type stars or L-type substellar objects. The absorption of H_2O becomes more dominant and features of molecular TiO and VO disappear. In the assumption of phase equilibrium, titanium and also a fraction of the oxygen are supposed to be bound in solid phases, for example in rutile (TiO_2[s]) or other complex compounds ($CaTiO_3$, $Ca_4Ti_3O_{10}$, $Ca_3Ti_2O_7$, Ti_2O_3, Ti_3O_5, Ti_4O_7). Vanadium oxide may also condense to VO_2 or other condensates. In addition also Al and Ca are bound into solid phase condensates (e.g. Al_2O_3, $CaAl_{12}O_{19}$, $CaAl_4O_7$, $Ca_2Al_2SiO_7$) and, therefore, above mentioned atomic and molecular features vanish or are weakened at least. (Burrows & Sharp, 1999; Lodders, 1999, 2002; Cooper et al., 2003; Kirkpatrick, 2005)

Objects with spectral type T form CH_4 at the expense of CO. Water vapour features become stronger and also NH_3 features are detectable at late types. Also, at later types

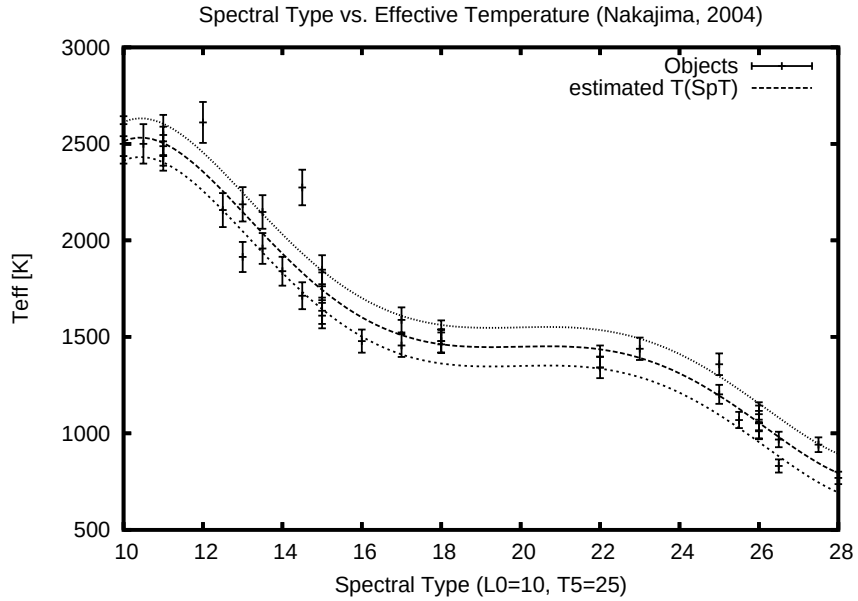

Figure 1.1: Spectral type versus effective temperature by Nakajima et al. (2004). The middle lines is based on a polynomial fit, where the upper and lower line indicate an estimated error of ±100 K. Similar plots are also found in Golimowski et al. (2004) and Kirkpatrick (2005).

(T8), collision-induced absorption (CIA) of H_2 suppresses flux at about 2 μm (K-band) which is sensitive in terms of changes in surface gravitation. (Burgasser et al., 2002)
The spectral energy distribution is represented by photometric colour indices. The J-K index increases from hotter M-type objects and then decreases in the regime of T-dwarfs, which is expected, as the maximum of the spectral energy distribution is approximately in the J band ($1 - 1.5$ μm). But, as seen in Figure 1.2, J-K shows a significant scattering for sectral types L3 to T0. This is expected to different behaviour of dust clouds caused by differences in age, metallicity, and rotation period of the objects (Leggett et al., 2002; Stephens & Leggett, 2004).

1.2 Works on models of dust in brown dwarf atmospheres

It will become clear in this chapter, that current models are based on the same assumptions which differ from the dust model described in chapter 2.1.
Laboratory experiments of dust formation or direct measurements of dust particles in the interplanetary space provide hints about the properties of dust. For example, the investigation of micro impacts on lunar rocks gave an idea of the particle size distribution of the interstellar dust (Le Sergeant D'Hendecourt & Lamy, 1980). From this measurements and fits based on these results, the interstellar grain size distribution is often given by the power law $n(a) \propto a^{-3.5}$ (Witteborn et al., 1982). A general and thorough review of interstellar dust physics is given in Draine (2003).
Conditions in space can be simulated in the laboratory only in a restricted way only.

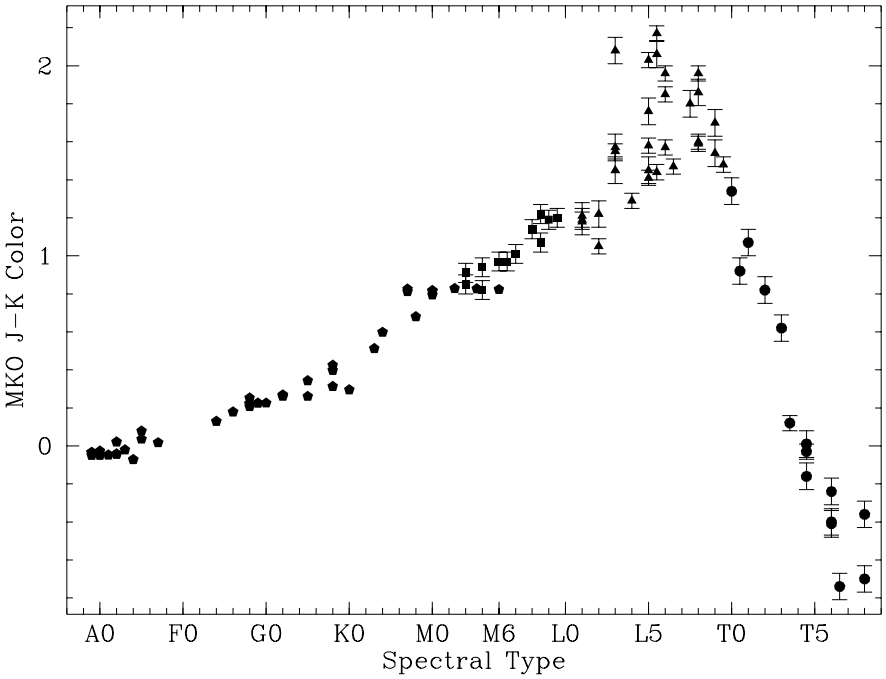

Figure 1.2: J-K colour indices in MKO filter set of different spectral types from A0 to T9. See the scattering of the indices at spectral type L3-T0. Figure from Stephens & Leggett (2004)

This is consequently also true for cool stellar atmospheres. Therefore, physical conditions of these atmospheres and the treatment of their dust have to be done via simulations. Thermodynamic calculations as basis of dust formation are used in current models (Sharp & Huebner, 1990; Lodders, 2003). These calculations treat the possibility of dust formation in phase-equilibrium assumption as equilibrium chemistry by given temperature and pressure and yield condensation curves. These temperature-pressure profiles show at which physical conditions distinct solid species remain stable. In recent years, theoretical considerations of dust formation have been applied to low mass stars and brown dwarfs:

Work by Tsuji et al.:
In the model assumptions of Tsuji an co-workers, dust may form at supersaturated ratios ($S > 1$). The saturation ratio is defined as $S = n_{\mathrm{gas}} kT / P_{\mathrm{vap}}$, where P_{vap} is the vapour pressure of the gas component. States with $S > 1$ are supersaturated states. Small dust grains survive in atmosphere layers where $T_{\mathrm{crit}} \leq T \leq T_{\mathrm{cond}}$. Here, T_{crit} denotes a "critical" temperature, where dust grains are about to grow so much that they settle down into optical thick parts of the atmosphere and do not contribute to the opacity in the photosphere. Only small grain particles remain in the photosphere and therefore its opacity is approximately independent of the size distribution. Thus, a grain radius of $0.01\,\mu$m is assumed. This critical temperature is a free parameter, which is often set to $1600 \ldots 2000$ K, from fits to observed spectra.
(Tsuji et al., 1996a,b; Jones & Tsuji, 1997; Tsuji, 2002, 2005)

Work by Allard et al.:
In these models, a check of the saturation ratio is performed. If the gas phase is supersaturated ($S > 1$), condensates are considered to be present. Simultaneously, the gas phase of the affected elements or molecules are depleted until the saturation ratio equals unity. The grains are assumed to be homogeneous and spherical, and its size distribution is prescribed by different distribution laws, where the distribution of the interstellar medium ($n(a) \propto a^{-3.5}$) is used by default. There are two limiting cases that are considered.
One is the `COND` model, where dust forms, but all dust is assumed to settle down into the deeper (and optically thick) parts of the atmosphere. Technically, the gas depletion takes place, but the dust opacity is set to zero.
The other one is the `DUSTY` model, where dust forms and remains at the place in the atmosphere where it formed. The opacity is fully considered and the gas phase depleted. In more recent work, the fact that dust is settling partially in the atmosphere had been taken into account by time scale arguments according to Rossow (1978) (`SETTLING` models).
(Allard et al., 1997, 2001, 2003)
Work by Ackerman & Marley:
In this model, gas parcels are supposed to be driven upwards, where dust condenses at higher layers if the saturation ratio exceeds unity.Their main equation expresses a balance of raising gas and dust moving downwards. There is a free parameter $f_{\rm sed}$ describing the efficiency of the gravitational settling of the grains. The particle size is given by a log-normal size distributions, where its parameters are partially free adjustable. Mean particle sizes in L and T dwarfs reach up to 75 μm.
(Marley et al., 1999; Ackerman & Marley, 2001; Marley et al., 2002)
Work by Burrows et al.:
In the previous models, condensation occurs if the saturation ratio is larger than unity. In the Burrows model, the condition is $S > 1 + x$, where x is a free parameter for each dust species, e.g. 0.01 for iron and 1.0 for forsterite. The amount of dust is arbitrarily scaled by free parameters. These characterize a constant part in the middle of a cloud and a decline at the cloud deck and cloud base. The grain particle size distribution is a delta function and set to a mean particle size which is also a free parameter. Mean sizes between 10 to 100 μm are found to reproduce observed spectra best, as they do not smear out features of K I in the J-bands and features of CO in K-bands.
(Burrows et al., 2001, 2006)
Work by Cooper et al.:
Condensates in the model of Cooper et al. (2003) are supposed to be present at supersaturation $S > 1 + x$, again with x being a free parameter. The mean size of grains a_0 is determined by local time scale arguments based on work of Rossow (1978) and reaches values of $2 \ldots 300$ μm, depending on dust species, surface gravity, and effective temperature. The particle size distribution is given by $f(a) \propto (a/a_0)^6 \exp(-6a/a_0)$ (Sudarsky et al., 2000).
(Cooper et al., 2003)

These dust models have some features in common: Supersaturation $(S-1)$ in the order of $0.01 \ldots 2$ defines the amount of existing dust grains. The physical forming processes

of the grains are *not* taken into account. Settling of grains by gravitational drift is ignored in older models or described by free parameters. The grain size distribution is often set arbitrary on base of best fit results where mean grain sizes differ by four orders of magnitude in several models (0.01 μm in models of Tsuji et al. and 100 μm in models of Burrows et al.). However, if grain sizes are derived by time scale arguments by Rossow (1978), mean grain sizes vary from 10 to 300 μm (Allard et al., 2003; Cooper et al., 2003).

Chapter 2

Basic equations

2.1 Microphysical model of dust formation

Dust grains consist of stable monomers in the solid phase. Monomers are the basic units of a grain. The available molecules for grain formation depend strongly on the carbon to oxygen ratio. Due to CO-blocking either carbon-bearing molecules such as TiC, SiC, C_2, C_3, C_2H_2 or oxygen-bearing molecules such as SiO, TiO_2, MgO, CaO, VO are stable.
The exact shapes of dust grains in brown dwarfs are unknown. Shapes are only known from of grains collected from interplanetary space or meteorites. Assumptions of the grains shape are based on considerations made from observations of interstellar dust. Thus, shapes may vary from simple spheres (Clayton et al., 1971) or oblate ellipsoids (Sengupta & Krishan, 2001) to more complex shaped grains (Wright, 1989; Fabian et al., 2000; Iatì et al., 2001; Min et al., 2006). Compositions may be completely heterogeneous ("dirty") or coated by shells of other material, as e.g. proposed by Brown et al. (1989) for interstellar grains or Preibisch et al. (1993) for protostars.
The dust formation theory used here for oxygen rich brown dwarfs was developed by Woitke & Helling (2003, 2004) and Helling & Woitke (2006) and follows the approach of Gail et al. (1984) and Gail & Sedlmayr (1988). In high atmospheric layers, where saturation ratios are very high, nucleation takes place which forms microscopic condensation seeds. By surface reactions with distinct gas molecules ("gas-grain reactions"), the seed particles are growing to macroscopic dust grains. Due to the consumption of gas molecules, initial gas phase elemental abundances become depleted. Theoretically, coagulation ("grain-grain reactions") is also a possible mechanism. Time scale considerations showed that coagulation reactions are too slow compared to other mechanisms and, therefore, play no role (Cooper et al., 2003).
In contrast to red giant stars, the growing dust particles drift *down* into deeper and hotter parts of the atmosphere, since gravitation is more dominant than radiative pressure in brown dwarfs. Conditions in the deep parts of the atmosphere normally do not allow the formation of new dust grains. But due to gravitational drift, the dust grains move into these atmosphere layers. The growth of the grains which formed in higher parts can still take place until a distinct depth is reached. There, dust grains evaporate into their molecules and/or atoms.

The formation and growth of dust grains "consumes" elements which leads to a depletion of the corresponding atmosphere layers. The grains evaporate in deep layers, but there are no elements left which produces new grains. Thus, a quasi-static atmosphere would be completely dust free. As brown dwarfs are fully convective, the overshooting mechanism (Ludwig et al., 2002) transports "fresh" elements into high atmosphere layers and replenish the consumed elements again. This leads to a circulation of dust, which is sketched in Figure 2.1.

The underlying physical processes of the dust circulation and the solution method of

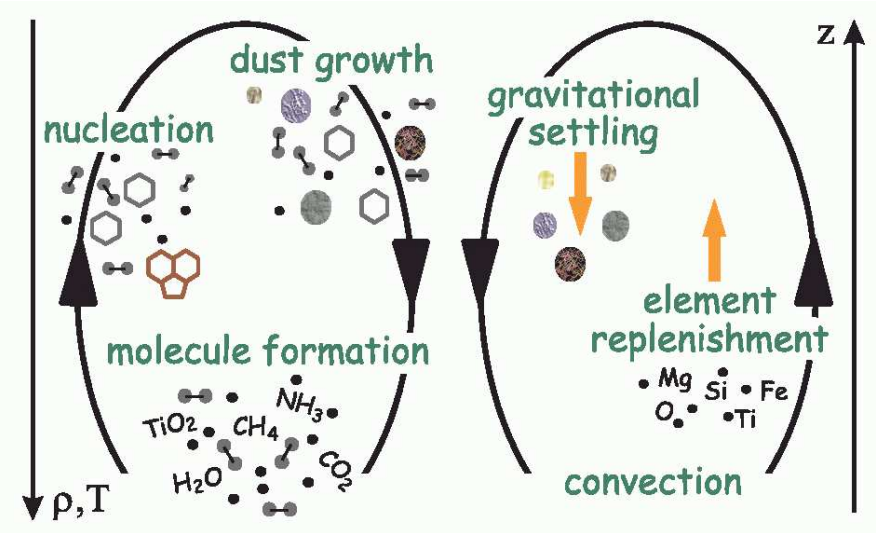

Figure 2.1: Sketch of circulation of dust in brown dwarfs. (Helling et al. 2001)

the general dust treatment are briefly reviewed in the subsequent paragraphs. Afterwards, some aspects which are needed for the coupling to the radiation transfer are outlined.

2.1.1 Nucleation

In this approach, condensation only occurs if $S \gg 1$ which is in contrast to all the considerations discussed in 1.2: Usually small impurities (e.g. aerosols in atmospheres) lead to a condensation of the gas onto their surfaces. This occurs already at quite low supersaturation ratios. However, in brown dwarfs atmospheres, we cannot assume a priori that seed particles like aerosols exist. So, if there are no impurities it may be possible that the gas is highly saturated. Thus, spontaneous nucleation has to be modelled which had been treated several decades before in several ways. Classical representatives of work on nucleation theories are Becker & Döring (1935) and Draine & Salpeter (1977). In this chapter, the results of Gail et al. (1984); Gail & Sedlmayr (1988); Helling et al. (2001); Woitke & Helling (2003, 2004) are used.

Nucleation can be considered on a net of n-mere reactions (n-mere = n monomers) as shown in Figure 2.2. There, one energetically favoured distinct reaction path exists,

$$A_1 \rightleftharpoons A_2 \rightleftharpoons \ldots \rightleftharpoons A_{N_*} \rightleftharpoons \ldots \rightleftharpoons A_N, \tag{2.1.1}$$

where A_N represents the nucleation seed with N monomers. Every reaction $A_i \rightleftharpoons$

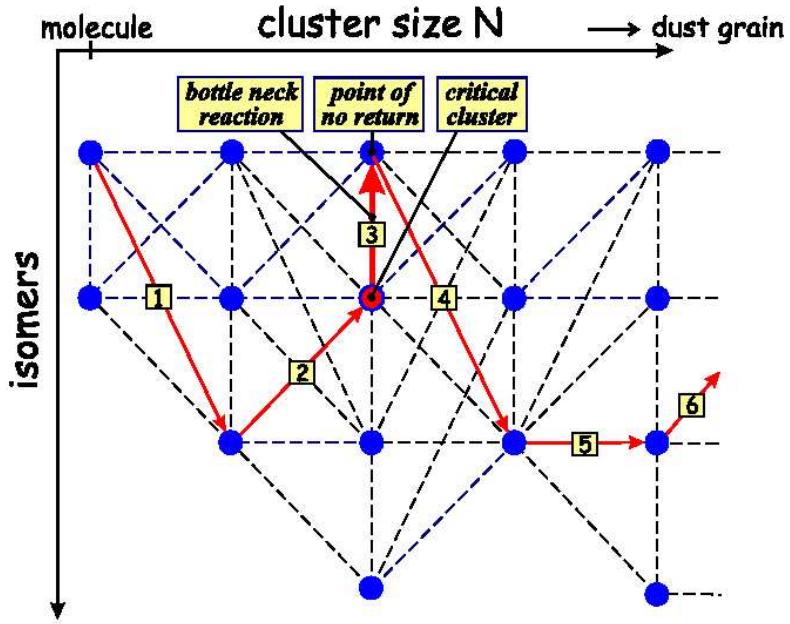

Figure 2.2: Net of n-mere reactions. One reaction path is favoured (red arrows). After a critical cluster has formed, the reaction path balances toward the dust grain. The numbers denote reaction numbers. (By courtesy of Peter Woitke)

A_j, $i < j$ is a reaction which can occur in both directions at different timescales: Timescales of growth reactions are denoted with $\tau_j^{\rm growth}$ $(A_i \rightharpoonup A_j)$ and evaporation timescales are denoted with $\tau_i^{\rm evap}$ $(A_i \rightharpoonup A_j)$. The distribution of clusters of size i in quasi stationary equilibrium is denoted with $\dot{f}(i)$. At sufficiently low temperatures, reaction rates in both direction become about the same ($\dot{f}(i)/\tau^{\rm growth} \approx \dot{f}(i)/\tau^{\rm evap}$), except for the formation of the critical cluster of size $N_* < N$. Its evaporation rate $\dot{f}(N_*)/\tau^{\rm evap}$ is small compared to its corresponding growth reaction rate $\dot{f}(N_*)/\tau^{\rm growth}$. The reaction which forms the critical cluster is also called a "bottleneck reaction", because its rate determines the rate of subsequent reactions of larger clusters. Consequently, the formation of the critical cluster leads to the formation of the seed particle of size N, if the flux through the cluster space towards larger N can be considered stationary. Thus, the total nucleation rate of seed particles can be determined by the nucleation rate of the critical cluster:

$$J^* \approx \frac{\dot{f}(N_*)}{\tau_{N_*}^{\rm growth}} \qquad [{\rm cm}^{-3}\ {\rm s}^{-1}] \tag{2.1.2}$$

According to the dust model of Woitke & Helling (2003, 2004), TiO_2 was chosen as seed particle, because in contrast to the thermodynamically more stable Al_2O_3, TiO_2 has stable monomers in the gas phase and additionally can form seeds by the primary reaction $TiO_2 + (TiO_2[s])_N \rightleftharpoons (TiO_2[s])_{N+1}$.[1] $Al_2O_3[s]$ on the other hand, requires a catalyst

[1] Solid phases are denoted with "[s]"

surface for condensation (Patzer et al., 1999). For TiO_2, the extended classical nucleation theory (Gail et al., 1984) can be used, with surface tension $\sigma_{TiO_2} = 620$ erg/cm^2 (Jeong, 2000):

$$J^* = \frac{n_{TiO_2}}{\tau} Z \exp\left[(N_* - 1)\ln S - \left(\frac{T_\Theta}{T}\right)(N_* - 1)^{2/3}\right] \tag{2.1.3}$$

With $T_\Theta = 4\pi a_0^2 \sigma / k$ with surface tension σ and a_0 hypothetical monomer radius, $N_* = (\frac{2}{3}\frac{T_\Theta}{T}\frac{1}{\ln S})^3$ the critical cluster size, Z the Zeldovich factor (Gail et al., 1984, Eq. 2.18), and $\tau^{-1} = n_{TiO_2} v_{rel} N_*^{2/3} A_0$ the reaction time. The characteristics of J^* at different temperatures and number densities of gaseous TiO_2 are shown in the appendix on page 75.

2.1.2 Growth and evaporation

Another main physical mechanism is the growth of a grain, which describes the condensation of dust material in the gas phase directly onto the surface of an already existing grain. The growth of a dust grain depends on its effective surface area and the supersaturation ratio of the surrounding gas material. The considered case of subsonic free molecular flow had been discussed in detail by Gail & Sedlmayr (1988); Gauger et al. (1990); Dominik et al. (1993). According to Woitke & Helling (2003), the volume of a grain changes with

$$\frac{dV}{dt} = 4\pi a^2 \sum_r \Delta V_r n_r v_r^{\mathrm{rel}} \alpha_r \left(1 - \frac{1}{S_r}\right). \tag{2.1.4}$$

Here, r denotes a single reaction of a gas molecule with the grain. If a reaction occurs, ΔV_r is the increase of the grain volume after the reaction. The number density of a gas species is denoted with n_r and v_r^{rel} is its relative speed to the grain, given by the Maxwell-distribution. The "sticking coefficient" α_r is a generalised coefficient of the sticking probability of the gas molecule to the grain. Finally, S_r denotes the supersaturation ratio of the gas molecules in the surrounding medium for the reaction r. The supersaturation ratio determines the sign of dV/dT, which describes the effective growth of a dust grain.
Each reaction heats resp. cools the dust grain. This effect is very small in typical brown dwarf atmospheres. For typical pressure and temperature ranges, the difference of heated/cooled dust is $\Delta T \approx 3.5$ K as an upper limit (Woitke & Helling, 2003). Thus, this effect will be neglected and the equality of grain and gas temperature is assumed.

2.1.3 Gravitational settling

The movement of a dust grain in a gravitational field is called gravitational settling. The velocity of the grain can be derived by an equation of motion:

$$m\dot{v}_{\mathrm{drift}} = -gm + F_{\mathrm{fric}}(a, \rho, T, v_{\mathrm{drift}}) \tag{2.1.5}$$

Here, a is the radius of the dust grain, $m = 4\pi/3 a^3 \rho_d$ its mass and density ρ_d, v_{drift} its velocity relative to the surrounding gas (drift velocity), g the gravitational acceleration, and F_{fric} the force of friction. Compared to the gravitational force, the force of

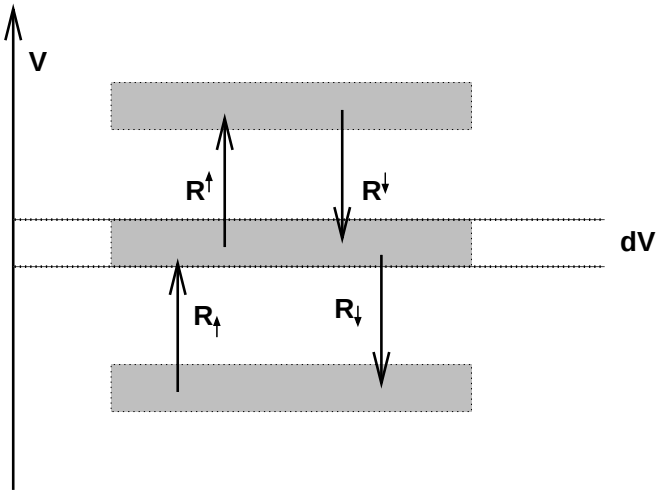

Figure 2.3: Scheme of one type of growth and evaporation reactions r at given volume. The population rate $R^{\uparrow}$ decreases the population of grains in the current volume interval dV and increases the population with higher volumes. The mechanisms for $R_{\uparrow}$, $R^{\downarrow}$, and $R_{\downarrow}$ are analogue.

radiation may be neglected in brown dwarfs (which is *not* the case for giant stars, as shown e.g. in Woitke & Helling (2003)).
The treatment of friction depends on the surrounding medium and the drift velocity. The ratio of the mean free path of a grain compared to its radius is called Knudsen number Kn. Additionally, the Reynolds number Re is a measure of the transition from a laminar to a turbulent flow. Depending on $v_{\rm drift}$, Kn, and Re, different treatments of the friction force are needed. In Woitke & Helling (2003), very detailed numerical tests have been presented. These show that the subsonic free molecular flow ($Kn \gg 1$, $v_{\rm drift} \ll v_s$, v_s : sonic speed) is appropriate for small grain sizes and low gas densities ($a \lesssim 100$ μm and $\rho \lesssim 10^{-7}$ g cm^{-3}). In this case, the friction force is $F_{\rm fric}(a,\rho,T,v_{\rm drift}) = \frac{8\sqrt{\pi}}{3} a^2 \rho v_s v_{\rm drift}$. There may be some atmospheric regions for which this case is not applicable. Finally, an equilibrium drift velocity can be considered, which is given by

$$v_{\rm drift} = \frac{\sqrt{\pi}}{2} \frac{\rho_d g}{\rho v_s} a. \tag{2.1.6}$$

2.1.4 Solution method

The mechanism of growth and evaporation surface reactions r of a dust grain is illustrated in Figure 2.3. A dust grain in the volume interval dV grows or evaporates by surface reactions. This time dependent mechanism can be expressed formally (Gail & Sedlmayr, 1988; Dominik et al., 1993; Woitke & Helling, 2003) via

$$\frac{\partial}{\partial t}\left(f(V)dV\right) + \nabla\left(\left[v_{\rm gas} + v_{\rm drift}(V)\right] f(V)dV\right) = \left(R_{\uparrow} + R^{\downarrow} - R^{\uparrow} - R_{\downarrow}\right) dV. \tag{2.1.7}$$

The population and depopulation of the volume V by growth or evaporation reactions r are denoted with $R_{\uparrow}$, $R^{\downarrow}$, $R^{\uparrow}$, and $R_{\downarrow}$, generally expressed by $\sum R_k$. In the case of subsonic free molecular flow ($Kn \gg 1,\ v_{\mathrm{drift}} \ll v_s$) it can be written as following (Woitke & Helling, 2003):

$$R^{\uparrow} dV = \sum_r f(V) dV 4\pi \left[a(V)\right]^2 n_r v_r^{\mathrm{rel}} \alpha_r \tag{2.1.8}$$

$$R_{\uparrow} dV = \sum_r f(V - \Delta V_r) dV 4\pi \left[a(V - \Delta V_r)\right]^2 n_r v_r^{\mathrm{rel}} \alpha_r \tag{2.1.9}$$

$$R^{\downarrow} dV = \sum_r f(V + \Delta V_r) dV 4\pi \left[a(V)\right]^2 n_r v_r^{\mathrm{rel}} \alpha_r \frac{1}{S_r} \tag{2.1.10}$$

$$R_{\downarrow} dV = \sum_r f(V) dV 4\pi \left[a(V - \Delta V_r)\right]^2 n_r v_r^{\mathrm{rel}} \alpha_r \frac{1}{S_r} \tag{2.1.11}$$

If the master equation 2.1.7 is multiplied with $V^{j/3}$ and integrated from V_l to ∞, we obtain the dust moments equation:

$$\begin{aligned} \frac{\partial}{\partial t}(\rho L_j) + \nabla\left(\mathbf{v}_{\mathrm{gas}}\ \rho L_j\right) = & \int_{V_l}^{\infty} \left(R_{\uparrow} + R^{\downarrow} - R^{\uparrow} - R_{\downarrow}\right) V^{j/3} dV \\ & -\nabla \int_{V_l}^{\infty} f(V) V^{j/3} v_{\mathrm{drift}}(V) dV \\ = & \quad V_l^{j/3}\ J^* + \frac{j}{3}\ \chi_{\mathrm{lKn}}^{\mathrm{net}}\ \rho L_{j-1} \\ & + \xi_{\mathrm{lKn}}\ \nabla\left(\frac{L_{j+1}}{c_{\mathrm{T}}} \mathbf{e}_r\right) \end{aligned} \tag{2.1.12}$$

with

$$\rho L_j = \int_{V_l}^{\infty} f(V) V^{j/3} dV \tag{2.1.13}$$

$$\chi_{\mathrm{lKn}}^{\mathrm{net}} = \sqrt[3]{36\pi} \sum_{r=1}^{R} \Delta V_r n_r v_r^{\mathrm{rel}} \alpha_r \left(1 - \frac{1}{b_{\mathrm{mix}}^d S_r}\right) \tag{2.1.14}$$

$$\xi_{\mathrm{lKn}} = \frac{\sqrt{\pi}}{2} \left(\frac{3}{4\pi}\right)^{1/3} g \rho_d \tag{2.1.15}$$

The expression ρL_j ($[\mathrm{cm}^{j-3}]$) with $j = 0, 1, 2, ...$ are the j'th moments of the dust size distribution function $f(V)$ in volume space. The minimum volume of a grain is denoted by V_l and assumed to be 1000 times the volume of a TiO_2 monomer (Woitke & Helling, 2004). The growth speed is denoted with $\chi_{\mathrm{lKn}}^{\mathrm{net}}$ or χ_{net} and b_{mix}^d is the volume fraction of a dust species (Helling & Woitke, 2006). ξ_{lKn} is the drag force density. χ_{net} is called a net growth/evaporation rate also, as all dust reactions which can occur are summarised and expressed in this value.

According to Gail et al. (1984) and Woitke & Helling (2003), the dust moments correspond directly with physical mean properties of the grains (Dominik et al., 1993; Helling et al., 2001). The number density of dust grains is given by

$$n_d = \rho L_0, \tag{2.1.16}$$

the mean grain radius by

$$<a>= \sqrt[3]{\frac{3}{4\pi}}\frac{L_1}{L_0}, \tag{2.1.17}$$

the average dust surface by

$$<A>= \sqrt[3]{36\pi}\frac{L_2}{L_0}, \tag{2.1.18}$$

and the mean dust volume by

$$<V>= \frac{L_3}{L_0}. \tag{2.1.19}$$

In the case of stationary (time independent) dust components ($\frac{\partial L_j}{\partial t} = 0$), under the assumption of a plane parallel atmosphere ($\mathbf{e}_r = \mathbf{e}_z$) without movement of the gas ($\mathbf{v}_{\rm gas} = 0$), and a constant gravitation ($g = \text{const}$), the left side of the dust moments equation 2.1.12 becomes zero and the right hand side simplifies to a derivative in one dimension. The equations become a system of j differential equations:

$$-\frac{d}{dz}\left(\frac{L_{j+1}}{c_{\rm T}}\right) = \frac{1}{\xi_{\rm lKn}}\left(V_l^{j/3}\ J^* + \frac{j}{3}\ \chi_{\rm lKn}^{\rm net}\rho L_{j-1}\right) \tag{2.1.20}$$

It has been shown by Woitke & Helling (2004) that the coupled system in this static case has only a trivial solution, which means the atmosphere is totally dust free, because the dust grains sink down in deeper atmospheric layers. New dust grains cannot form because the gas is too much depleted of dust forming elements.
Dust forming molecules may be replaced due to convective mixing: Matter from deeper atmospheric layers flows up to higher zones and enriches the gas with fresh material making dust formation possible again. The mixing is added to Eq. 2.1.20 as a term $\frac{\rho L_j}{\tau_{\rm mix}}$, where $\tau_{\rm mix}$ is a depth dependent mixing time scale (Woitke & Helling, 2004):

$$\log\tau_{\rm mix} = \tau_{\rm mix}^{\rm min} + \beta\cdot\max\left\{0, \log p_0 - \log p(z)\right\} \tag{2.1.21}$$

Here, $\beta = \frac{\Delta\log f_{exchg}}{\Delta\log p} \approx 2.2$ is given by the measurement of the steepness of the graph (Ludwig et al., 2002, fig. 16) and $f_{\rm exchg}$ is the mass exchange frequency.
The stationary equation, including the mixing, is then

$$-\frac{d}{dz}\left(\frac{L_{j+1}}{c_{\rm T}}\right) = \frac{1}{\xi_{\rm lKn}}\left(-\frac{\rho L_j}{\tau_{\rm mix}} + V_l^{j/3}\ J^* + \frac{j}{3}\ \chi_{\rm lKn}^{\rm net}\rho L_{j-1}\right). \tag{2.1.22}$$

As this is not a closed differential equation, closing conditions have to be found, which is discussed in detail in Woitke & Helling (2003). An alternative approach will be presented in Helling et al. (2007).

Secondary constrains must be obeyed, namely the conservation of stoichiometric coefficients and mass. This is considered by the algebraic equation

$$\frac{n_{<H>}(\varepsilon_i^0 - \varepsilon_i)}{\tau_{\mathrm{mix}}} = \nu_{i,0} N_l J^* + \sqrt[3]{36\pi}\ \rho L_2 \sum_r \nu_{i,r} n_r, v_r^{\mathrm{rel}} \alpha_r \left(1 - \frac{1}{S_r}\right). \tag{2.1.23}$$

Here, ε denotes the abundance of the involved element i, where ε^0 refers to the solar (or initial) composition. ν_i are the stoichiometric coefficients and n_r the particle densities of the involved species. By solving equation 2.1.22 with the constraints given in equation 2.1.23, the dust moments are derived which provide properties of the dust model with all needed information.

2.1.5 Grain size distribution

As mentioned before, the size distribution of dust grains is not very well understood. Some authors found a power law size distribution $n(a) \propto a^\gamma$ appropriate to the model of the interstellar medium (Le Sergeant D'Hendecourt & Lamy, 1980). The distribution $n(a) \propto a^{-3.5}$ (Witteborn et al., 1982) is widely used and sometimes adapted for brown dwarfs, e.g., by Allard et al. (2001) despite totally different origin of the dust: Interstellar dust is formed in AGB giant stars and blown into interstellar space through radiative forces. Calculations have been made to examine the influence of the gravitational drift velocity on the shape of the grain size distribution curve (Krüger & Sedlmayr, 1997) for carbon-rich AGB stars. They discovered that there are generally less but larger grains if drift is included. Consistent with the results of this paper, observations in laboratory experiments find a logarithmic normal distribution of the dust grains.
The kind of grain size distribution cannot be concluded from dust moments calculations. Thus, a priori assumptions of the distribution have to be made. The most simple assumption is single sized dust:

$$n(a) = n_d\ \delta(a - <a>) \tag{2.1.24}$$

Due to the definition of the dust moments, a given dust size distribution has to fulfill the condition

$$\rho L_j = \int_{V_l}^{\infty} f(V) V^{j/3} dV. \tag{2.1.25}$$

With dust moments K_j and lower integration boundary a_l in radius space it can be written

$$K_j = \int_{a_l}^{\infty} n(a) a^j da. \tag{2.1.26}$$

Generally, every parametrised function $n(a, c_0, c_1, \ldots, c_n)$ can be used for a description of the distribution function if for each $j = 0, \ldots, n$ a K_j exists, for example exponential or log-normal functions. But due to numerical reasons, an analytical integrable function

is preferred. Therefore, another approach, similar to equation 2.1.24, is using multiple discrete grain sizes:

$$n(a) = \sum_{i=1}^{N} N_i \delta(a - a_i) \tag{2.1.27}$$

In this case, a_i and N_i are unknowns which can be determined if $\rho L_j,\ j = 0 \ldots (2 \times N)$ are available dust moments (see equation 2.1.13). Limited to $N = 2$, the difference $|a_1 - a_2|$ is a rough measure of the width of the grain size distribution which is used in the calculations.

2.2 Opacity treatment

If the dust problem itself is solved, it has to be used to compute opacities for the solution of the radiative transfer. The physical structure and shape of real dust grains are not completely known (see chapter 2.1). We assume homogeneous spheres of composite dust material as a first order approach. As seen from results of the dust moment equation (2.1.22), the grain size has the same order as the wavelength of the light, thus the Rayleigh approximation[2] is not appropriate. Instead, the complete application of Mie theory is needed (Mie, 1908; Boren & Huffman, 1983), which is described in 2.2.3. In order to apply Mie theory, the size of the dust grain and its optical properties are needed as input. Optical properties or optical data in this context is the complex refractory index $m = n + ik$, in which at least n is known from classical refractory law. Connected to refractory index is the complex optical permittivity $\varepsilon = (\varepsilon_r + i\varepsilon_i)$, which relates to complex refractive index as

$$\varepsilon_r = n^2 - k^2 \qquad \varepsilon_i = 2nk \tag{2.2.1}$$

or vice versa:

$$n = \sqrt{\frac{1}{2}\left(\varepsilon_r + \sqrt{\varepsilon_r^2 + \varepsilon_i^2} \right)} \tag{2.2.2}$$

$$k = \sqrt{\frac{1}{2}\left(-\varepsilon_r + \sqrt{\varepsilon_r^2 + \varepsilon_i^2} \right)}. \tag{2.2.3}$$

Mie theory yields extinction efficiencies (Q) or optical cross sections (C) and with the gas density the appropriate extinction ($\chi = \kappa + \sigma$). The connection between these properties is given in the subsequent chapters.

2.2.1 Optical data

Optical data are wavelength dependent complex refractive indices $m(\lambda) = n(\lambda) + ik(\lambda)$ and are tabulated in several sources. In this work, the seven dust species Al_2O_3, Fe, MgO, $MgSiO_3$, Mg_2SiO_4, SiO_2, and TiO_2 are used. The source of optical data and their available wavelength range is given in table 2.1. In the last row of table 2.1, "silicate" denotes an composition of silicates, supposed to be present in the interstellar medium. Its optical properties were calculated by Draine (1985). The used optical data are shown in the appendix (pg. 85). The optical data had been re-sampled to an logarithmic spaced wavelength grid of 601 grid points in the range of 0.1 to 100 μm, in order of an uniform treatment of the different data sets. Unavailable points were set to m = 1 (vacuum), although it is appropriate to extrapolate some data points (Mutschke, 2006, priv.comm.).
The composition of a dust grain and also the optical properties of each species are known. In order to gain the optical properties of the compound grain an effective medium theory is needed.

[2]Rayleigh approximation: $\frac{Q_{ext}}{a} = \frac{8\pi}{\lambda} Im\left(\frac{m^2-1}{m^2+2}\right)$, with Q_{ext} extinction efficiency, a grain radius, λ wavelength of light, and m complex refractive index

Solid	$\lambda_{\min}$ [μm]	$\lambda_{\max}$ [μm]	Reference
Al_2O_3	0.1	200.00	Begemann et al. (1997); Palik (1991)
Fe	$1.24 \cdot 10^{-4}$	285.70	Palik (1985, 1991)
MgO	0.0165	626.162	Palik (1985, 1991)
$MgSiO_3$	0.196	9998.0004	Jäger et al. (2003)
Mg_2SiO_4	0.196	948.53	Jäger et al. (2003)
SiO_2	$1.24 \cdot 10^{-4}$	500.00	Palik (1985, 1991)
TiO_2	1.00	48.56	Posch (1999)
"Silicate"	0.05	2000.00	Draine (1985)

Table 2.1: Optical data used in this work. The first column shows the species, second and third column show the available wavelength range, and the last one indicates the reference.

2.2.2 Effective medium theory

In general, the effective medium theory (EMT) is a description of the optical properties of a compound medium, if the properties of each fraction species is known (Makse et al., 1999; Ossenkopf, 1991). Consistent EMTs are based on the assumption of the existence of a host medium, which consists of small inclusions in the small particle limit. Expressed in permittivities, their relation can be written as (Aspnes et al., 1979)

$$\frac{\bar{\varepsilon} - \varepsilon_h}{\bar{\varepsilon} + \gamma\varepsilon_h} = \sum_i f_i \frac{\varepsilon_i - \varepsilon_h}{\varepsilon_i + \gamma\varepsilon_h}, \tag{2.2.4}$$

with the depolarization factor $\gamma = \frac{1}{l} - 1$ (for spheres: $l = 1/3 \rightarrow \gamma = 2$), the volume fractions f_i of each component with $\sum_i f_i = 1$, $\bar{\varepsilon}$ is the wanted effective permeability and ε_h the permeability of the host medium. It is assumed that the inclusions only react with each other by dipole interactions and the inclusions are spherically. There are three common specialisations of EMT:

- Maxwell Garnett (1904) (setting $\varepsilon_h = \varepsilon_1$)
- Lorentz-Lorenz (setting $\varepsilon_h = 1$)
- Bruggeman (1935) (setting $\varepsilon_h = \bar{\varepsilon}$)

Maxwell-Garnett assumes that the host medium is one of the inclusions by itself. In this case, the expression is only valid for a dominant abundance of the distinct inclusion compared to the host medium, which means that the total fraction of inclusions should exceed 90%. This specialisation is not useful for dust grains, as the fractions can change completely at different atmosphere layers. Neither the Lorentz-Lorenz formulation is valid, which assumes the host medium is the vacuum. The theory of Bruggeman (Bruggeman, 1935) assumes the host medium to be the effective medium, which provides self consistency in our case. Thus, setting $\varepsilon_h = \bar{\varepsilon}$ yields

$$\sum_{i=1}^{N} f_i \frac{\varepsilon_i - \bar{\varepsilon}}{\varepsilon_i + \gamma\bar{\varepsilon}} = 0 \tag{2.2.5}$$

Equation 2.2.5 reduces the search of optical properties of the compound grain to a simple root finding problem, which may be solved easily for complex arguments e.g. by Müllers method (Press & Flannery, 1988).

2.2.3 Mie theory

The small particle limit of the Mie thoery, the Rayleigh approximation, is not appropriate in our case, so the full Mie theory (Mie, 1908; Boren & Huffman, 1983; Wolf & Voshchinnikov, 2004) has to be used. Mie theory yields the extinction, scattering, and absorption efficiency factors ($Q_{\rm ext}$, $Q_{\rm sca}$, $Q_{\rm abs}$), which are given by

$$Q_{ext} = \frac{2}{x^2}\sum_{n=1}^{\infty}(2n+1)Re(a_n + b_n) \tag{2.2.6}$$

$$Q_{sca} = \frac{2}{x^2}\sum_{n=1}^{\infty}(2n+1)(|a_n|^2 + |b_n|^2) \tag{2.2.7}$$

$$Q_{abs} = Q_{ext} - Q_{sca}, \tag{2.2.8}$$

with size parameter $x = 2\pi a/\lambda$ (a: grain radius, λ: wavelength of light) and the Mie coefficients a_n and b_n:

$$a_n = \frac{\psi_n'(mx)\psi_n(x) - m\psi_n(mx)\psi_n'(x)}{\psi_n'(mx)\zeta_n(x) - m\psi_n(mx)\zeta_n'(x)} \tag{2.2.9}$$

$$b_n = \frac{m\psi_n'(mx)\psi_n(x) - \psi_n(mx)\psi_n'(x)}{m\psi_n'(mx)\zeta_n(x) - \psi_n(mx)\zeta_n'(x)}, \tag{2.2.10}$$

where

$$\psi_n(x) = xJ_n(x) \tag{2.2.11}$$

$$\zeta_n(x) = \psi_n(x) - ixY_n(x) \tag{2.2.12}$$

The spherical Bessel function of 1st kind is denoted as $J_n(x)$ and the spherical Bessel function of 2nd kind is $Y_n(x)$ (Bronstein & Semendjajew, 1997). As given by EMT, $m = n + \imath k$ is the refractive index of the material.
Now, absorption and scattering efficiency factors are known, which can easily be transformed to cross sections (Ferguson et al., 2005) by

$$C_{\rm abs} = \pi a^2 Q_{\rm abs} \tag{2.2.13}$$

$$C_{\rm sca} = \pi a^2 Q_{\rm sca} \tag{2.2.14}$$

and with the known gas density and number density of grains transformed to opacities:

$$\kappa = n_d C_{\rm abs} \tag{2.2.15}$$

$$\sigma = n_d C_{\rm sca}. \tag{2.2.16}$$

These opacities are used by the atmosphere code PHOENIX (Hauschildt & Baron, 1999) in order to solve the radiative transport problem which yields the synthetic spectrum.

2.3 Convection

Besides radative transfer, convection is another important type of energy transport in stellar atmospheres, which is an energy transfer by mass motion.

Schwartzschild criterion

Under the assumption of an ideal gas, stability against convection can be tested with the *Schwartzschild criterion*:

$$\left(\frac{d\ln T}{d\ln p}\right)_R > \left(\frac{d\ln T}{d\ln p}\right)_A \tag{2.3.1}$$

Here, $d\ln T$ is the logarithmic change in temperature and $d\ln p$ the logarithmic change in pressure, either by radiation (R) or adiabatic changes (A). With the definition $\nabla := (d\ln T/d\ln p)$ the criterion can be abbreviated:

$$\nabla_R > \nabla_A$$

So, convections occurs, where the radiative gradient of temperature exceeds the adiabatic gradient. This can be induced by high opacities or a high radiative flux.

Mixing length theory

In astrophysics, mass transport by convection is generally treated with the *mixing-length theory* (MLT) (Biermann, 1932; Mihalas, 1978). In this approximation, mass transport is described by adiabatic mass elements which move up- or downwards. Upward moving elements transfer their thermical energy to their surrounding after a characteristic distance, called *mixing length*. Downward moving elements, absorb energy from the surrounding medium after travelling the mixing length, too.
Due to this energy exchange, the temperature gradient becomes larger compared to the gradient if only radiative transfer is considerd.
If ∇_R denotes the radiative gradient, ∇ the gradient of the final state, where convection and radiation act together, ∇_E the gradient in a convective elements, and ∇_A the adiabatic gradient, the following relation is valid:

$$\nabla_R \geq \nabla \geq \nabla_E \geq \nabla_A \tag{2.3.2}$$

The pressure scale height H_p is the distance, on which the local pressure changes by a factor of $1/e$ and can be expressed by

$$\frac{1}{H_p} = -\frac{d\ln p}{dr} = \frac{g\rho}{p}, \tag{2.3.3}$$

where g is the surface gravity, C_p the heat capacity at constant pressure, and $Q = 1 - (\partial\ln\mu/\partial\ln T)_p$. Then, the convective flux F_{conv} is given by

$$F_{\text{conv}} = \frac{1}{4}\sqrt{\frac{gH_pQ}{2}}(\rho C_pT)(\nabla - \nabla_E)^{3/2}\left(\frac{l}{H}\right)^2 \tag{2.3.4}$$

and the convection speed is

$$v_{\rm conv} = \frac{1}{2\sqrt{2}} \, (gQH_p)^{1/2} \, (\nabla - \nabla_E)^{1/2} \, \frac{l}{H_p}. \tag{2.3.5}$$

The choice of the mixing length l is a free parameter and can only be estimated. Typical values are $l/H_p = 1 \ldots 3$ (Ludwig et al., 2002).

2.4 Radiative transfer

Detailed descriptions of the radiative transfer problem are found in e.g. Unsöld (1955); Mihalas (1970, 1978); Rutten (2002) on which the following sections are based.
Radiation is described by a beam of light of the wavelength λ through several layers of the atmosphere. If the atmosphere is thin compared to the stellar (or substellar) object, the layers can be assumed to be plan-parallel. In one dimension, the radiative flux can be written as

$$F_\lambda = \oint I_\lambda \, \mu \, d\mu, \tag{2.4.1}$$

where I_λ is the wavelength dependent specific intensity and $\mu = \cos\varphi$ is the angle between the beam ray and the surface normal. The mean intensity J_λ is defined by

$$J_\lambda(z,t) = \frac{1}{2} \int_{-1}^{1} I_\lambda(z,\mu,t) \, d\mu. \tag{2.4.2}$$

Each infinitesimal layer can absorb, scatter or amplify the light by dI_λ. In the case of absorption and scattering, dI_λ is proportional to I_λ:

$$dI_\lambda = -\kappa_\lambda \, I_\lambda \, ds \qquad \text{(absorption)} \tag{2.4.3}$$

$$dI_\lambda = -\sigma_\lambda \, I_\lambda \, ds \qquad \text{(scattering)}. \tag{2.4.4}$$

Here, ds denotes the infinitesimal thickness of a layer, κ_λ is the absorption and σ_λ the scattering coefficient, which are often summed up as extinction coefficient $\chi_\lambda = \kappa_\lambda + \sigma_\lambda$. The case of emission is independent of I_λ and is written as

$$dI_\lambda = \eta_\lambda \, ds \qquad \text{(emission)}. \tag{2.4.5}$$

The wavelength dependent optical depth τ_λ is defined by

$$\begin{aligned} d\tau_\lambda &= \chi_\lambda \, ds \\ &= -\chi_\lambda \, \mu \, dz. \end{aligned} \tag{2.4.6}$$

The definition in the second line of eq. 2.4.6 indicates the case of a different angle than 0° between beam and axis of symmetry z. The decline of intensity by extinction can also be expressed in terms of optical depth with

$$dI_\lambda = I_\lambda d\tau_\lambda. \tag{2.4.7}$$

One wavelength independent optical depth can be defined with the *Rosseland-mean* opacity $\kappa_{\rm ross}$, which is defined as

$$\frac{1}{\kappa_{\rm ross}} = \frac{\pi}{4\sigma T^3} \int_0^\infty \frac{1}{\kappa_\lambda} \frac{\partial B_\lambda}{\partial T} d\lambda. \tag{2.4.8}$$

2.4.1 Schwarzschild equation

If a beam of light traverses a thin layer of matter, its energy may increase by additional emission coming from the layer or it declines by absorption or scattering by an amount dI:

$$dI_\lambda \, ds \, d\lambda = (\eta_\lambda(s) - \chi_\lambda(s) I_\lambda(s)) \, ds \, d\lambda, \tag{2.4.9}$$

which can also written as

$$\frac{dI_\lambda}{ds} = \eta_\lambda(s) - \chi_\lambda(s) I_\lambda(s). \tag{2.4.10}$$

With definition of the *source function*

$$S_\lambda = \frac{\eta_\lambda}{\chi_\lambda} \tag{2.4.11}$$

and use of optical depth τ_λ, equation 2.4.10 can be written as

$$\frac{1}{\mu}\frac{dI_\lambda}{d\tau_\lambda} = I_\lambda - S_\lambda \qquad \text{(plane-parallel equation of transfer).} \tag{2.4.12}$$

Formally speaking, this is a first order differential equation with a constant coefficient and with the integrating factor $e^{-\frac{\tau}{\mu}}$, which yields

$$\frac{d}{d\tau}\left(I e^{-\frac{\tau}{\mu}}\right) = -\frac{1}{\mu} S e^{-\frac{\tau}{\mu}} \tag{2.4.13}$$

and has its formal solution

$$I(\tau_1, \mu) = I(\tau_2, \mu)\, e^{-\frac{\tau_2 - \tau_1}{\mu}} + \int_{\tau_1}^{\tau_2} S(t)\, e^{-\frac{t-\tau_1}{\mu}} \frac{dt}{\mu}. \tag{2.4.14}$$

Keeping in mind the dependency of S from I, the solution of 2.4.14 is not trivial. With the assumption of the special case of an optical deep atmosphere ($\lim \tau \to \infty$), an expression of inward and outwards radiation at distinct optical depth τ is given (Unsöld, 1955):

$$\text{Outwards radiation:} \quad I_{(\mu>0)}(\tau, \mu) = \int_\tau^\infty S(t) e^{\frac{t-\tau}{\mu}} \frac{dt}{\mu} \tag{2.4.15}$$

$$\text{Inward radiation:} \quad I_{(\mu<0)}(\tau, \mu) = -\int_0^\tau S(t) e^{\frac{t-\tau}{\mu}} \frac{dt}{\mu} \tag{2.4.16}$$

The mean intensity (see equation 2.4.2) is given by integration along the angle $\mu = \cos\varphi$:

$$J(\tau) = \frac{1}{2}\int_0^1 \int_\tau^\infty S(t) e^{-\frac{t-\tau}{\mu}} \, dt \, d\mu - \frac{1}{2}\int_{-1}^0 \int_0^\tau S(t) e^{-\frac{\tau - t}{\mu}} \, dt \, d\mu \tag{2.4.17}$$

Via substitution and transformation, the *Schwarzschild Equation*

$$J(\tau) = \frac{1}{2}\int_0^\infty S(t) E_1(|t - \tau|) dt \tag{2.4.18}$$

with exponential integral

$$E_n(x) = \int_1^\infty \frac{e^{-xt}\, dt}{t^n}$$

is found.

2.4.2 Solution with Λ-operator

The Schwarzschild equation can be solved by an iterative method, which will be described in this chapter. Equations in the format of equation 2.4.18 often occur in treatment of radiation transfer. Thus, a Λ-operator for the plane-parallel case is defined as abbreviation:

$$\Lambda_\tau[f(t)] := \frac{1}{2}\int_0^\infty f(t)E_1|t-\tau|dt \tag{2.4.19}$$

The source function which includes thermal emission and scattering can be written as follows:

$$\begin{aligned} S_\lambda &= \frac{\kappa_\lambda}{\kappa_\lambda+\sigma_\lambda}B_\lambda + \frac{\sigma_\lambda}{\kappa_\lambda+\sigma_\lambda}J_\lambda \\ &\equiv (1-\rho_\lambda)B_\lambda + \rho_\lambda J_\lambda. \end{aligned} \tag{2.4.20}$$

Thus, the ansatz in equation 2.4.14 is only a formal solution as it is an integro differential equation, which cannot be solved analytically. (B_λ is the Planck function.) The solution of 2.4.14, written with the Λ operator is

$$\begin{aligned} J_\lambda(\tau_\lambda) &= \Lambda_{\tau_\lambda}[S_\lambda(t_\lambda)] \\ &= \Lambda_{\tau_\lambda}[B_\lambda] + \Lambda_{\tau_\lambda}[\rho_\lambda(J_\lambda - B_\lambda)]. \end{aligned} \tag{2.4.21}$$

This integral equation can be solved by iteration. $J_\lambda \to B_\lambda$ for $\tau_\lambda \to \infty$, so $J_\lambda^{(0)} = B_\lambda$ is the useful starting point. The iteration scheme becomes

$$J^{(i+1)} = \Lambda_{\tau_\lambda}[S_\lambda^{(i)}(t_\lambda)] \tag{2.4.22}$$

$$S_\lambda^{(i+1)} = (1-\rho_\lambda)B_\lambda + \rho_\lambda J_\lambda^{(i+1)}. \tag{2.4.23}$$

Accelerated lambda-iteration

In the range of $\tau > 1$ and $\rho \to 1$, the Λ iteration does not converge (Rutten, 2002), as $\Lambda[S] \approx S$ there. Hence, this method is inappropriate for the solution of scattering dominated problems. A better convergence behaviour can be obtained by the Operator Splitting (OS) method (Cannon, 1973; Scharmer, 1981). The operator is split

$$\Lambda_{\tau_\lambda} = \Lambda^*_{\tau_\lambda} + (\Lambda_{\tau_\lambda} - \Lambda^*_{\tau_\lambda}), \tag{2.4.24}$$

so the solution can be written as (similar to equation 2.4.21):

$$J_\lambda^{(i+1)}(\tau_\lambda) = \Lambda^*_{\tau_\lambda}[S_\lambda^{(i+1)}] + \left(\Lambda_{\tau_\lambda} - \Lambda^*_{\tau_\lambda}\right)[S_\lambda^{(i)}] \tag{2.4.25}$$

Resolved explicitly to $J_\lambda^{(i+1)}$, one obtains (neglecting the indices):

$$J^{(i+1)} = [1-\rho\Lambda^*]^{-1}\left(\Lambda S^{(i)} - \rho\Lambda^* J^{(i)}\right) \tag{2.4.26}$$

The complexity lies in the determination of an appropriate Λ^*, which is described in detail in Hauschildt & Baron (1999).

Chapter 3

Approach

A stand-alone application of the dust model is already shown in detail in Woitke & Helling (2004). There prescribed brown dwarf atmosphere structures of different effective temperatures (Tsuji, 2002) were applied to the dust model. Only TiO_2, both as nucleation seed and as growth species, was considered. On the other hand, Helling et al. (2007) present a dust model for truly heterogeneous dust grains coupled to the process of gravitational settling. Even if the prescribed atmosphere structures are based on calculations which include dust formation, they do not resemble the structure which would be generated with the current dust model connected to a radiative transfer code.[1]
In the present application the dust treatment of Woitke & Helling (2003, 2004); Helling & Woitke (2006); Helling et al. (2007) (hereafter called **DRIFT**) is incorporated with the stellar atmosphere code PHOENIX. PHOENIX was initially created in order to calculate supernova atmospheres but was improved and enhanced over the years to handle cool stars and brown dwarfs (Hauschildt, 1992; Allard & Hauschildt, 1995; Allard et al., 1997; Hauschildt et al., 1997; Baron & Hauschildt, 1998; Hauschildt & Baron, 1999; Hauschildt et al., 1999a,b; Allard et al., 2000; Hauschildt et al., 2001). In Allard et al. (2001), a simple treatment of dust in brown dwarfs in connection with PHOENIX is described. The so called COND and DUSTY models are defined there. (See also chapter 1.2)
Details of the implementation can be found in the appendix (A.2.1).

3.1 Simplified flow chart of PHOENIX

Regarding the structure of PHOENIX itself, dust treatment is

(a) a drain of chemical elements (if grains form and deplete the gas phase) or a source of them (if grains evaporate and enrich the gas phase), which has to be considered in solving the equation of state, the gas phase chemistry, line opacities etc., and

(b) an additional source of opacity besides atomic or molecular opacities, which plays

[1] A workshop was held in Leiden where scientists meet to quantify such possible uncertainties. (`http://www.lorentzcenter.nl/lc/web/2006/203/info.php3?wsid=203`)

a role in the solution of radiative transfer and finally in computing the atmosphere structure.

A simplified flow chart of a PHOENIX run for an application to static (e.g. no winds) cool stars is given as follows:

1. **Input of previous model (initial data):**
   Reading the temperature, gas pressure and density structure as initial values.

2. **Solving equilibrium chemistry:**
   More than 600 molecules and ions can be considered in the calculation of the equilibrium chemistry. Dissociation constants of the molecules are found in the JANAF-tables (Chase et al., 1985). The complete equilibrium equations are solved simultaneously by a Newton-Raphson iteration. (Allard & Hauschildt, 1995; Allard et al., 2001; Ferguson et al., 2005)

3. **Solving the atmosphere structure:**
   A temperature-pressure profile is calculated by solving the hydrostatic equation. Convective flux using mixing length theory (MLT) is also included.

4. **For every given wavelength:**

   (a) **Calculation of opacities:**
   Continuous opacity sources (bound-free and free-free processes), atomic lines, molecular bands, and dust opacities are calculated, depending on local pressure and temperature. Several (8×10^8) atomic and molecular lines can be considered (Ferguson et al., 2005).

   (b) **Radiation transfer and spectrum:**
   The radiation transport problem is solved via accelerated Λ-iteration with the opacities calculated above (Hauschildt, 1992; Hauschildt & Baron, 1999).

5. **Temperature correction:**
   PHOENIX adjusts the temperature structure with an Unsöld-Lucy temperature correction (Hauschildt et al., 2003). This alters T in each layer, so the atmospheric structure will be readjusted in the next iteration.

After the temperature corrections, the next iteration starts again at 1. If the temperature corrections are small enough ($\Delta T < 0.5 \ldots 2.0$ K, depending on settings) or after a specified number of iterations, the program stops and and returns the atmospheric structure and the spectrum. Usually, the current temperature corrections always exceed the termination conditions at lower effective temperatures ($T_{\rm eff} < 2600$ K) with lower dust opacities. Then, a model is considered to be converged, if an error in radiative flux is below $\approx 5 \ldots 10\%$ in each layer. A model usually converges after 5 to 20 iterations.

3.2 The DRIFT module

The DRIFT module is an independent subroutine which can be easily converted into a stand-alone program. In order to facilitate data transfer, error tracking, and sharing results, all properties are exchanged between via data files. For the treatment of nucleation, growth and evaporation, gravitational settling, and convective mixing, DRIFT needs the following layer dependent properties:

→ Atmospheric structure ($T(z)$ in K, $P_{\rm gas}(z)$ in bar, $\rho(z)$ in g cm^{-3}, z in cm)

→ Mean molecular mass ($\mu(z)$ in u = $1.6605402 \cdot 10^{-24}$ g)

→ Convection speed ($v_{\rm conv}(z)$ in cm s^{-1})

→ Element abundances (ε_i^0)

On the other hand, after the solution of the dust moment equation (2.1.22), the following layer dependent properties are available:

← Mean dust number density and radius ($n_d(z)$ in cm^{-3}, $<a>$ (z) in μm)

← Depletion of elements ($\varepsilon_i(z)$)

Furthermore, nucleation rate (J^*), net growth ($\chi_{\rm net}$), saturation ratios (S), drift velocity ($v_{\rm drift}$), mixing timescale ($\tau_{\rm mix}$), and fraction of grain components are also available and interesting for a detailed analysis.
As DRIFT needs the convection speed $v_{\rm conv}$ to determine the mixing time scale $\tau_{\rm mix}$, and $v_{\rm conv}$ is not saved in the input model structure, the invocation of DRIFT is done after the hydrostatic structure is solved in PHOENIX (item 3). This leads to the problem, that element depletion in the atmosphere is not considered while solving the equilibrium chemistry. Avoidance of this hen-and-egg problem is simple, if initial models start at high effective temperatures (e.g. $T_{\rm eff} = 3000$ K), where no dust forms at all. Then, while decreasing $T_{\rm eff}$ step by step, element depletion is saved with every model run and read in at startup. On the other hand, PHOENIX calculates opacities before performing the radiative transfer, so DRIFT has to be finished before (item 4). With given dust properties, the dust opacities $\kappa_{\rm dust}$ and scattering $\sigma_{\rm dust}$ are calculated (see chapter 2.2).

At the present state, DRIFT knows how to handle seven distinct dust species (Al_2O_3, Fe, MgO, $MgSiO_3$, Mg_2SiO_4, SiO_2, and TiO_2) for which several growth reactions are considered (See section A.2.2 for a complete list of reactions). Additionally, TiO_2 is the nucleation species. PHOENIX and DRIFT calculate equilibrium chemistry on their own, which means that the routines and data sets are different.
In order to ensure proper results in the chemistry calculations, equilibrium constants (K_p) of 33 common used species have been checked in the temperature range from 500 to 4000 K. Constants of 30 species agree with an accuracy better than 20%[2] (1 of them better than 10%, 16 < 5%, and 10 < 1%), but the K_p of the ions $C2^-$, CN^-, NO^+,

[2]The accuracy is here defined as $10^{\frac{2|\mathcal{K}_1-\mathcal{K}_2|}{|\mathcal{K}_1+\mathcal{K}_2|}} - 1$, with $\mathcal{K}_i = \int \log_{10}(K_{pi}(T))\, dT$, distinct equilibrium constants K_{p1}, K_{p2}, and integration in the range of 500 to 4000 K.

and $AlOH^+$ completely disagree. Partial pressures of the latter four are more than 12 orders of magnitudes smaller than the partial pressures of H_2 in each atmosphere layer in a model with $T_{\rm eff} = 1500$ K. Hence, their deviations in K_p can be neglected. A complete list of molecules and their agreement of K_p is found in table 3.1. A comparison of K_p(FeS) and K_p(AlH) is shown in Figure 3.1. These molecules are chosen because their range $|K_p(\mathrm{T} = 500\,\mathrm{K}) - K_p(\mathrm{T} = 4000\,\mathrm{K})|$ is quite small which makes deviations easily visible.

$< 20\%$	$< 10\%$	$< 5\%$	$< 1\%$
FeS, AlO_2, AlO	AlS	H_2, CO, CO_2, CN, C_2, N_2, TiO, TiO_2, NH, TiS, SiO, FeO, NO, AlOH, AlH, MgH,	CH_4, H_2O, SiS, SiO_2, $Mg(OH)_2$, CH, OH, SiH, $Fe(OH)_2$, CO_2^-

Table 3.1: List of molecules, which equilibrium constants K_p in PHOENIX and DRIFT were examined. According to their agreement, they are divided into the columns with 20, 10, 5 and 1% accuracy.

3.3 Model parameters

The DRIFT-module was adapted for plan parallel atmospheres. For consistency, calculations in PHOENIX are also made in this approximation. In order to summarise this chapter, the required input parameters are listed which determine a model:

- **Input parameter**
  - **Stellar parameter**
    The following parameters sufficiently determine the objects:
    $T_{\rm eff}$, $\log g$, and ε_i^0 (e.g. solar abundances)
  - **Parameter ranges**
    In order to represent late-M and L dwarfs, the following parameter ranges were selected:
    * $T_{\rm eff} = 3000 \ldots 1400$ K
    * $\log g = 4.0 \ldots 6.0$
    * $[\mathrm{Fe/H}] = 0.0 \ldots -1.0$
  - **Dust parameters**
    There are no free parameters needed for the dust formation. In some rare cases, parameters of microphysical quantities are set. (E.g. the sticking coefficient α_r, which is set to unity, see Section 2.1.2).
  - **Treatment of mixing**
    The importance of mixing time $\tau_{\rm mix}$ was discussed previously (see section 2.1.4 and Woitke & Helling (2004)). In the current treatment, the mixing time $\tau_{\rm mix}$ does not depend on a freely chosen minimum mixing time $\tau_{\rm mix}^{\rm min}$ (see eq 2.1.21) anymore. Instead, $\tau_{\rm mix}^{\rm min}$ is determined by the convection speed ($\tau_{\rm mix}^{\rm min} = l/(H_p v_{\rm conv})$).

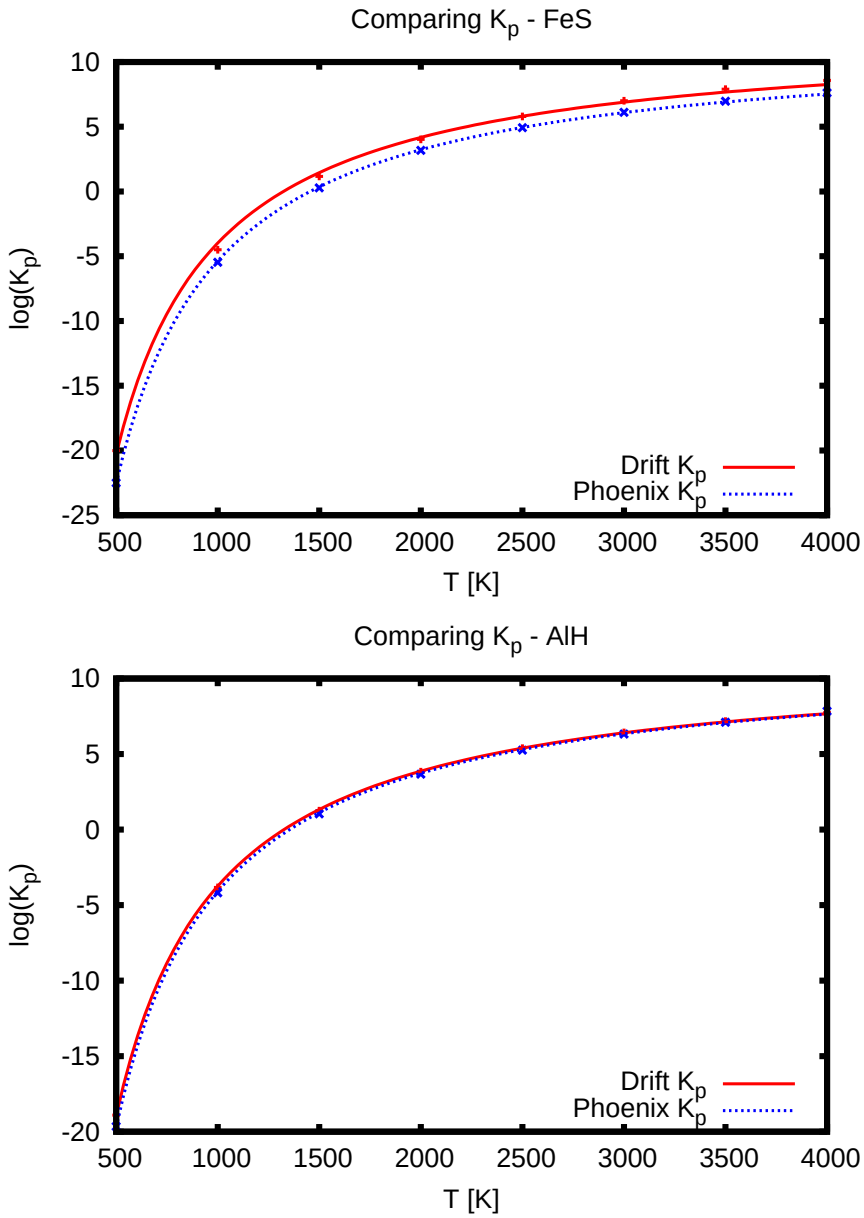

Figure 3.1: Equilibrium constants of FeS (error <20%) and AlH (<5%) in DRIFT and PHOENIX models at temperatures between $T = 500 \ldots 4000$ K. The lines correspond to a function $a/T + b$ fitted to the data points.

* **Mixing length**
  The convection $v_{\rm conv}$ speed depends on the mixing length l/H_p. Its value is still discussed and can be set to 2 for M and L-dwarfs (Ludwig et al., 2002).
* **Overshoot parameter**
  The value of $\beta = d\log(\tau^{-1})/d\log P$ was determined to be 2.2, according to calculations of Ludwig et al. 2002 (Figure 16).

The following list gives an outline of the physical output quantities:

- **Output quantities**
  - **Hydrostatic properties**
    - Temperature profile $T(z)$ [K]
    - Gas pressure profile $P_{\mathrm{gas}}(z)$ [bar]
    - Partial pressures of species $P_i/P_{\mathrm{gas}}(z)$
    - Gas density profile $\rho(z)$ [g cm^{-3}]
    - Mean molecular mass $\mu(z)$ [amu]
    - Convection speed $v_{\mathrm{conv}}(z)$ [cm s^{-1}]
    - Mixing time $\tau_{\mathrm{mix}}(z)$ [s]
  - **Dust properties**
    - Dust number density $n_d(z)$ [cm^{-3}]
    - Mean grain radius $<a>$ (z) [μm]
    - Width of grain size distribution (see 2.1.5) $|a_1 - a_2|(z)$ [μm]
    - Nucleation rate $J^*(z)$ [cm^{-3} s^{-1}]
    - Growth rate $\chi_{\mathrm{net}}(z)$ [cm s^{-1}]
    - Abundances modified via depletion $\varepsilon_i(z)$
    - Components volume fraction in a grain
  - **Optical properties**
    - Complex refractory indices of dust $m(z, \lambda)$
    - Absorption coefficient of dust $\kappa_{\mathrm{dust}}(z, \lambda)$ [cm^{-1}]
    - Scattering coefficient of dust $\sigma_{\mathrm{dust}}(z, \lambda)$ [cm^{-1}]
    - Optical depth $\tau_{1.2\mu\mathrm{m}}(z)$ and Rosseland depth $\tau_{\mathrm{ross}}(z)$
  - **Spectral properties**
    The spectral flux $F(\lambda)$ [erg s^{-1} cm^{-1} cm^{-2}]

Chapter 4

Results

This part considers at first very detailed results on dust formation and focusses then more on observable properties.

4.1 Detailed dust cloud structure

In this section, a brown dwarf model with $T_{\rm eff} = 1600$ K, $\log g = 5.0$, and solar composition (Grevesse et al., 1992) will be examined in detail. Its temperature profile is presented in Figure 4.1. This and subsequent diagrams always use the same gas pressure range from 10^{-8} to 10^{2} bar to allow an easy comparison. The temperature curve

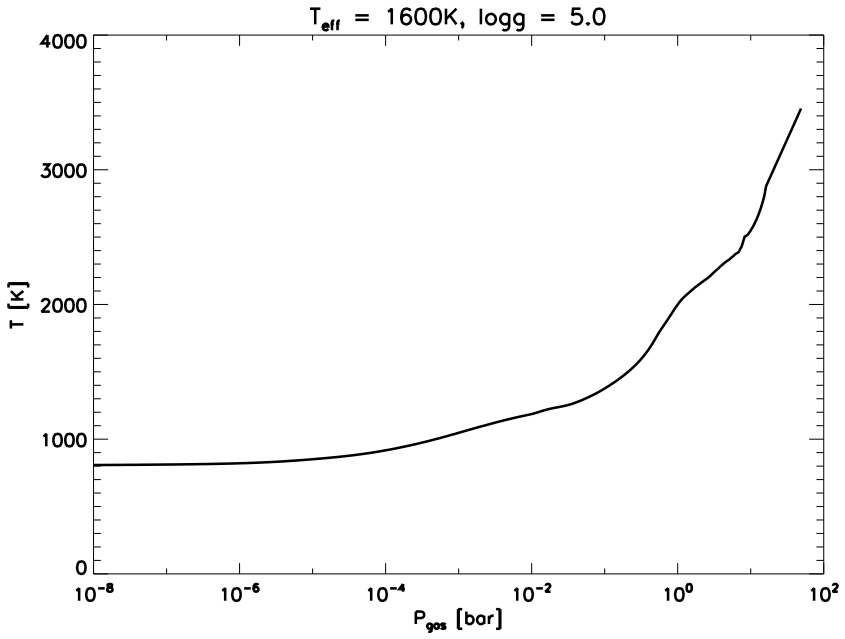

Figure 4.1: Temperature [K] of a brown dwarf with $T_{\rm eff} = 1600$ K and $\log g = 5.0$ as function of $P_{\rm gas}$.

shows at least one significant bump at $P_{\rm gas} \approx 1$ bar. It is induced by backwarming and

coincides with the occurence of dust, which is seen in the next section.

4.1.1 Nucleation rate and particle number density

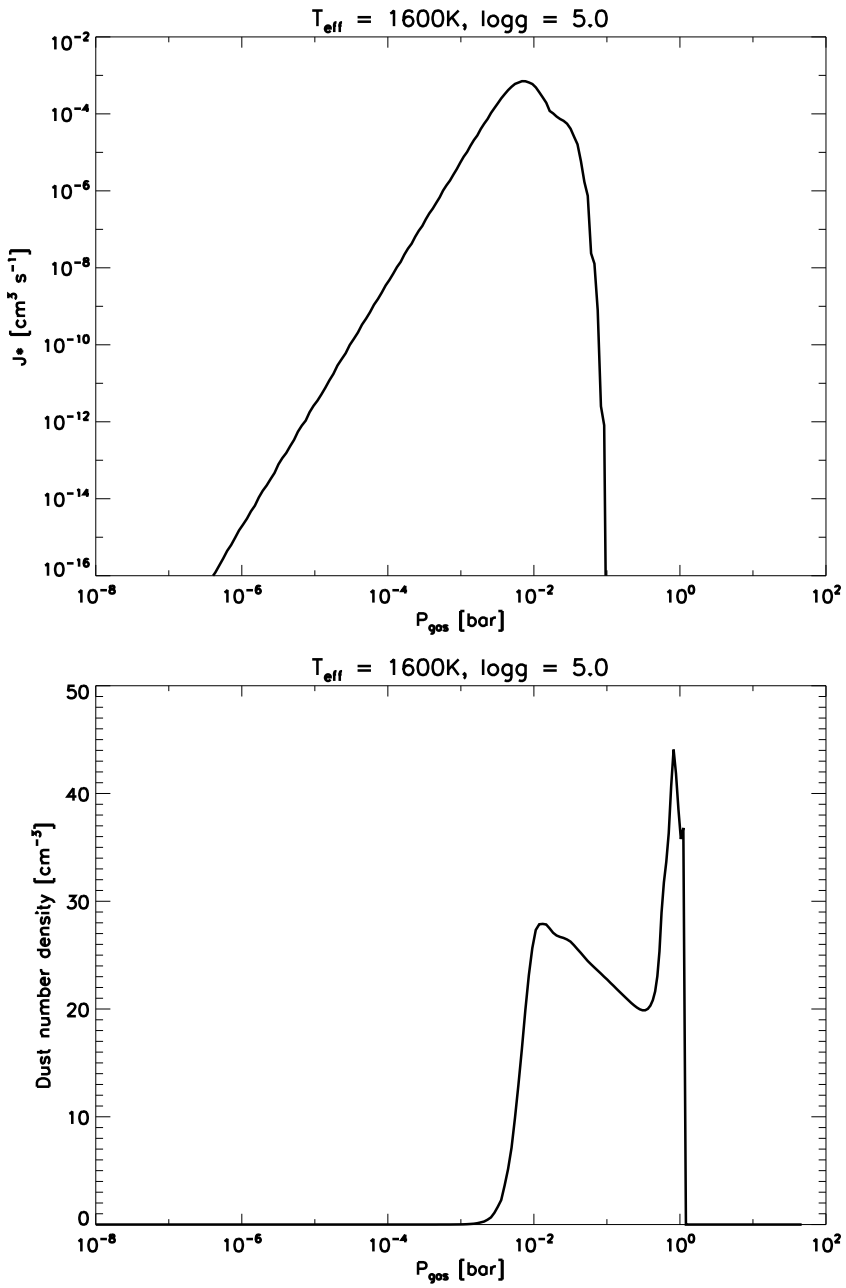

Figure 4.2: The nucleation rate J^* [$\mathrm{cm}^{-3}\,\mathrm{s}^{-1}$] (top) and dust particle number density n_d [cm^{-3}] (bottom) as function of local pressure P_{gas} [bar]. J^* peaks at $P_{\mathrm{gas}} = 7{\cdot}10^{-3}$ bar, causing a rise of particle numbers there.

It is seen in Figure 4.2, that high nucleation rates cause a rise in the particle number

density. For $P_{\rm gas} = 10^{-6}$ bar the nucleation rate reaches values of 10^{-15} cm^3 s^{-1} and increases slowly until $P_{\rm gas} = 10^{-3}$ is reached. The peak of J^* at $7 \cdot 10^{-4}$ cm^3 s^{-1} is found at $P_{\rm gas} = 7 \cdot 10^{-3}$ bar, which is the regime where n_d raises fastest for the first time. In deeper atmosphere layers where $P_{\rm gas} > 10^{-1}$ bar, the nucleation rate is zero. If a distinct local temperature is exceeded (here 1400 K), J^* drops very fast (see characteristics of J^* in A.1.1).
A significant concentration of dust grains is seen between 10^{-2} and 1 bar. After the first rise up to 30 grains per cm^3 at 10^{-2} bar, an unexpected drop to 20 grains per cm^3 at 0.4 bar is visible. Within a small range of the atmosphere, a second peak of 45 cm^{-3} at 1 bar is reached, which drops to zero quickly. J^* is zero at these deep atmosphere layers and plays no role anymore. Thus, the occurrence of the decay zone and the deeper second peak cannot be explained by nucleation formalism: It will be shown in a few sections that the drift velocity plays a major role here.

4.1.2 Growth velocity and mean grain size

To understand the behaviour of the mean grain sizes $<a>$, the influence of $\chi_{\rm net}$ is demonstrated. Net grain growth is taken place where $\chi_{\rm net} > 0$, and a net evaporation takes place where $\chi_{\rm net} < 0$. As shown in Figure 4.3, a first efficient growth period of grains occurs at $P_{\rm gas} = 1.6 \cdot 10^{-5}$ bar. Only very few grains exist, because the nucleation rate still is very small there. In layers with $P_{\rm gas} = 3 \cdot 10^{-5}$ to $3 \cdot 10^{-3}$ bar, grain radii remain constant at 0.01 μm.Grains do not exist at very low pressures ($P_{\rm gas} < 10^{-6}$ bar). Thus, the mean grain radiu are artifically set to the equivalent of 1000$\times$ the volume of TiO_2 (see 2.1.4) in these layers.
The second growth occurs at $P_{\rm gas} = 0.3$ bar, where much more grains exist. At the same pressure, between 0.1 to 1 bar, the grain radii increase up to 1.2 μm. Both parts of the atmosphere, where $<a>$ increases correspond very well to $\chi_{\rm net} > 0$.
A few layers deeper than $P_{\rm gas} = 0.3$ bar, the first evaporation of dust species takes place. The evaporation of all grains is completed at $P_{\rm gas} > 1$ bar, where no dust exists anymore. The rise of the curve is smooth until it reaches its peak. When it starts to decline, some small bumps are visible. Due to a low spatial resolution of the model atmosphere, subtleties are not well resolved in the graph.

In this model, the Rosseland depth $\tau_{\rm ross}$ reaches unity at about 0.43 bar. This coincides with the part of the atmosphere, where $<a>$ reaches its maximum. At the innermost layer, where dust exists ($P_{\rm gas} \approx 1$ bar), $\tau_{\rm ross}$ exceeds 3. This means, that only very little radiation from the inner part of the dust cloud, which is located in optically thick layers (see Figure 4.4) reaches the observer.

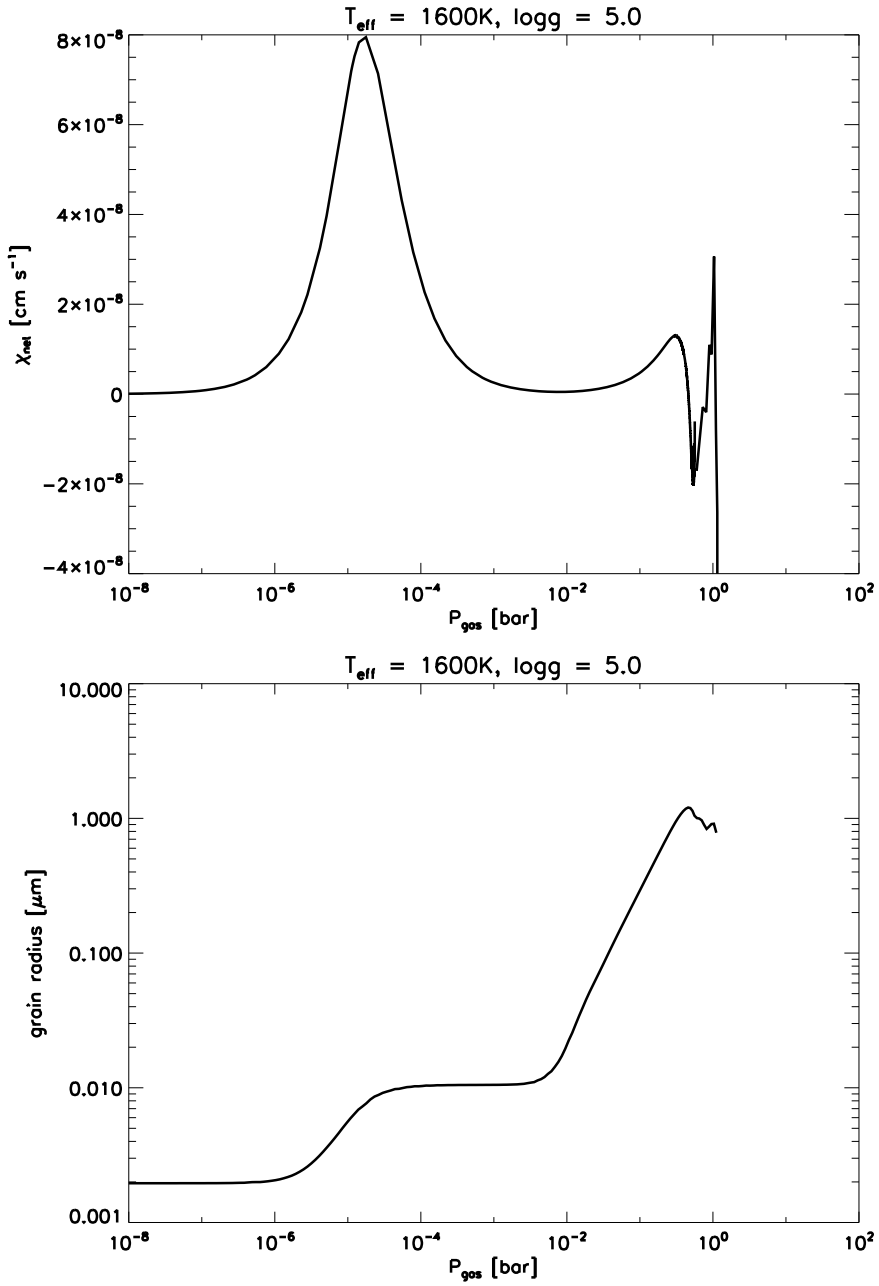

Figure 4.3: Net growth rate $\chi_{\rm net}$ [cm s^{-1}] of an average dust grain (top). Large rates > 0 indicate dominant growth processes, small rates < 0 indicate dominant evaporation processes. The bottom figure shows the mean grain size $<a>$ [μm] as function of local gas pressure $P_{\rm gas}$ [bar].

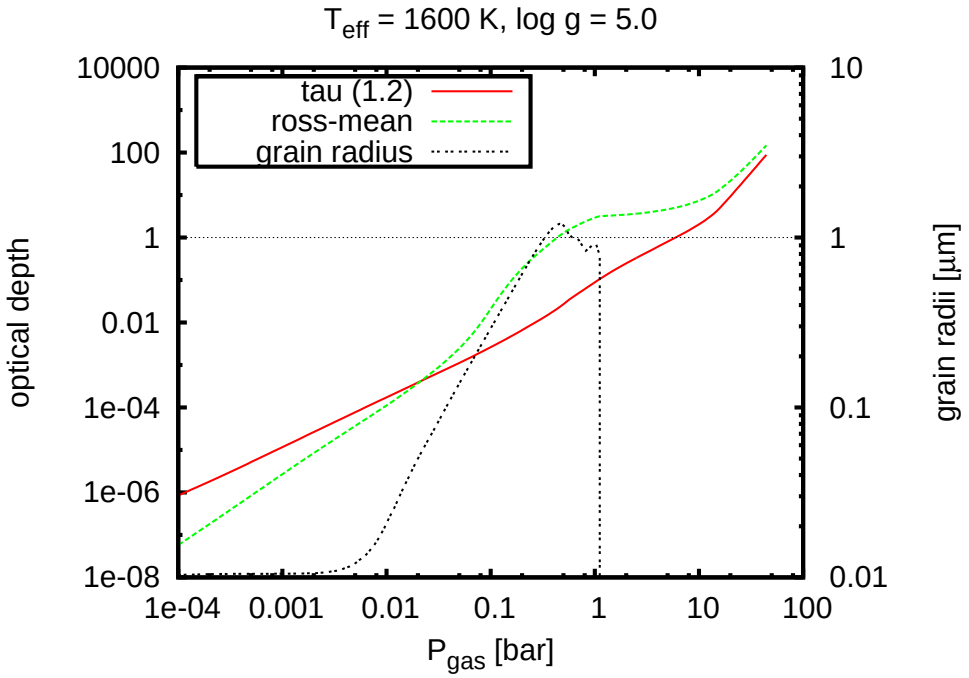

Figure 4.4: Rosseland depth $\tau_{\rm ross}$, optical depth τ at 1.2 μm (left axis), and mean grain radii (right axis) as function of gas pressure $P_{\rm gas}$ [bar].

4.1.3 Drift velocities

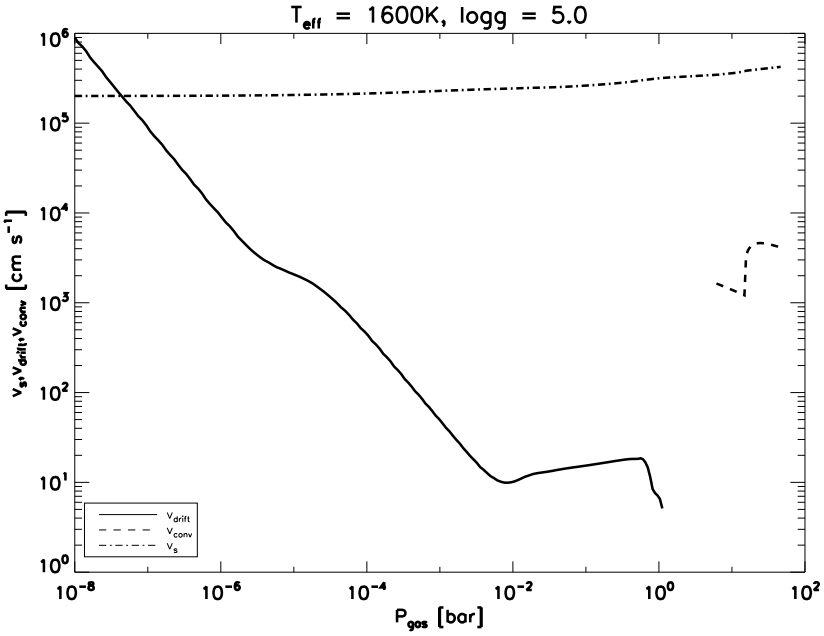

Figure 4.5: Velocities in the model atmosphere: Drift velocity of grains is denoted with $v_{\rm drift}$ (solid line), $v_{\rm conv}$ is the convective speed (dashed line), and v_s is the sonic speed (dash-dot line).

The connection of grain size and drift velocity can be seen very well in Figure 4.5. There, the solid line indicates the drift velocity. The velocity dependency on the grain radii can be seen easily comparing with Figure 4.3:
A rise (or decline) of the grain radius is also seen in the drift velocity, amongst the steady decline caused by $v_{\rm drift} \propto \rho^{-1} \propto P_{\rm gas}^{-1}$ (see Eqn. 2.1.6, ρ is the gas density).
In Figure 4.5, the convection speed, which determines the mixing timescale $\tau_{\rm mix}$, is indicated in the inner parts of the atmosphere ($P_{\rm gas} \approx 10 \ldots 100$ bar) and is given here for comparison. As the dust moment equations applied here are only valid in the subsonic regime, the sound speed is also given. Only in the very outer parts of the atmosphere, the drift velocity exceeds the sound speed. There, the dust moments equations (Eq. 2.1.22) are not valid any more. The different hydrodynamical flow regime needs a different treatment of the frictional force (Woitke & Helling, 2003).
Considering the decay zone (at $P_{\rm gas} \approx 0.1$ bar) and the second peak (at $P_{\rm gas} \approx 1$ bar) in the number density n_d (Figure 4.2), the drift mechanism explains it now. The drift velocity has a local minimum at $P_{\rm gas} = 10^{-2}$ bar and allows grains to cumulate as mentioned before to $n_d = 30$ cm^{-3}. In the region with $P_{\rm gas} = 10^{-2}$ to 1 bar, the drift velocity increases which depopulates the layers from dust. This leads to the decline of n_d in this region. Finally, at 1 bar, due to evaporation, the grain size shrinks, which causes the drift velocity to decrease. Due to this, the grains accumulate again in that region until their final evaporation.
It is clear from the dust moment equation, that everything which influences the dust

moments is coupled to each other. Thus, the drift velocity as well as nucleation rate affects the particle number density, but in different regions of the atmosphere.

4.1.4 Grain composition

In order to calculate the opacity of an heterogeneous dust grain, its composition mut be known. As mentioned before, seven solids are considered in the calculations, which are Al_2O_3, Fe, MgO, $MgSiO_3$, Mg_2SiO_4, SiO_2, and TiO_2. The volume fractions are normalised to unity, which is shown in Figure 4.6: In the outer atmospheric layers, the grains consist only of solid TiO_2, as this is the given nucleation species. This

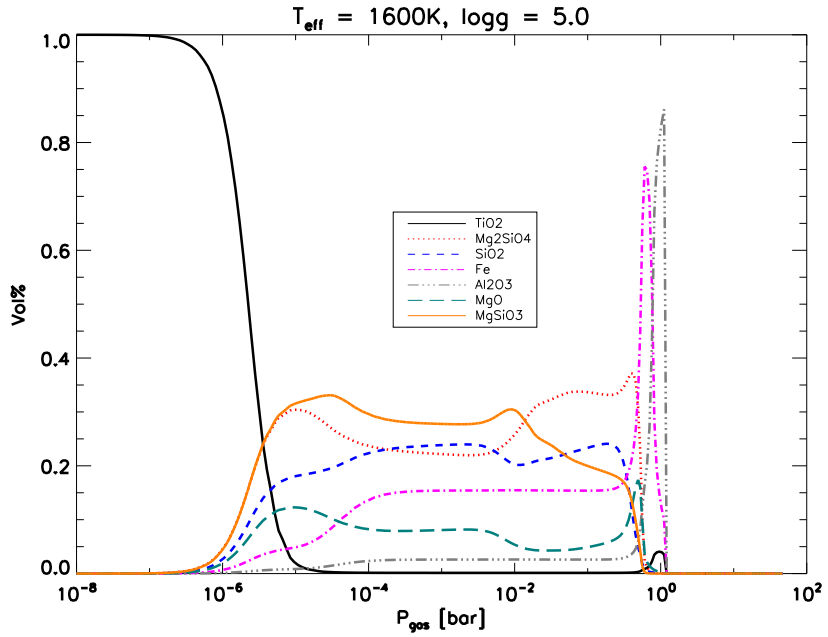

Figure 4.6: This figure shows the volume fraction of each of the seven dust species in a dust grain. All fractions sum up to unity. In the outer part of the atmosphere, only TiO_2 as condensation seed is present, which is edged out going into the more inner parts. Finally, several dust species are evaporating in a sequential order.

changes right after the growth process becomes significant at $P_{\rm gas} < 10^{-6}$ bar (see increasing $\chi_{\rm net}$ in Figure 4.3), where other solids form and the fraction of solid TiO_2 becomes insignificant. At deeper parts of the atmosphere different solids evaporate at different positions. At the end, Fe and Al_2O_3 remain and become the dominant constituents of a grain before it evaporates completely. These two last peaks of iron and corundum are reflected well in $\chi_{\rm net}$ in the same region and consequently in n_d and $<a>$.

4.1.5 Saturation ratios

Figure 4.7 shows saturation ratios S for all considered dust forming solids. It can be seen that very high supersaturation occurs in the upper parts of the atmosphere

($S > 10^6$). At higher temperatures, the saturation ratio drops below unity, showing that the respective solid becomes thermically unstable. $S < 1$ causes evaporation ($\chi_{\rm net} < 0$).

The reason of high saturation ratios is an inefficiency in the growth reactions, which

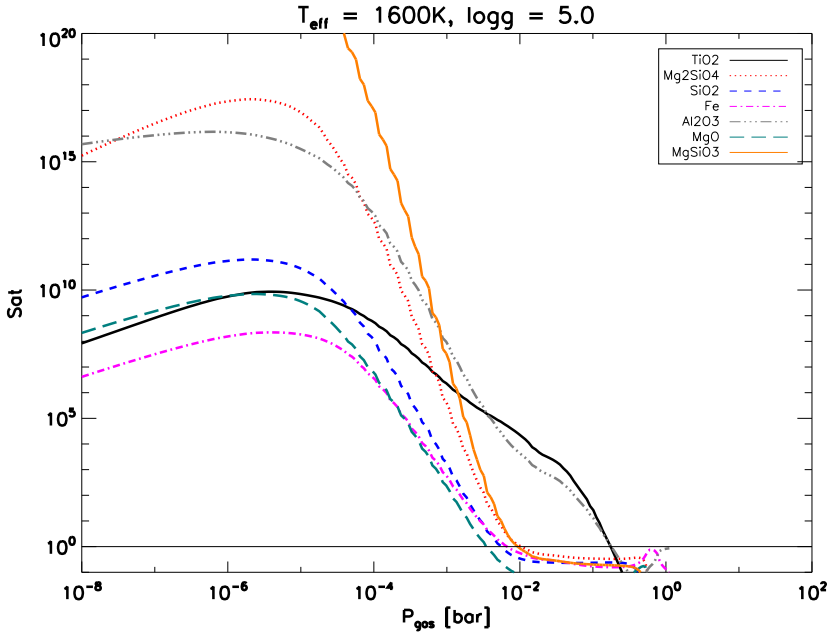

Figure 4.7: Saturation ratios of distinct dust species. The ratios exceed many orders of magnitude in upper atmosphere layers ($P_{\rm gas} < 10^{-3}$ bar) and drop down below unity in the lower ones ($P_{\rm gas} > 3 \cdot 10^{-1}$ bar for TiO_2 and Al_2O_3 and $P_{\rm gas} > 10^{-2}$ bar for the other species).

means that not every gaseous species are consumed, hence, the growth process is not complete. These high ratios disagree with the assumptions made e.g. in Cooper et al. (2003). They assume condensation, where $S - 1 \gtrsim 10^{-3} \ldots 1$.

4.1.6 Cloud structure

Summarising the results presented in the last sections, different cloud regions can be identified. This was done in Woitke & Helling (2004): Regions and calculations are shown for dust particles consisting of pure TiO_2 and some definitions of the cloud structure are based on the ratio $\varepsilon^{\rm dust}_{\rm TiO_2}/\varepsilon^{\rm solar}_{\rm TiO_2}$.

In the present models, more dust species are considered, so the abundance ratio of TiO_2 is not a suitable criterion anymore. The slightly changed criteria of the suggested cloud layers focus more on optically relevant dust properties and do not differentiate between growth or drift dominated regions. This differentiation is difficult because significant grain growth and high drift velocities occur in the same layers (between $P_{\rm gas} = 10^{-2}$ and 1 bar, see Figures 4.3 and 4.5).

0 Dust free atmosphere:
Increasing J^*, but convective mixing is still inefficient and does not allow a significant nucleation.

I Fine particles:
Present results suggest the existence of a region with very small radii (0.01 μm) and very low dust density in the outer atmosphere. The transition from the dust free atmosphere to the region of fine particles is identified with the first maximum of the growth speed ($\chi_{\rm net}|_{\min(P_{\rm gas})} = \chi_{\rm net}^{\rm max}$) in the outermost layers, which is indicated by $\min(P_{\rm gas})$. In these layers, saturation ratios are very high ($S > 10^6$) and nucleations increases gradually, but does not lead to significant dust number density.

II Cloud deck:
The cloud deck is characterized by a strong presence of dust particles, caused by high nucleation rates. Its upper boundary is defined by the maximum of nucleation rate ($J^* = J^*_{\rm max}$). This increase of dust number density also leads to an increase of the dust opacity, shown in 4.4.

III Rain edge:
At a distinct height, the dust grains start to evaporate, because $\chi_{\rm net}|_{\min(P_{\rm gas})} < 0$. Due to the drift, dust grains are not evaporated in only one layer but they move deeper while evaporating.

IV Cloud base:
Finally, every dust grain is evaporated and no dust exists below the cloud base ($n_d = 0$).

These characterisation is illustrative, but differs from Woitke & Helling (2004). There, the cloud deck and the rain edge is defined by $\varepsilon^{\rm dust}_{\rm TiO_2}/\varepsilon^{\rm solar}_{\rm TiO_2} = 1/e$ and the cloud base is identified as phase equilibrium state ($S = 1$).
The local gas pressure of the cloud layers and their thickness for the model with $T_{\rm eff} =$ 1600 K, $\log g = 5.0$, and [Fe/H]= 0.0 is shown in table 4.1. *This structure applies for every model in this work.*

	Description	Condition	Occurence $P_{\rm gas}$ [bar]	Thickness [km]
I	Fine particles	$\chi_{\rm net}\|_{\min(P_{\rm gas})} = \chi_{\rm net}^{\rm max}$	$1.6 \cdot 10^{-5}$	21.4
II	Cloud deck	$J^* = J^*_{\rm max}$	$7.6 \cdot 10^{-3}$	19.8
III	Rain edge	$\chi_{\rm net}\|_{\min(P_{\rm gas})} < 0$	$4.9 \cdot 10^{-1}$	5.9
IV	Cloud base	$n_d = 0$	1.2	—

Table 4.1: Cloud structure of a model with $T_{\rm eff} = 1600$ K, $\log g = 5.0$, and [Fe/H]= 0.0

4.2 Varying the model parameters

In this section, the change of dust properties with varying stellar and mixing input parameters is discussed. The parameter space was explored as follows:

$T_{\rm eff}$ [K]	= 1600,	**2000,**	2400
$\log g$	= 4.0,	**5.0,**	6.0
[Fe/H]	= **0.0,**	−0.5,	−1.0
l/H_p	= 1.0,	**2.0,**	4.0
β	= 2.0,	**2.2,**	2.4

A model with $T_{\rm eff}$ = 2000 K, $\log g$ = 5.0, [Fe/H]= 0.0, l/H_p = 2.0, and β = 2.2 is displayed in every subsection for comparison.

4.2.1 Effective temperature

Figure 4.8 shows the temperature structure of models with $T_{\rm eff}$ = 1600, 2000, 2400 K, $\log g$ = 5.0, and [Fe/H]= 0.0. The hottest model with 2400 K produces a quite smooth curve, where the curve of the coolest model with 1600 K shows significant bumps induced by backwarming. Going from hotter, inner parts of the atmosphere to the cooler, outer parts, the decline in temperature flattens in a small region and becomes steeper afterwards. This behaviour was also found in Allard et al. (2001), and (Tsuji, 2002; Burrows et al., 2006).

In order to locate and display the backwarmed atmosphere layers, the number density

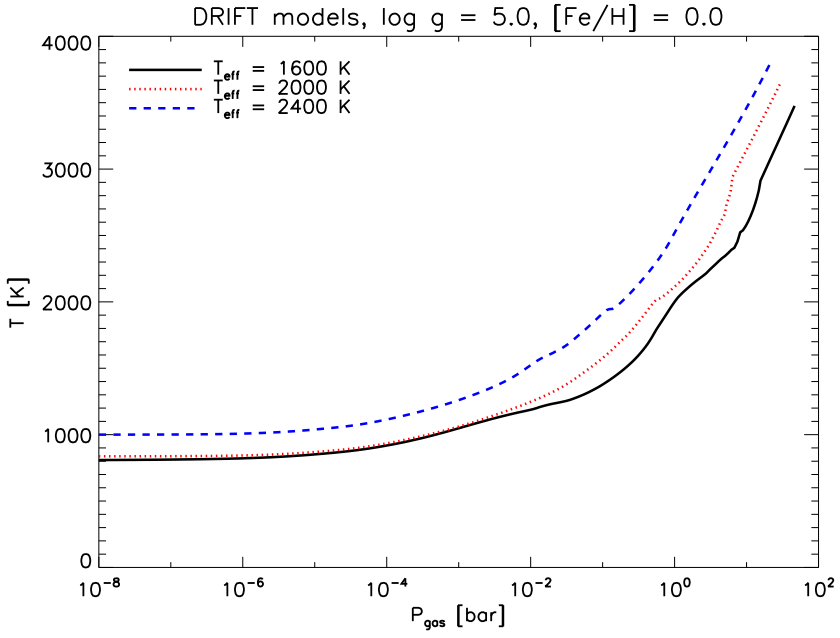

Figure 4.8: Temperature shape of three models with $T_{\rm eff}$ = 1600, 2000, and 2400 K, $\log g$ = 5.0, and [Fe/H]= 0.0

of dust is shown (Figure 4.9) for comparison: The particle number (n_d) has a linear

effect on the dust opacity and the backwarming effect depends on the opacity, which can be seen directly: Where there are peaks in the distribution of n_d, the temperature structure changes from a flattened to a steeper curve one (e.g. $T_{\rm eff} = 1600$ at $P_{\rm gas} = 10^{-2}$ and 1 bar, $T_{\rm eff} = 2400$ K at $P_{\rm gas} = 0.1$ bar). The maximum amount of dust per volume also changes with effective temperature: The model with 2400 K produces about 5 grains per cm^3 and the cool model with 1600 K produces 40 grains per cm^3. It can be seen, that changes in the different temperature profiles result in different positions of the cloud deck and the cloude base. Their positions are shifted by up to one order of magnitude in $P_{\rm gas}$.
It has to be mentioned that the grain composition does not change very much with varying effective temperature; it looks similar to the one seen in Figure 4.6, which is important for the opacity determination (Section 4.4).

Mean grain radii are also shown in Figure 4.9: It turns out that the first growth occurs at the same pressure in the outer atmosphere at about 10^{-3} bar to up to 10^{-2} μm in size for all models. The location of the second growth phase differs also by one order of magnitude in $P_{\rm gas}$ and ends up at a quite similar maximum grain size. The coolest model ($T_{\rm eff} = 1600$ K) shows a maximal radius of 1.2 μm, the hottest model one of 0.6 μm. This fact is very interesting, as other models assume much larger grains in the atmosphere: For example, Burrows et al. (2006) assumes a single radius of 100 μm for all grains. Grain sizes in Ackerman & Marley (2001) depend on the free parameter $f_{\rm rain}$, but are about 10 μm in radius or larger. On the other hand, very small particle radii of smaller than 0.01 μm are assumed by Tsuji (2002) for opacity calculations. In Allard et al. (2001), a size distribution with radii between $6.25 \cdot 10^{-3}$ and 0.24 μm is set arbitrarily.
In the results, the maximum grain radii are of the order of $(1.0 \pm 0.5)\,\mu$m in the range from $T_{\rm eff} = 2600 \ldots 1500$ K with a small trend of increasing grain size at lower effective temperatures. In the range between $T_{\rm eff} = 2600$ and 3000 K, there is only very little dust which forms. At $T_{\rm eff} \approx 3000$ K and above, local temperatures are too high and number densities of TiO_2 are too low to allow for nucleation. Thus, these models are completely dust free.

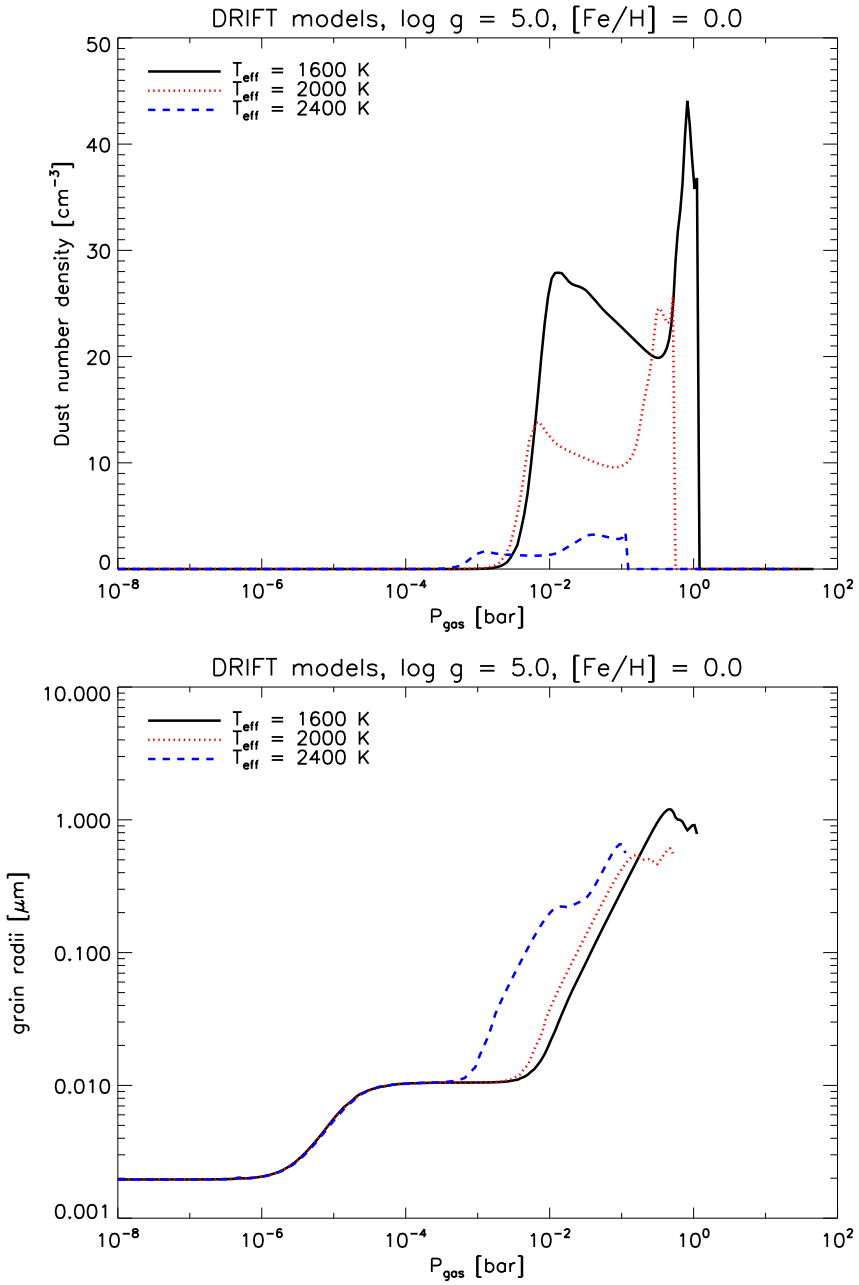

Figure 4.9: Dust number density n_d (top) and mean grain for radii <a> [μm] (bottom) for $T_{\rm eff} = 1600,\ 2000,$ and 2400 K, $\log g = 5.0$, and [Fe/H]$= 0.0$

4.2.2 Surface gravity

A variation of the surface gravity is interesting in order to explain the scattering found in J-K colour index for different spectral types. Different surface gravities might influence the location and extend of dust clouds and therefore cause the scattering (Marley et al., 2002; Tsuji, 2002; Tsuji et al., 2004; Tsuji, 2005; Stephens & Leggett, 2004; Knapp et al., 2004).
Surface gravities of low mass stars and substellar objects may range from $\log g = 3.4$ for Jupiter and $\log g = 4.4$ for a main sequence (low mass) star up to $\log g = 5.5$ for a star at the hydrogen-burning limit (Chabrier & Baraffe, 2000). Thus, assuming $\log g = 5.0$ for late L- and early T-dwarfs is a reasonable choice. In order to investigate dust properties in a wide range of the surface gravity, models with $\log g = 4.0$ and $\log g = 6.0$ are calculated. Each model has an effective temperature of 2000 K and solar metallicity. The temperature structure is shown in Figure 4.10, where the influence of the surface gravity on the hydrostatic equation can be seen easily, as it shifts the temperature structure by one order of magnitude in pressure with decreasing gravity towards the outer layers. So, it can be expected and predicted that the dust clouds

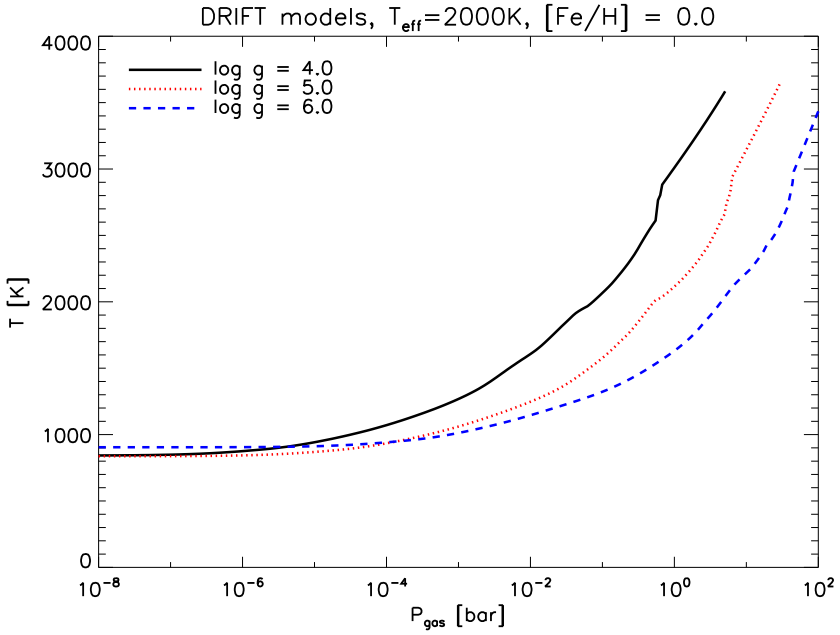

Figure 4.10: Temperature shape T [K] for $\log g = 4.0,\ 5.0,$ and 6.0, $T_{\rm eff} = 2000$ K, and [Fe/H]$= 0.0$

are located in upper regions of the atmosphere with lower surface gravity. Between 2000 and 3000 K, again, small dents in the temperature curves are seen. The right (inner) edge indicates the border of the convection zone, whereas the left (outer) one indicates a peak of the particle number density. The latter is shown in Figure 4.11 and it is indeed shifted in the atmosphere with changing surface gravity. In addition, the number densities differs significantly: The model with $\log g = 4.0$ has an maximum number density of one grain per cm^3, whereas the model with $\log g = 6.0$ exceeds 200

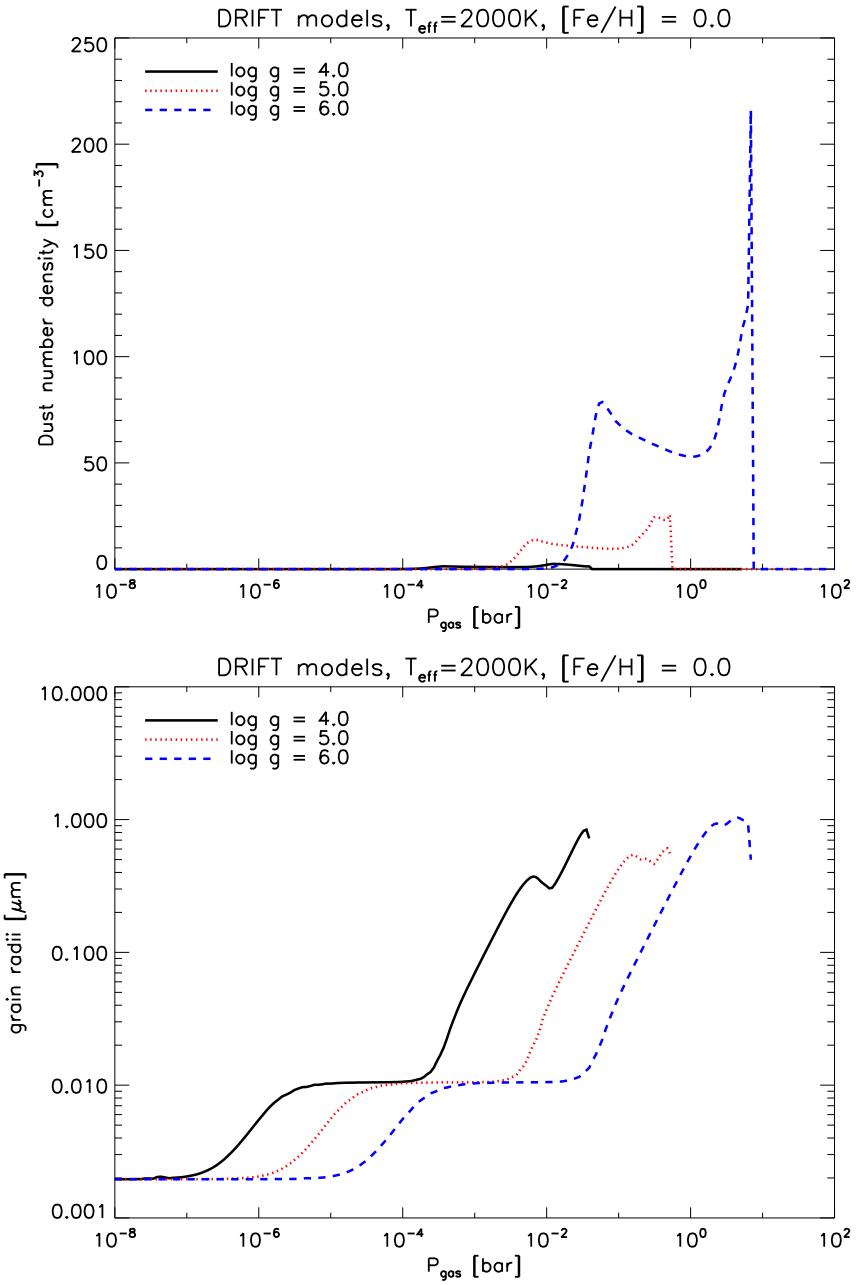

Figure 4.11: Number density of dust n_d [cm^{-3}] (top) and mean grain size $<a>$ [μm] (bottom) for $\log g = 4.0,\ 5.0,$ and 6.0, $T_{\rm eff} = 2000$ K, and [Fe/H]$= 0.0$

grains per cm^3. What is the reason of this large difference? The nucleation rate shows ratios of four orders of magnitude, in this case $J^{*\rm max}_{\log g=4.0}/J^{*\rm max}_{\log g=6.0} \approx 10^{-4}$ and their maxima are found at $P_{\rm gas} = 2.8 \cdot 10^{-4}$ and $4.5 \cdot 10^{-2}$ bar respectively. The large ratio might be explained as (in 0th order) $J^* \propto n^2_{\rm TiO_2} \propto \rho^2 \propto P^2_{\rm gas}$. The temperature at these two locations in the atmosphere differ by less than 100 K and, therefore, have no

big influence on the nucleation rate.[1] Thus, the much smaller gas pressure, and hence the smaller density, mainly influence the nucleation rate.
Figure 4.11 suggests that the total number of grains integrated along the line of sight ($\int n_d(z)dz$, column density) differs. It has to be stressed, that this representation is misleading: If n_d is plotted against z, the integrals remain nearly constant for different $\log g$ as the geometrical depth scales differently than $P_{\rm gas}$! Thus, with higher surface gravity dust particles concentrate on a small region at a depth of 3.8 km ($\log g = 6.0$, $n_d > 10^{-2}\mathrm{cm}^{-3}$) instead of 299.0 km ($\log g = 4.0$, $n_d > 10^{-2}\mathrm{cm}^{-3}$).
The mean grain size on the other hand, does not change. Despite the different gas pressure, which simply shifts the curves, the sizes can be considered equal on large ranges. Only some deviations are visible in inner atmosphere layers.

[1] Estimations of the dependency of J^* on particle density and temperature are seen in more detail in the appendix on page 75

4.2.3 Metallicity

Metallicity determines the amount of dust formed and may influence the sequence of condensation (Knapp et al., 2004; Kirkpatrick, 2005). If less metals (such as Al, Fe, Mg, Si, Ti) are available, less solids are expected to form.
Brown dwarf models with $T_{\rm eff} = 2000$ K with reduced metallicity by 0.5 and 1.0 dex are calculated. The results are compared with models with solar metallicity. The temperature structures are shown in Figure 4.12, whose scale in gas pressure is shifted, similar as in Figure 4.10 (changed surface gravity). Here, the surface gravity remains constant and does not change the hydrostatic structure, but the gas density and with it the molecular mass μ can. Differences in μ differ only by about 2.5 % and are therefore not the major reason for the shift.
Metal bearing molecules are depleted and their opacities are reduced. This makes the radiative cooling mechanism more effective and allows a deeper view insight the atmosphere at higher gas pressures (Chabrier & Baraffe, 2000, pg. 359). An optical depth of 100 (at $\lambda = 1.2\,\mu$m) is reached at $P_{\rm gas} = 31$ bar in a model with solar metallicity, but in a model with [Fe/H] $= -1.0$, the same optical depth is reached at $P_{\rm gas} = 108$ bar. As anticipated, the number of dust grains decreases with lower

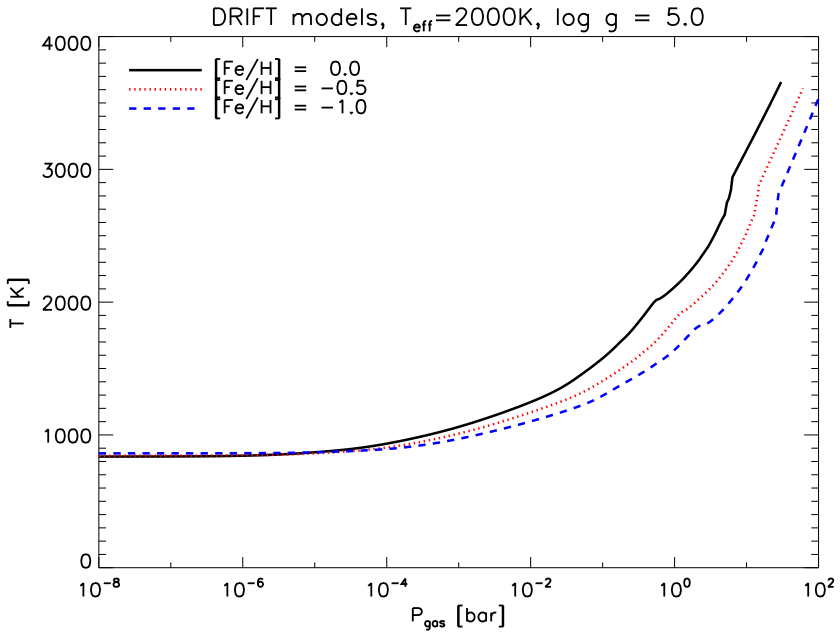

Figure 4.12: Temperature structures T [K] for [Fe/H] $= -1.0, -0.5,$ and 0.0, $T_{\rm eff} = 2000$ K, and $\log g = 5.0$

metallicities (Fig. 4.13), which is not only because of the depletion of heavy elements, but also because of a decrease of the convection speed $v_{\rm conv}$ of by 45%.This decrease in $v_{\rm conv}$ leads to a less efficient mixing in the outer parts of the atmosphere, which makes the few heavy elements even more rare. As very rough estimate, the maximum dust number density decreases by a factor of two for each decrease of 0.5 dex in metallicity. Because of the shift of the temperature density structure, the region of efficient grain

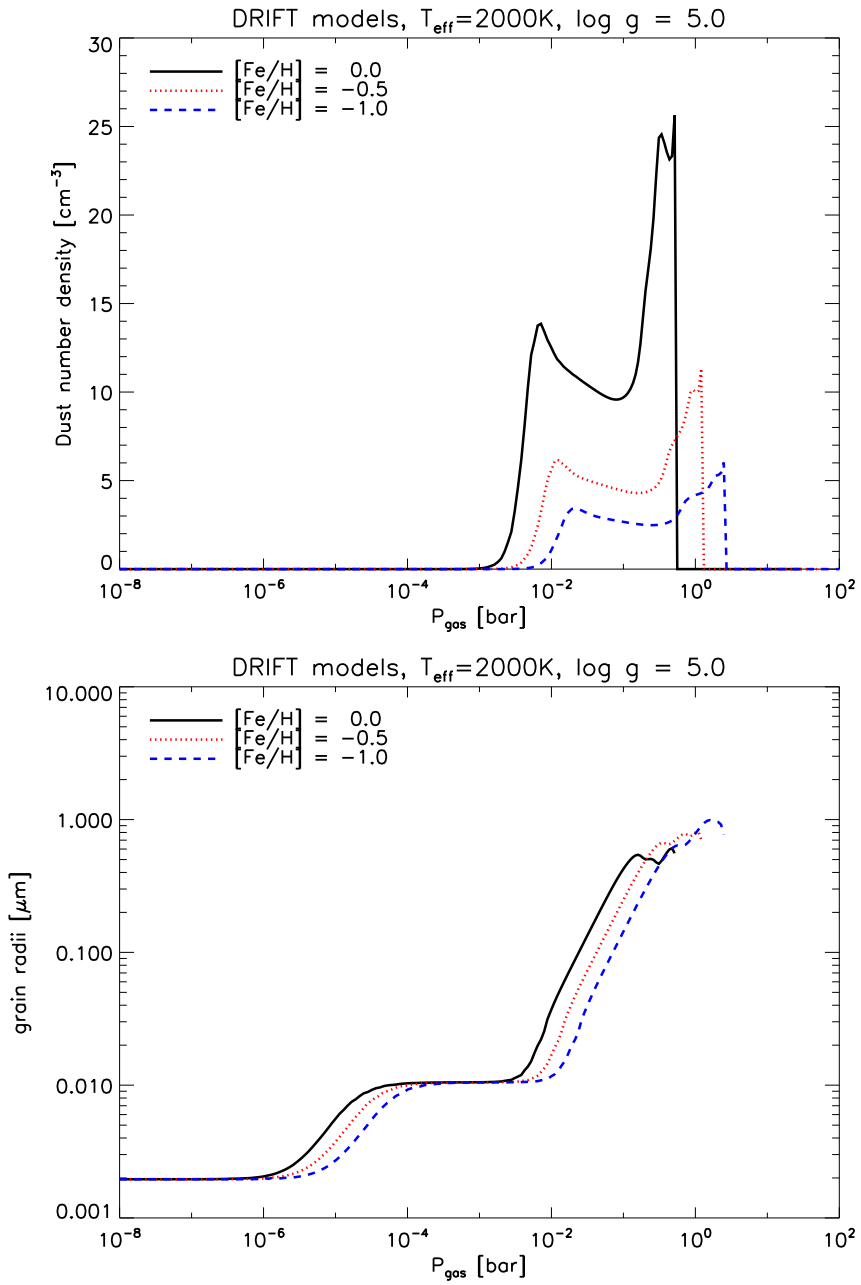

Figure 4.13: Number density n_d [cm^{-3}] (top) and mean grain size $<a>$ [μm] (bottom) for [Fe/H]$= -1.0, -0.5,$ and 0.0, $T_{\rm eff} = 2000$ K, and $\log g = 5.0$

growth ($\chi_{\rm net} > 0$) starts at higher pressures ($P_{\rm gas} = 5.1 \times 10^{-5}$ and 0.3 bar, compared to $P_{\rm gas} = 1.5 \times 10^{-5}$ and 0.1 bar at solar abundances) and is less efficient for lower metallicity. This leads first to smaller grain sizes. On the other hand, shortly before the evaporation zone begins, $\chi_{\rm net}$ increases with lower metallicities, producing 50% larger grain radii in these regions.

4.2.4 Convection and overshoot parameters

In this section, the mixing length parameter l/H_p and the gradient β of the extrapolated mass mixing time are examined.
The importance of the replenishment of elements by mixing is directly seen in the dust moment equation (2.1.22), given by the mixing time $\tau_{\rm mix}$ (Eq. 2.1.21). In the current implementation, $\tau_{\rm mix}^{\rm min}$ is given by the convection speed at the outer edge of the convection zone ($\tau_{\rm mix}^{\rm min} = l/v_{\rm conv}$, with mixing length l).
The mixing length parameter may range from 1.5 to 3.5, depending on the type of hydrodynamic treatment of the convection (Ludwig et al., 2002). In present models, a value of $l/H_p = 2.0$ is assumed. In order to check the influence on the atmospheric structure, it was changed to 1.0 and 4.0, two extreme limits, and compared to a model with $T_{\rm eff} = 2300$ K and $l/H_p = 2.0$. Results of the three models are shown in Figure

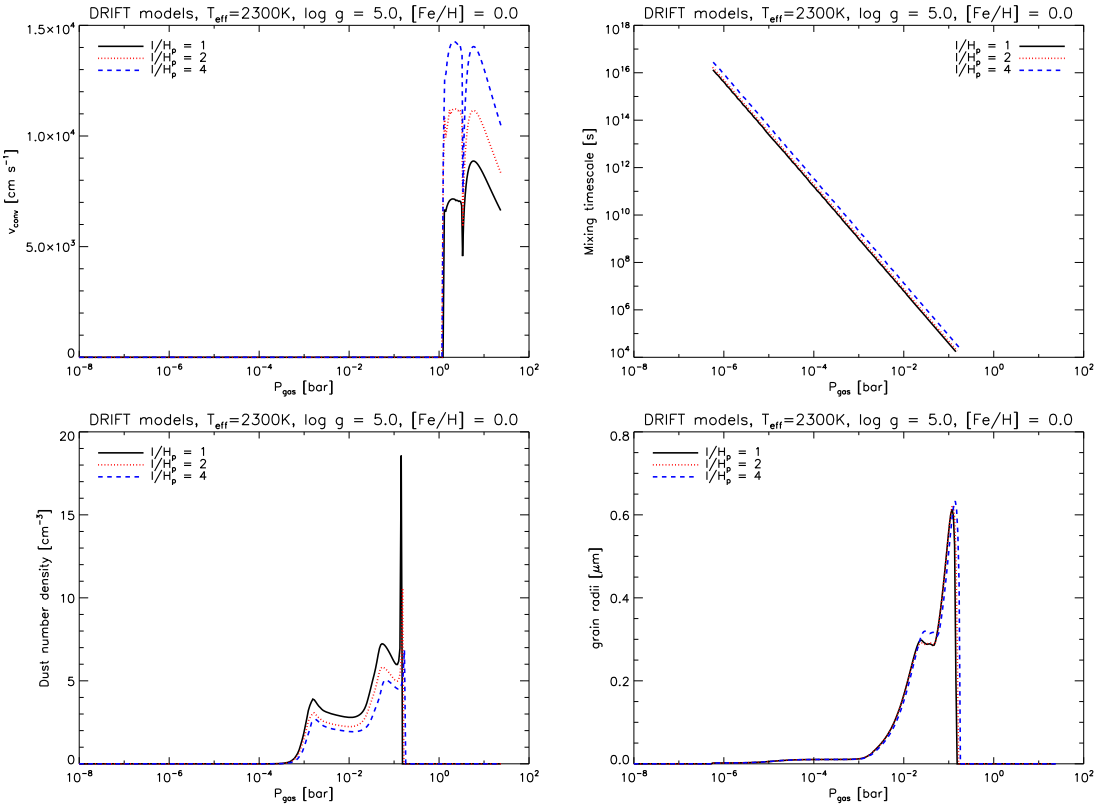

Figure 4.14: Influence of the mixing lengths on dust formation for $T_{\rm eff} = 2300$ K. Convection speeds obtained with $l/H_p = 1$, 2 and 4, its corresponding mixing time scale $\tau_{\rm mix}$ is shown in the upper panel. In the lower panel, dust number densities and mean grain radii are presented. Deviations of dust number densities related to $n_d(l/H_p = 2)$ drop below 20%.

4.14. The left picture on the upper panel simply shows the change of the convection speed $v_{\rm conv}$, which is strongly influenced by the mixing length. The change of $v_{\rm conv}$ is reflected in a corresponding change of the layer dependent $\tau_{\rm mix}$, which has the prescribed

gradient $\log \Delta\tau_{\rm mix}/\log \Delta P = \beta = 2.2$ (right figure). On the lower panel, the number density of dust (left) and their mean grain radii are plotted (right). Again, due to similar growth speed, the grain sizes remain similar. This is not true for the nucleation rate J^*. Because of a different efficiency in the mixing, J^* differs by about 20 % resulting in changes in n_d in the same order of magnitude.

The gradient of the mixing time β had been changed by about $\pm 10\%$ which corresponds

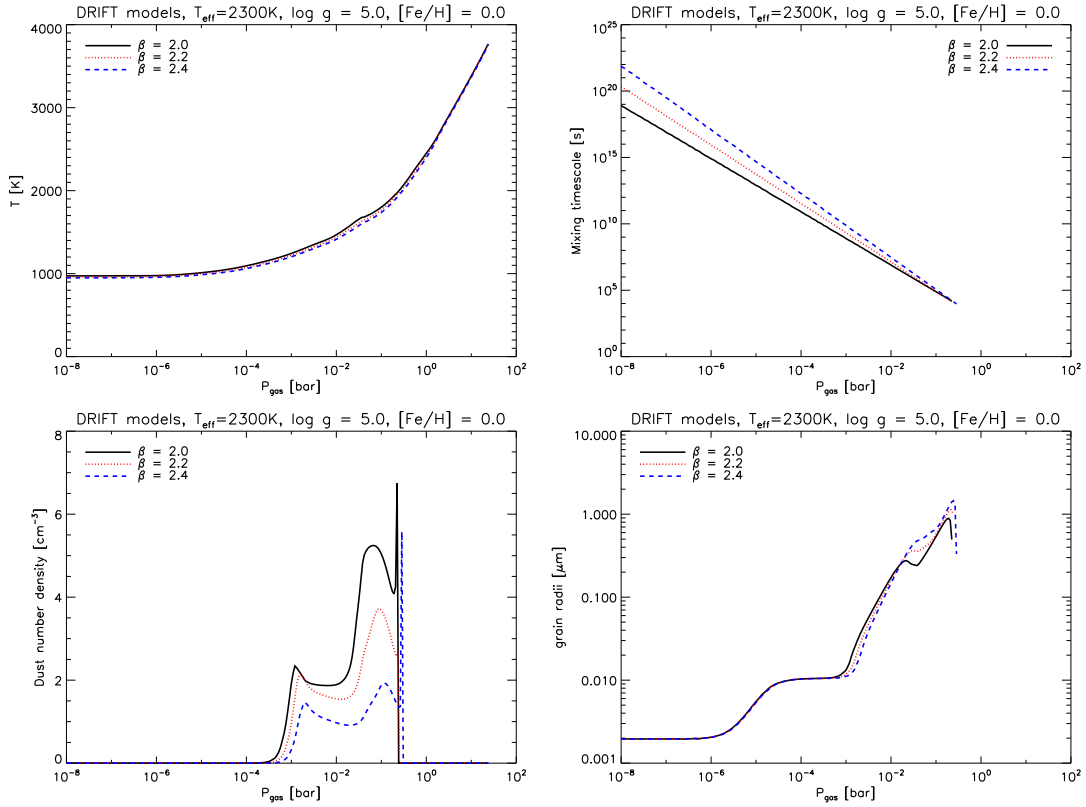

Figure 4.15: Influence of different gradients β in determining the mixing time scale $\tau_{\rm mix}$ on dust formation is shown on a model with $T_{\rm eff} = 2300$ K. Temperature structure of models with different $\beta = 2.0$, 2.2 and 2.4 is shown in the top left picture. Corresponding mixing time scale $\tau_{\rm mix}$ is on the right picture. In the lower panel, dust number densities and mean grain radii are presented. Dust number densities related to $n_d(\beta = 2.2)$ differ by a factor of about 1.5.

with the given error by Ludwig et al. (2006). Figure 4.15 shows results of models with $T_{\rm eff} = 2300$ K, $\beta = 2.0$, 2.2, and 2.4. The temperature structures of all the models are quite similar (left figure, upper panel) and the mixing time reflects the adjusted behaviour (right figure). For the higher mixing times, less "fresh" elements are available for dust formation, which is seen in the lower panel. The dust number densities differ by a factor of about three between the two extremes $\beta = 2.0$ and 2.4. The maximal mean grain radii are $<a>= 0.9\,\mu$m ($\beta = 2.0$) and $1.5\,\mu$m ($\beta = 2.4$) respectively . The differences may be caused by the changes in the different temperature structures, which are, in turn, caused by the different dust number densities.

It is clear that small changes in β have a big influence on the amount of dust formed, which makes the determination of this parameter an important issue. Bigger changes in β, e.g. by $\Delta\beta = \pm 1.1$, change the number dust density by more than one order of magnitude and strongly increase the effects of backwarming (see appendix A.3.1). Recent results suggest a value of $\beta = 2.4$ (Ludwig et al., 2006), which has to be considered consequently in future models.

4.3 Influence of minor model assumptions

4.3.1 Grain size distribution

The used grain size distribution can only give an impression of the width of the real physical distribution. Two grain sizes a_1 and a_2 are obtained, weighted with N_1/N and N_2/N, with $N = n_d$ (see section 2.1.5). In a model with $T_{\rm eff} = 1600$ K, the width $\Delta a = |a_1 - a_2|$ in the region of $P_{\rm gas} = 10^{-4} \ldots 10^{-2}$ bar is about $0.02\,\mu$m, which is seen in Figure 4.16. In other parts of the atmosphere, the distribution plays no role: This is true, if either Δa is too small or $|\log N_1 - \log N_2|$ larger than two. The latter means, that one distribution component is negligible ($< 1\%$) compared to the other. Results in other models give similar results, which leads to the conclusion, that the consideration of the grain size distribution in opacity calculations take only a very small effect, which is confirmed by appendant spectra: These models were compared with models which neglect the grain size distribution and only assume $n(a) = n_d \delta(a - <a>)$. They show similar spectra. Eventually, the modelling of the grain size distribution has to be revised. On the other hand, present results may be a reasonable representation of reality, because of the grain drift: Small grains have a slower drift velocity. Due to this, they have more time for growth reactions and all grain sizes may in the end equal.

4.3.2 Optical data

For each of the considered seven dust species, wavelength dependent refractive indices are available. In a more simple process the optical properties may be assumed to be the "astrophysical silicate", for which optical data are given in Draine (1985). Figure 4.17 shows synthetic spectra of two corresponding models ($T_{\rm eff} = 2000$ K, $\log g = 5.0$). If just "astrophysical silicate" is assumed larger fluxes in H, K, and L-band ($3.5\,\mu$m) emerge than in models, which calculate generic optical properties. On the other hand, fluxes in J-band are slightly decreased. 2MASS Colour indices $J - K$ are 0.98 ("generic") and 1.17 ("astr. silicate") respectively.

4.3.3 Effective Medium Theory

In this section, it is described how models behave, if no EMT is applied. Instead, only a simple averaging of the complex refractive indices of the dust components was performed in order to construct the refractive index of the compound grain. Comparison

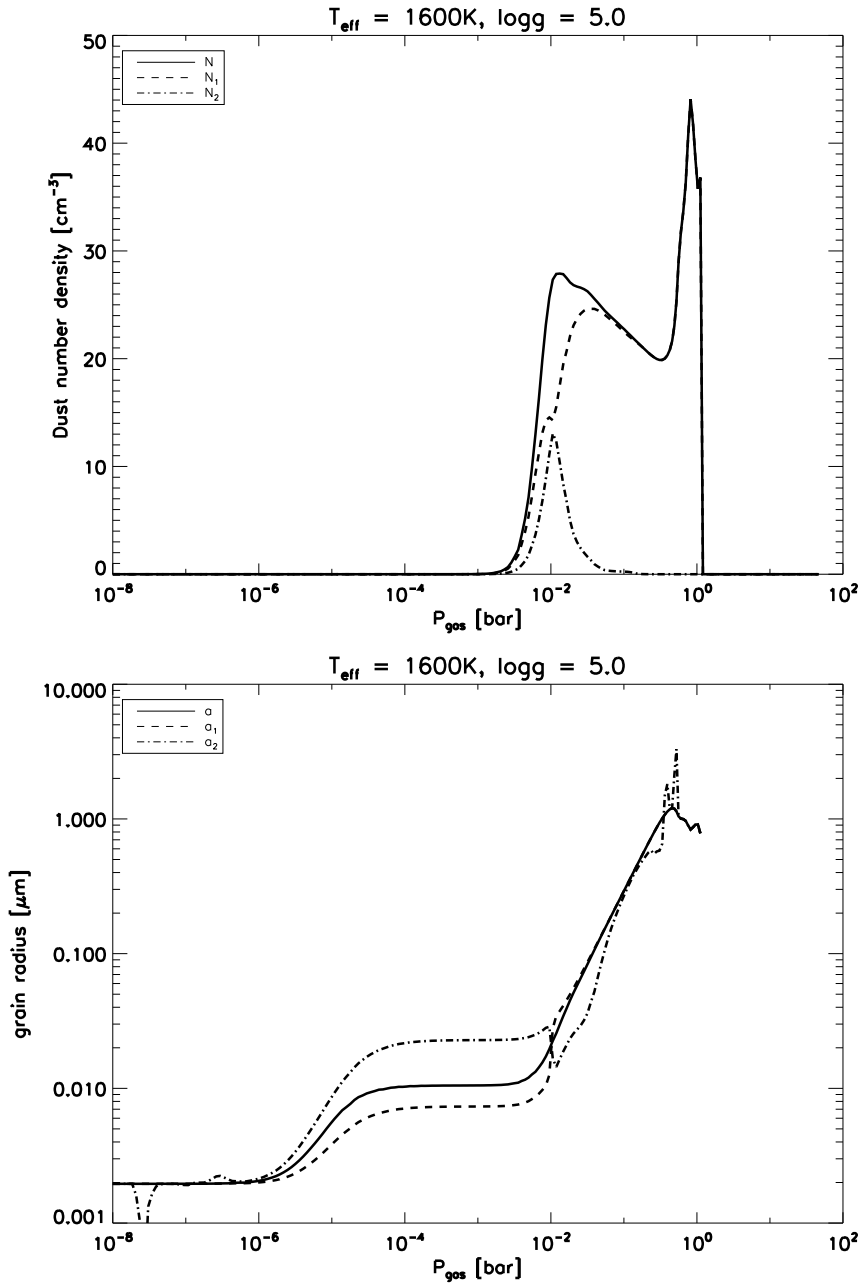

Figure 4.16: Solution of the two-peaked grain size distribution of a model with $T_{\rm eff}$ = 1600 K, $\log g$ = 5.0, and solar metallicity. The relations $N = N_1 + N_2$ and $a = (N_1 a_1 + N_2 a_2)/N$ are valid.

of the spectra show no significant differences. The reason for this is unclear. EMT calculations result in refractive indices which may differ one order of magnitude from averaged indices in each layer of the atmosphere. These differences might counteract each other in subsequent layers and nearly cancel out. Finally, it can be concluded,

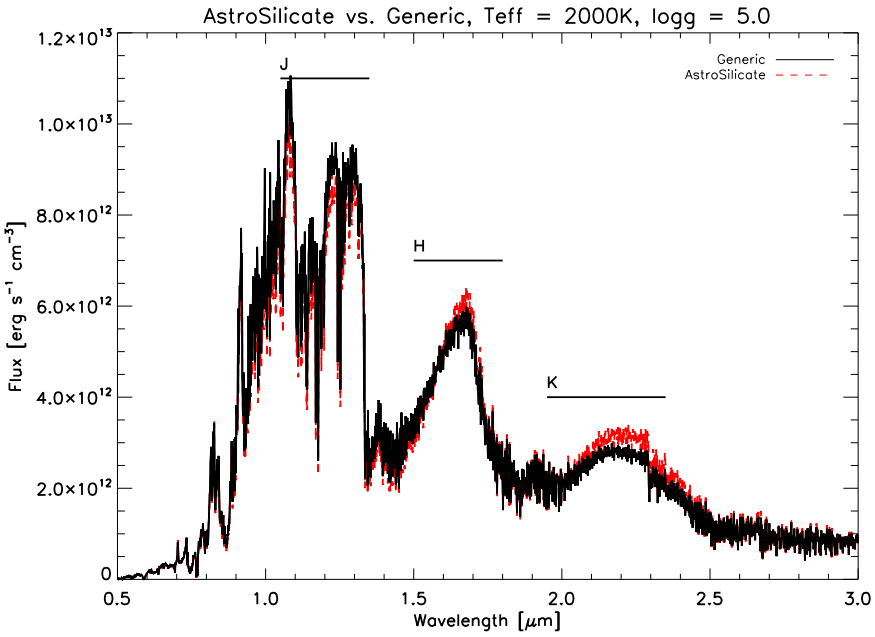

Figure 4.17: Synthetic spectra of two models with $T_{\rm eff} = 2000$ K, $\log g = 5.0$, and solar metallicity. In one model, composite grains are supposed to form (generic). In the other one, optical properties of the grains are supposed to be equal to "astrophysical silicates" (Draine, 1985)

Model		$\Delta(J-K)$
Size Distribution:	Single Sized	-0.02
Optical Data:	'Astr. Silicate'	$+0.15$
EMT:	Averaging only	$+0.02$

Table 4.2: Absolute changes in $J-K$, depending on model assumptions. The reference model with $T_{\rm eff} = 2000$ K, $\log g = 5.0$, solar metallicity and a $J-K$ index of (0.99 ± 0.01). For a detailed description of the different models, refer to the text.

that the consideration of grain size distribution and the application of effective medium theory seems to play only a minor role in the formation of the spectra. Table 4.2 shows relative changes in 2MASS $J-K$ colour index, if some assumptions are simplified. Consequently, maintenance of optical data from different databases and literature is more important and should be done regularly.

4.3.4 Radiative feedback

In this section, the influence of the input model on the dust structure is examined. Two different external atmosphere structures are passed to the dust routine. This means that no subsequent iterations with treatment of radiation transport, temperature correction, and adjustment of the atmosphere were performed. The dust properties are

compared to a fully iterated, self-consistent model. Figure 4.18 shows the atmospheric

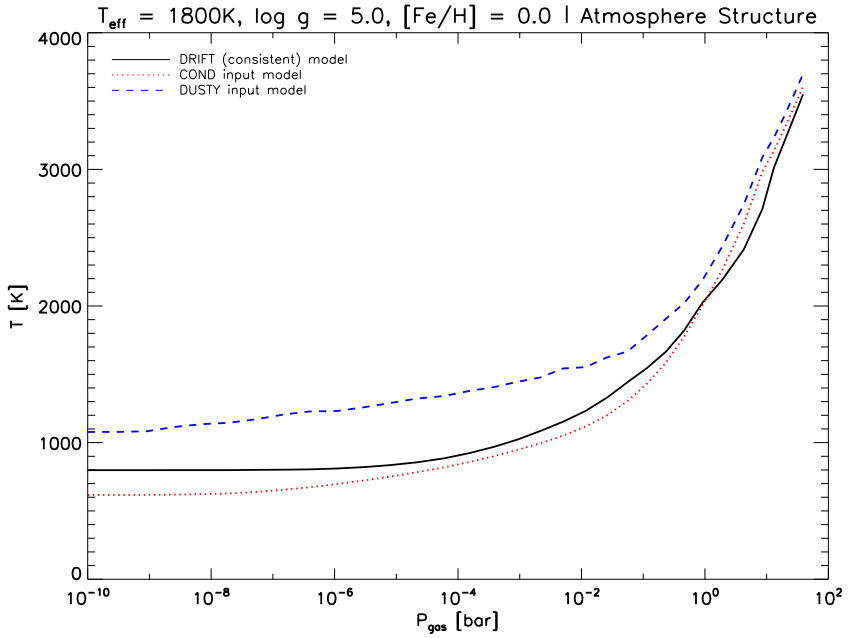

Figure 4.18: Different models (COND, DUSTY, DRIFT) with same model parameters: $T_{\rm eff} = 1800$ K, $\log g = 5.0$ and solar abundances (Grevesse et al., 1992).

structure of the different input models, whereas the model parameters are the same: $T_{\rm eff} = 1800$ K, $\log g = 5.0$ and solar abundances. The first external structure came from a fully iterated and converged COND model (see 1.2 and Allard et al. (2001)), which includes dust formation, but no dust opacity. The second external structure is based on a fully iterated and converged DUSTY model. In contrary to the COND model, the dust opacity plays an important role here as is the depletion of the gaseous elements. For comparison, the atmospheric structure of a DRIFT model is presented also. Mean grain radii and dust particle number densities after one iteration of the dust routine are shown in Figures 4.19 and 4.20. The two external input models produce totally different behaviours of the dust formation: The mean grain sizes are more than one order of magnitude higher ($\approx 4 - 20$ μm at maximum in the inner parts of the atmosphere) than those resulting of the self-consistent model, which hardly reaches 1 μm at maximum.
Dust particle numbers (n_d) change very much with different input models: With given COND model as input, the n_d reaches nearly 10^4 grains per cm^3. If a DUSTY model was used, n_d hardly exceeds 3×10^{-5} cm^{-3}. So, the results are similar to the results presented in Woitke & Helling (2004) where input models from Tsuji (2002) are used and no radiative feedback was taken into account, too. There, atmosphere models with $T_{\rm eff} = 1000$, 1400, and 1800 K were used to process dust properties without calculating dust opacities, recalculating radiative transfer or adjusting the atmosphere. Mean grain radii became much larger ($<a>_{\rm max} > 10\,\mu$m) than in our self-consistent models.

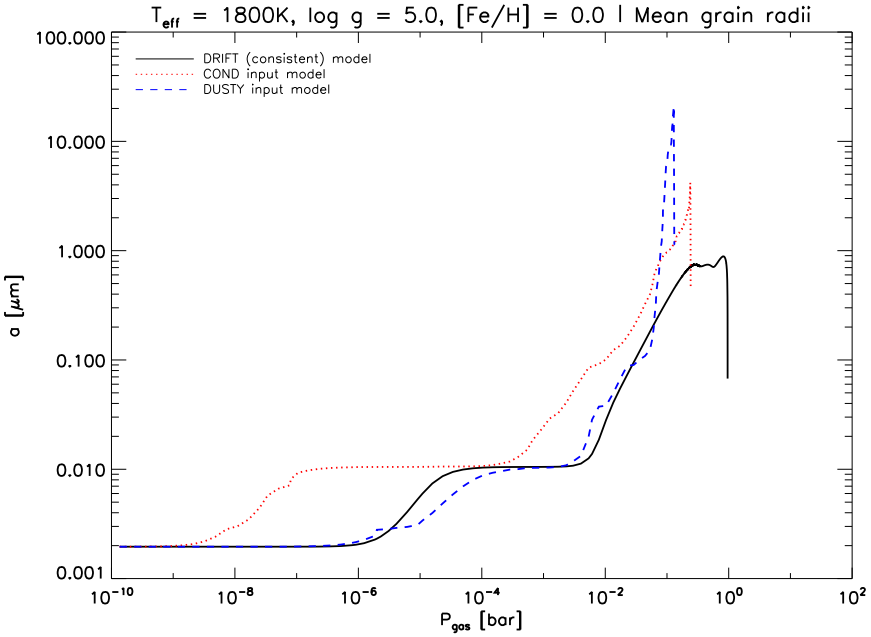

Figure 4.19: Mean grain radii $<a>$ [μm] with prescribed COND, DUSTY, and a consistent DRIFT atmosphere structure as input.

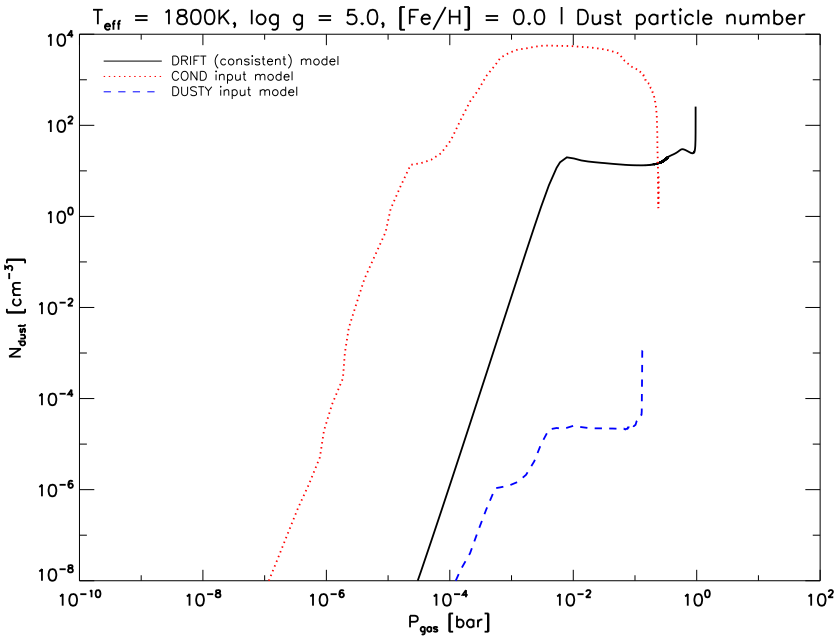

Figure 4.20: Dust number densities n_d [cm^{-3}] of dust with prescribed COND, DUSTY, and a consistent DRIFT atmosphere structure as input.

4.4 Dust opacities and synthetic spectra

4.4.1 Dust opacities

The grain composition does not change significantly for differing effective temperatures at the same local pressures. Large layer dependent variations do occur (see Figure 4.6 on page 35), and the general picture remains nearly constant. Thus, spectral features are expected to remain similar for changing T_{eff} apart from a systematic shift in wavelength. This shift is caused by the dependency of Mie theory on the size parameter $x = 2\pi a/\lambda$ (see section 2.2.3). Because mean grain radii $<a>$ change with T_{eff}, a feature at the same wavelength is expected to be shifted by the ratio $<a>\ (T_{\text{eff}} = A)/\ <a>\ (T_{\text{eff}} = B)$.

In the following Figures, the layer and wavelength dependent extiction coefficients χ_λ of three models are shown. The dust properties of the models are described in section 4.2.1; their effective temperatures are 1600 K , 2000 K, and 2400 K (Fig. 4.21).
The dust of the 1600 K model produces approximately grey opacities in the near infrared, except for a rise in χ_λ at $2.5\,\mu$m. Significant opacity is located only in the range $P_{\text{gas}} = 0.1$ to 1 bar. This corresponds to the largest amount of n_d (see Figure 4.2), because of the relation $\chi_\lambda \propto n_d$.
On the other hand, the dust opacities of the 2000 K model do show significant features, e.g. at 1.5, 1.7, and $2.0\,\mu$m. The maximum mean grain sizes differ by a factor of about 2, so the small feature at $2.5\,\mu$m in the 1600 K model should be visible at $1.25\,\mu$m in the model with $T_{\text{eff}} = 2000$ K. Hence, it might identical to the peak at $1.5\,\mu$m.
As shown above, models with $T_{\text{eff}} = 2000$ and 2400 K have nearly the same maximal mean grain size and, therefore, similarities in the opacities are expected. Comparison of the middle and bottom Figure (4.21) confirms this: The shapes of the plotted surfaces are similar, except for two additional peaks in the 2400 K opacities.
It has to be pointed out that comparisons at longer wavelengths (e.g. $2 - 16\,\mu$m) are much more difficult, because there are many bumps. For a better presentation, the opacity is integrated over the radius, which yields the optical depth τ.
First, the optical depths in the near infrared (NIR) are shown (fig. 4.22). The left figure shows $\tau(\lambda)$. The dust clouds of the models with $T_{\text{eff}} = 2000$ and 2400 K are optically thin ($\bar{\tau} < 0.5$) in the NIR, and the cloud for $T_{\text{eff}} = 1600$ K is optically thick ($\bar{\tau} \approx 1.9$). Optical depths are rescaled (right figure) in order to identify possible spectral features. Only the cloud in the warm model ($T_{\text{eff}} = 2400$ K) shows some features. However, they will not be visible in the spectrum, because they are too weak.

Optical depths in the mid-infrared (MIR, $2 - 16\,\mu$m) are shown in Figure 4.23. All clouds have in common that their optical depths (and their opacities) decrease by a factor of 4 or more between 2 and $16\,\mu$m. Even for $T_{\text{eff}} = 1600$ K, the cloud is optical thin at $\lambda > 12\,\mu$m. Some features up to $5\,\mu$m are seen, but they cannot be identified in the emergent spectra, because molecular bands are still too strong.

It was shown, that opacities significant where n_d exceeds a distinct amount, which complies with the definition of the cloud deck and cloud base. Concerning optical depth, no possible spectral features can be identified so far.

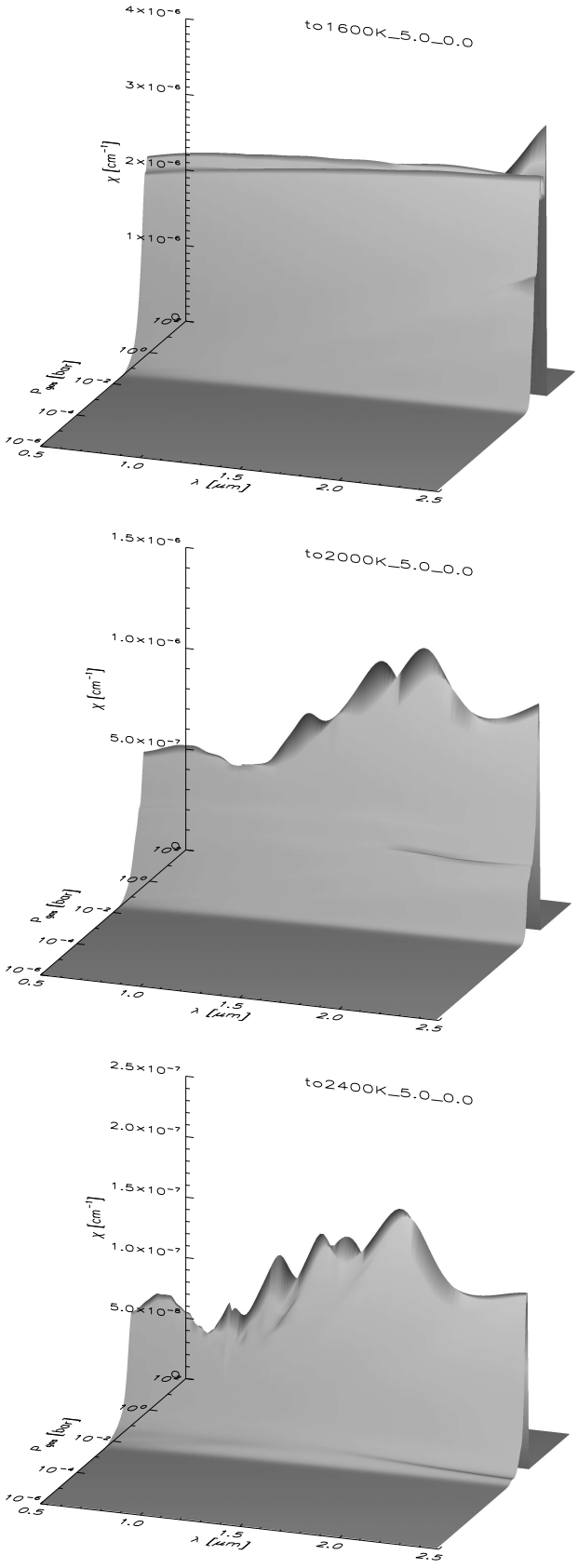

Figure 4.21: Extinction coefficient of dust $\chi(\lambda, P_{\rm gas})$ [cm^{-1}] of a model with $T_{\rm eff} = 1600$, (top) 2000, and 2400 K (bottom), $\log g = 5.0$, solar metallicity and its dependency of gas pressure and wavelength ($0.5 - 2.5\,\mu$m).

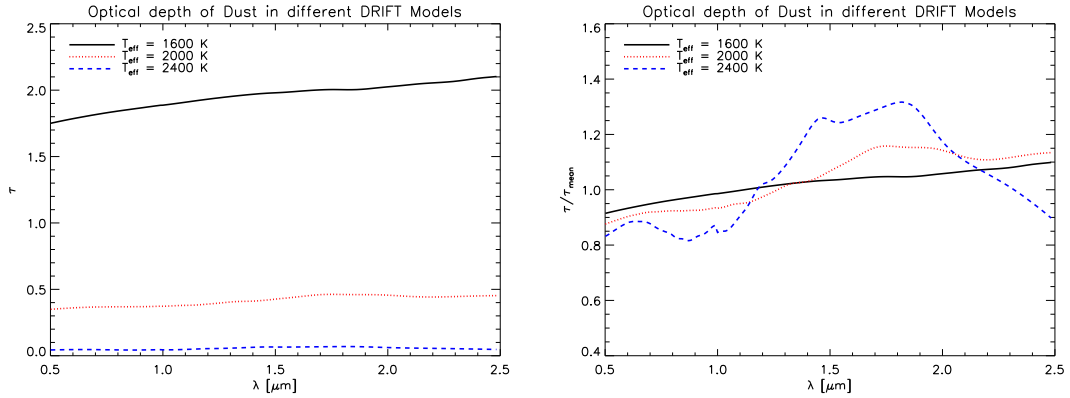

Figure 4.22: Near infrared, wavelength dependent optical depth τ of clouds for models with $T_{\rm eff}$ = 1600, 2000, 2400 K, $\log g$ = 5.0, and solar metallicity (left). In order to resolve features, optical depth is divided by its mean value in the corresponding wavelength range (right).

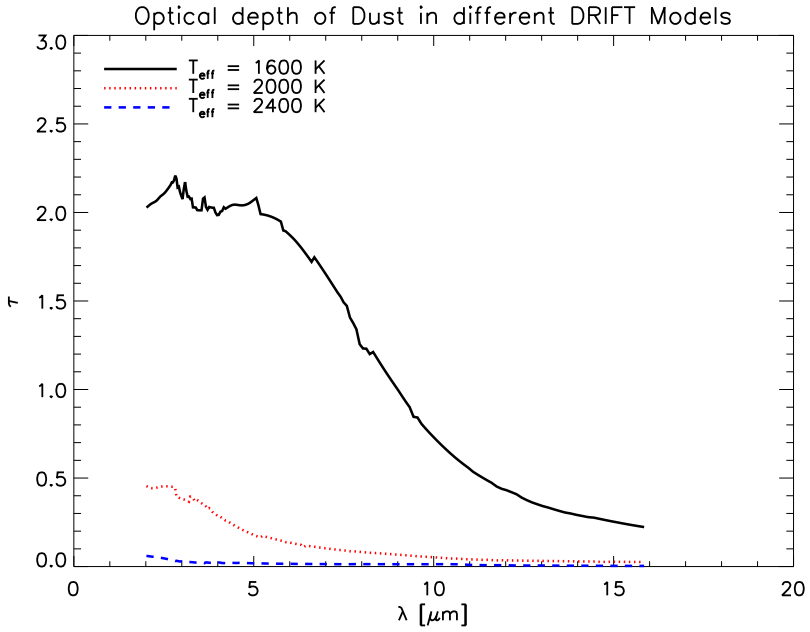

Figure 4.23: Mid infrared, wavelength dependent optical depth τ of clouds for models with $T_{\rm eff}$ = 1600, 2000, 2400 K, $\log g$ = 5.0, and solar metallicity.

4.4.2 Optical depth and cloud structure

Objects with low effective temperatures form more dust grains, which leads to optically thicker clouds. As seen in the previous section, models with $T_{\rm eff} = 2000$ K still produce optically thin clouds. Figure 4.24 shows the local gas pressures at the boundaries of the cloud structures, defined in section 4.1.6 (red lines). In addition, the local pressure of optical depth unitiy of the Rosseland depth $\tau_{\rm ross}$ is indicated (solid black line). Clouds become optically thick for $T_{\rm eff} < 2000$ K, where $P_{\rm gas}(\tau_{\rm ross} = 1) < P_{\rm gas}$(cloud base). Atmospheres with different stellar parameters show a similar behaviour: Optically thick clouds occur at $T_{\rm eff} < 1800 \ldots 2000$ K, nearly independent of $\log g$ and [Fe/H]. This means, spectral comparisons with other dust models are rather useful at these effective temperatures.

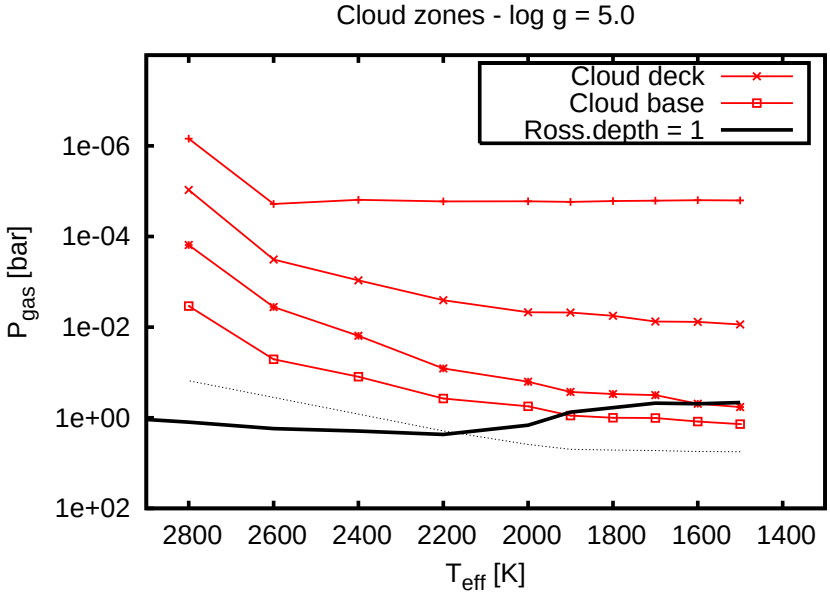

Figure 4.24: Cloud structure of models with $\log g = 5.0$, [Fe/H]$= 0.0$ and $T_{\rm eff} = 2800 \ldots 1500$ K. Local gas pressures of the fine particle zone (+), the cloud deck ($\times$), the rain edge ($\star$), and the cloud base ($\Box$) are shown for different $T_{\rm eff}$. The thick solid line indicates Rosseland depth of unity and the thin dotted line indicates the outer boundary of the convection zone. Clouds become optical thick for $T_{\rm eff} < 2000$ K.

4.4.3 Spectral properties in the near-IR

In this section, spectra of several DRIFT models are presented. The stellar parameters are the same as in section 4.2 in order to make comparisons with physical dust properties more easy.

Figure 4.25 displays smoothed spectra of models with $T_{\rm eff} = 1600$, 2000 and 2400 K. As seen before in section 4.4.1, the dust opacities increase with decreasing effective temperature. A strong suppression of fluxes in J, H, and K-bands is seen in the spectra. Molecular features are clearly seen, e.g. FeH at $0.98\,\mu$m, water bands at 1.4, 1.9, and

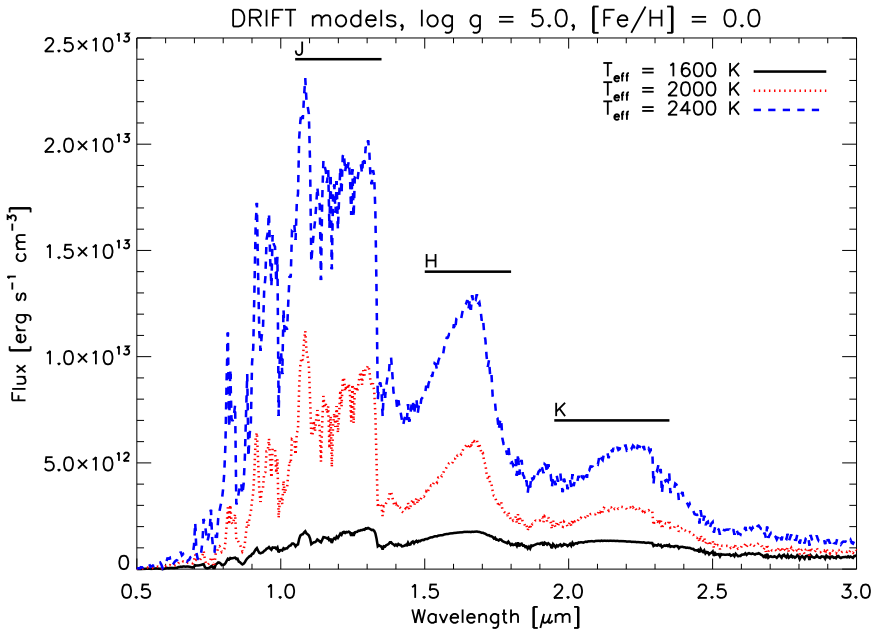

Figure 4.25: Near infrared spectra of models with $T_{\rm eff}$ = 1600, 2000 and 2400 K, $\log g = 5.0$ and [Fe/H]= 0.0.

2.6 μm, and a CO edge at 2.3 μm.

Spectral features also change with varying surface gravity, which is seen in Figure 4.26 for models with $T_{\rm eff} = 2000$ K. Models with high surface gravity ($\log g = 6.0$) produce more dust in thin layers ($\sim$ 4 km) in opposite to models with low surface gravities ($\log g = 4.0$) whose dust layers are thicker ($\sim$ 300 km). It is possible that either the dust opacities or water bands are located at different optical thick layers with varying $\log g$. This might smear out spectral peaks in the H- and K-band and shifts them by about 0.1 μm to the blue. This effect appears at 4.0 μm again, but cannot be seen at higher wavelengths. All these effects hardly change colour index $J - K$, which remains at about 1.01 ± 0.2. This is seen in table 4.3, which contains colour indices for changed $\log g$ and [Fe/H] in DRIFT models with $T_{\rm eff} = 2000$ K.

Changes in metallicity result in an increase of collision induced absorption of molecular hydrogen (CIA H_2) centered at $\lambda \approx 2.0\,\mu$m. This leads to a blue shift of the spectral energy distribution (Allard & Hauschildt, 1995; Chabrier & Baraffe, 2000) which is seen in Figure 4.27. This effect is much stronger than extinction by dust, because the flux in the H- and K-band is suppressed with decreasing metallicity, although much less dust is available.

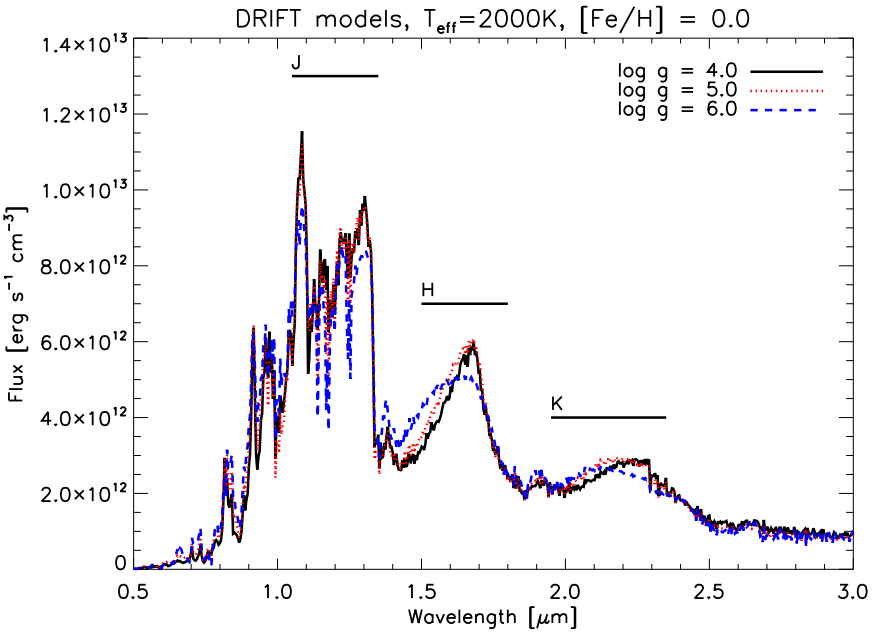

Figure 4.26: Near infrared spectra of models with $\log g = 4.0,\ 5.0,$ and 6.0, $T_{\rm eff} =$ 2000 K, and [Fe/H]= 0.0.

Model		$J-H$	$J-K$	$H-K$
$T_{\rm eff} = 2000$ K		0.547	0.998	0.451
$\log g =$	4.0	0.462	0.931	0.469
	6.0	0.611	1.023	0.412
[Fe/H] =	−1.00	0.256	0.532	0.276
	−0.50	0.467	0.801	0.335
	−0.25	0.551	0.958	0.407
	+0.25	0.583	1.084	0.501
	+0.50	0.636	1.200	0.564

Table 4.3: 2MASS $J-H$, $J-K$, and $H-K$ colour indices as function of different stellar parameters. If not explicitely given, stellar parameters are $T_{\rm eff} = 2000$ K, $\log g = 5.0$, and [Fe/H]= 0.0.

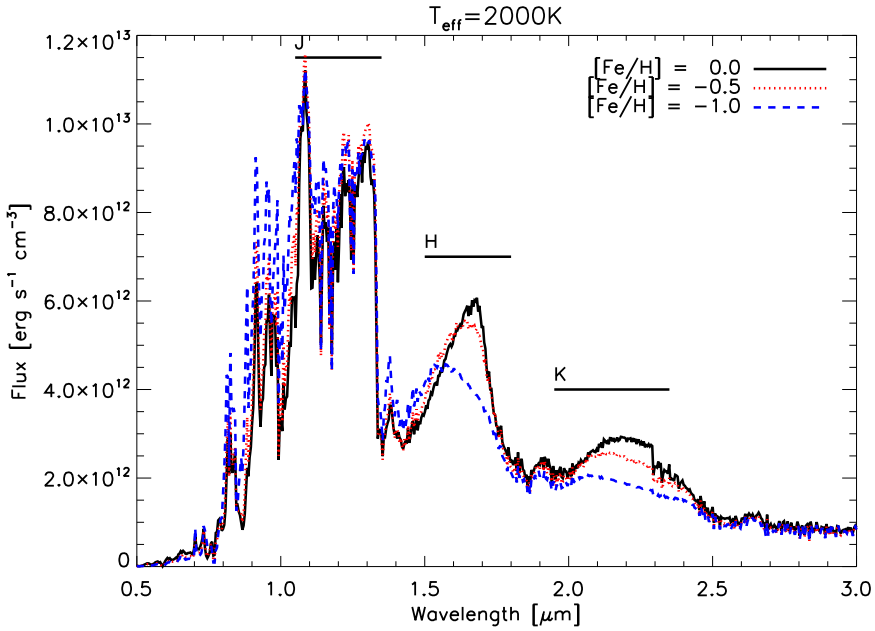

Figure 4.27: Near infrared spectra of models with [Fe/H]= 0.0, −0.5, and − 1.0, $T_{\rm eff} = 2000$ K, and $\log g = 5.0$.

4.5 Observing dust properties

It was shown in the last sections how dust number densities and grain sizes influence emergent spectra. On the other hand, it is useful to observe dust properties directly. In this section, the connection between $J-K$ colour indices and the integrated dust number density is shown. This integrated dust number density is defined by $N := \int n_d(z)dz$ [cm^{-2}] and is called *dust column density*. Here, the integration is limited to the line of sight inside the brown dwarfs atmosphere.

4.5.1 2MASS J-K colour indices

Figure 4.28 shows $J-K$ colour indices of DRIFT models with $T_{\rm eff} = 3000 \ldots 1400$ (indicated in blue, red, and magenta). COND and DUSTY models (cyan) with $\log g = 5.0$ and solar metallicity are also shown in order to demonstrate the limiting effects of completely settled or dusty atmospheres (Allard et al., 2001). $J-K$ of the DRIFT model[2] with $\log g = 5.0$ (blue) lie always between corresponding colour indices of the COND and DUSTY models ($(J-K)_{\rm COND} \leq (J-K)_{\rm DRIFT} \leq (J-K)_{\rm DUSTY}$, $\forall\, T_{\rm eff}$). At $T_{\rm eff} > 2600$ K, $J-K$ of all models with $\log g = 5.0$ are similar with $J-K \approx 0.8$, because there is essentially no dust in the atmosphere and the models do not differ except for the treatment of dust. $(J-K)_{\rm COND}$ drops down to about 0.2 at $T_{\rm eff} = 1500$ K and $(J-K)_{\rm DUSTY}$ exceeds 4.0 at $T_{\rm eff} = 1400$ K.
Differences in $J-K$ of DRIFT models with $\log g = 4.0$ and 6.0 (red) are about 0.4 at the same $T_{\rm eff}$. There is no systematic shift in the indices, so e.g. $(J-K)_{\log g=4.0} < (J-K)_{\log g=5.0}$ at $T_{\rm eff} = 1700 \ldots 2000$ K, but vice versa below 1600 K. A systematic shift is seen, when metallicites are changed from [Fe/H]= 0.0 to -1.0. The differences in colour indices are about $0.3 \ldots 0.5$, and $(J-K)_{\rm [Fe/H]=-1.0} \leq (J-K)_{\rm [Fe/H]=-0.5} \leq (J-K)_{\rm [Fe/H]=0.0}$ in all cases. The turn to the blue with smaller metallicities is mostly the result of the raising CIA H_2, described in the previous section.
A comparison of observed $J-K$ indices with other brown dwarf models is shown in Section 4.6.

[2]The DRIFT module and the PHOENIX code

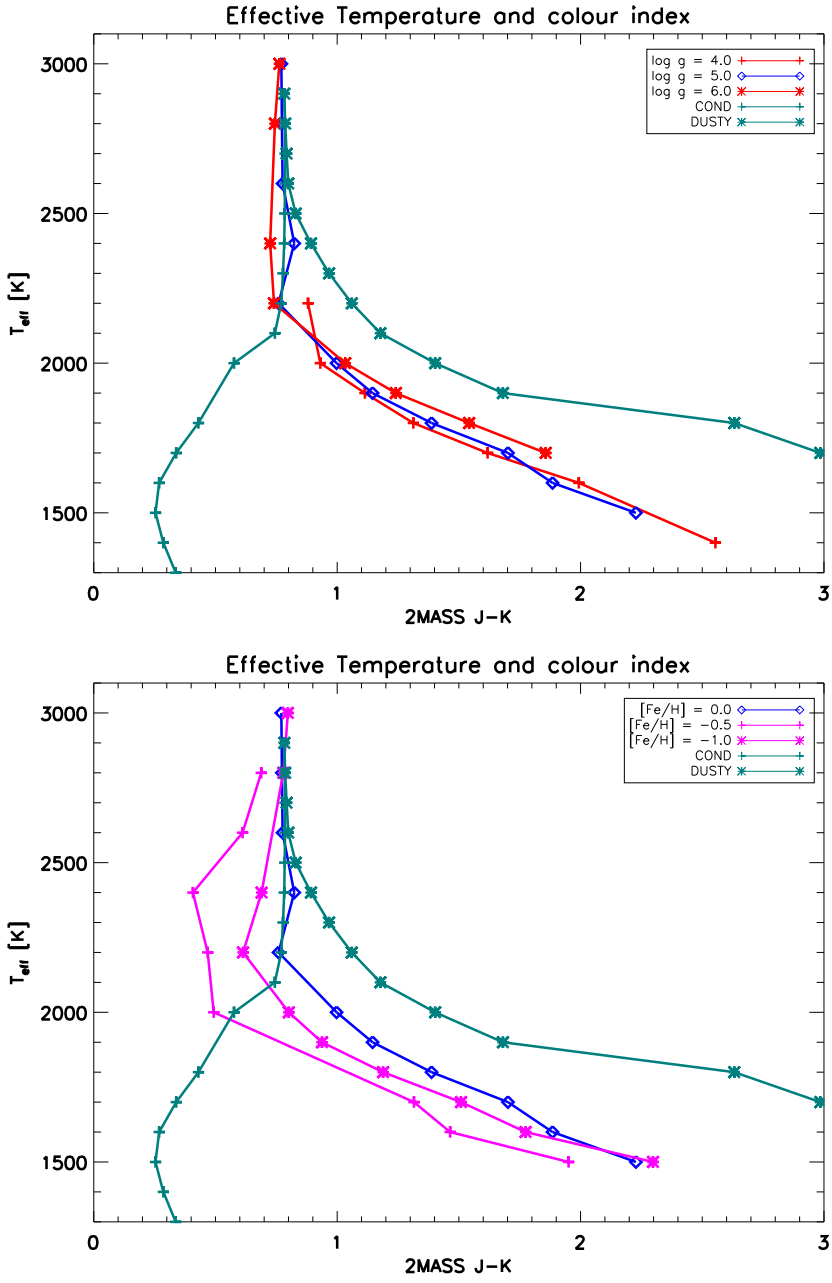

Figure 4.28: Colour indices $J - K$ (2MASS) of different dust models. Colour indices of DRIFT models with $\log g = 5.0$ (blue), $\log g = 4.0$ (red +), $\log g = 6.0$ (red $\star$), [Fe/H]$= -0.5$ (magenta +), and [Fe/H]$= -1.0$ (magenta $\star$) are shown. For comparison, COND (cyan +) and DUSTY models (cyan $\star$) with $\log g = 5.0$ and [Fe/H]$= 0.0$ are plotted.

4.5.2 Column densities

Until now, spectral features induced by dust grains cannot be identified in present models, so, other observable properties has to be used meanwhile.
Figure 4.29 shows column densities at different $T_{\rm eff}$ and their dependency of $\log g$ (top) and [Fe/H] (bottom). Differences of $\log g$ do not result in different column densities,

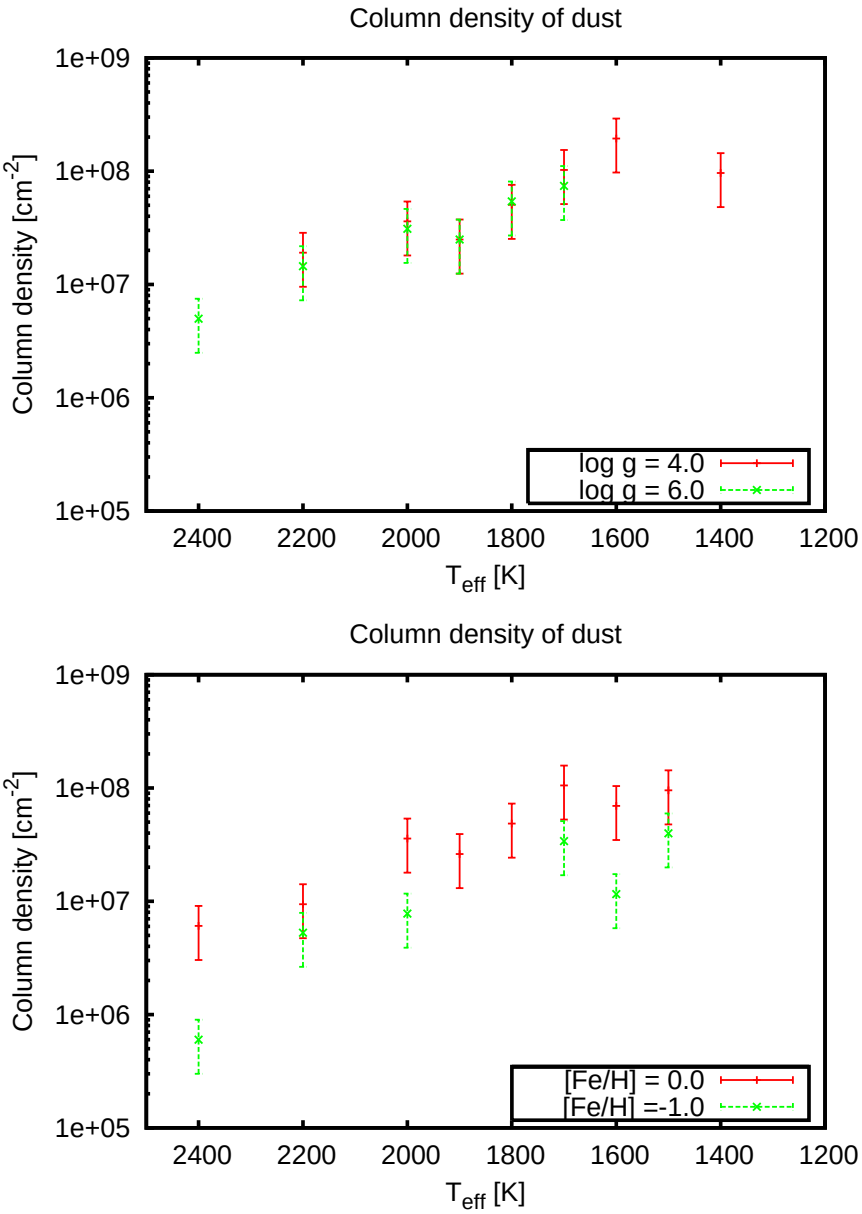

Figure 4.29: Dust column densities [cm^{-2}] vs. effective temperatures [K] of models with $\log g = 4.0$, 6.0 (top) and [Fe/H]$= 0.0, -1.0$ (bottom)

which was already mentioned in section 4.2.2. Reduced metallicities, on the other hand, reduce column densities, because of the lack of metals which are needed for dust

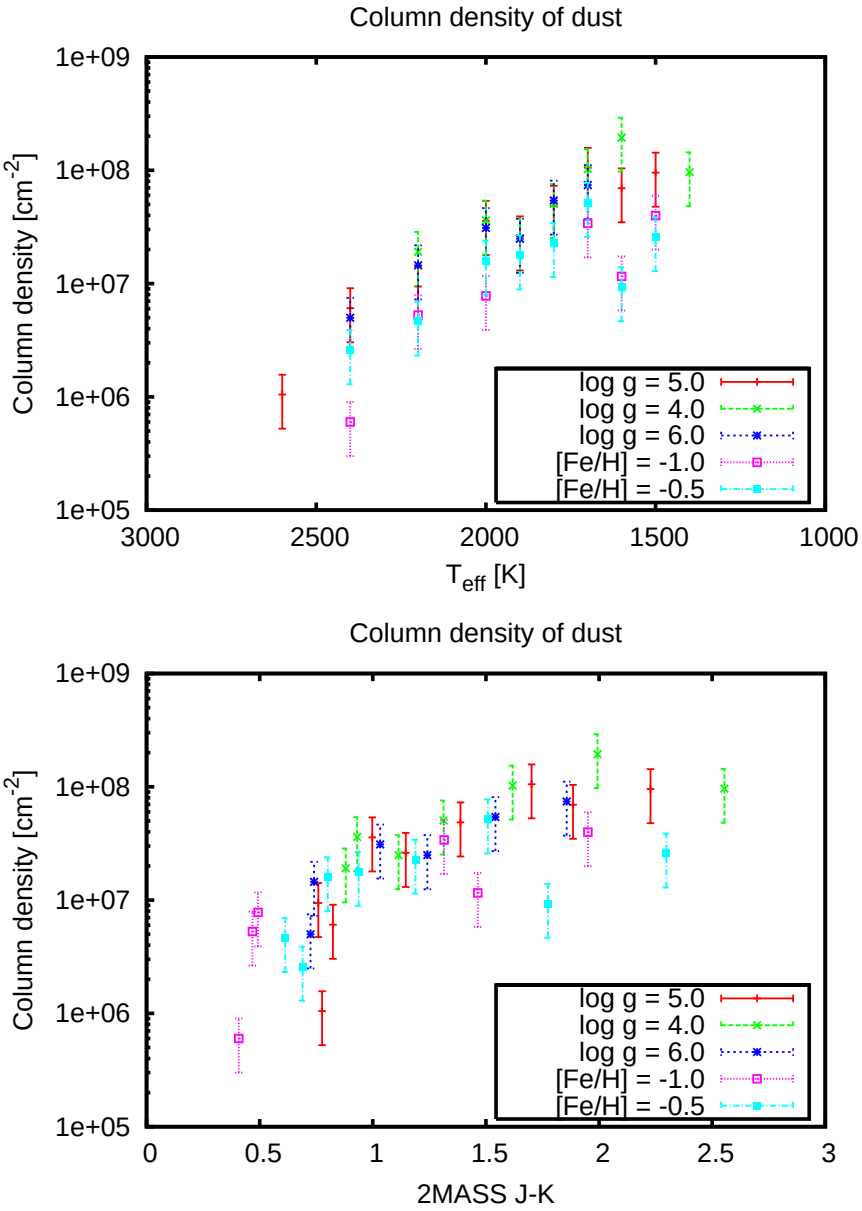

Figure 4.30: Column densities [cm^{-2}] dependent of effective temperature (top) or 2MASS $J-K$ (bottom).

formation (see section 4.2.3). The integrated amount of dust is very sensitive to small temperature changes of the atmosphere, so errors in N are estimated to about 50%. Column densities N of all calculated models are shown in Figure 4.30 as function of T_{eff} (left) and $J-K$ (right). For $T_{\mathrm{eff}} > 2600 \ldots 2800$ K, N drops to very low values and is not displayed. If N is shown as function of $J-K$, the systematic differences in N due to changed metallicities nearly disappear, despite that there is still a scattering of N of one order of magnitude. For $J-K > 1$, a rough estimate can be made with $\log_{10} N = (0.35 \pm 0.16)\,(J-K) + (7.07 \pm 0.27)$. For $J-K < 1$, the scatter of N is too

large, because models with no dust at all are also included in this sample.
This relation can only be used as a preliminary and rough estimate, which is only valid for L dwarfs for now. Once the dust model is able to reproduce the L-T transition, which is at $J - K < 1$ for T-dwarfs at lower effective temperatures, estimates which also use $J - H$ and $H - K$ indices may be considered. These indices can be used to roughly distinguish M, L, and T-dwarfs as shown e.g. in Knapp et al. (2004); Tsuji (2005); Burrows et al. (2006). For comparisons, it might be interesting how N depends on observable properties in other dust models.

4.6 Comparison with other models and observations

4.6.1 Dust properties of a SETTLING model

In recent brown dwarf model calculations with PHOENIX, the dust treatment by Allard et al. (2001) had been used. In this paper, two limiting cases of COND and DUSTY clouds had been introduced. A more recent development is the SETTLING model (Allard et al., 2003) which also treats the drift of formed dust. As all of these methods are already implemented in the PHOENIX code, it is worth to compare results of these models with results of this work. Due to the fact, that the main parts of the hydrostatic and radiation transfer consist of the same code and therefore, errors due to different assumptions in the physics of these parts are not present, a comparison concentrates on the dust treatment itself.
The results of two SETTLING models are shown below in order to indicate major differences in the structure of the resulting dust clouds. Figure 4.31 shows two main dust properties: Mean grain radii <a> and dust number density n_d against gas pressure in comparison to DRIFT models. It can be seen, that SETTLING clouds are three

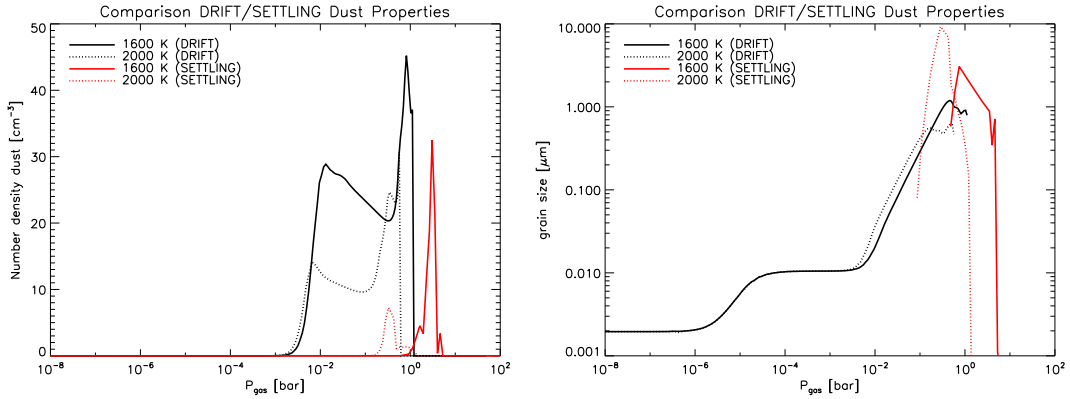

Figure 4.31: Dust particle numbers n_d [cm^{-3}] (left) and mean grain radii <a> [μm] (right) of two SETTLING models (red) with $T_{\rm eff}$ = 1600 and 2000 K and $\log g = 5.0$ compared to DRIFT models (black). Maximum grain radii in SETTLING dust clouds reach 3 and 10 μm instead of 0.6 and 1.2 μm.

orders of magnitude thinner in gas pressure than corresponding DRIFT clouds. The maximum number of the dust number density is also smaller: In DRIFT models n_d reads 45 ($T_{\rm eff}$ = 1600 K) and 25 grains per cm^3 ($T_{\rm eff}$ = 2000 K), compared to 32 and 8 grains per cm^3 in the SETTLING. Mean grain radii in SETTLING models are up to eight times larger than in corresponding DRIFT models.
DRIFT models contain much more dust, which is seen in the absolute synthetic spectra in Figure 4.32. Therefore, flux in J, H, and K-bands is much stronger suppressed, which leads to a higher flux at long wavelengths and in the water bands. The broad CH_4 feature at 8 μm is only seen in the SETTLING spectrum.

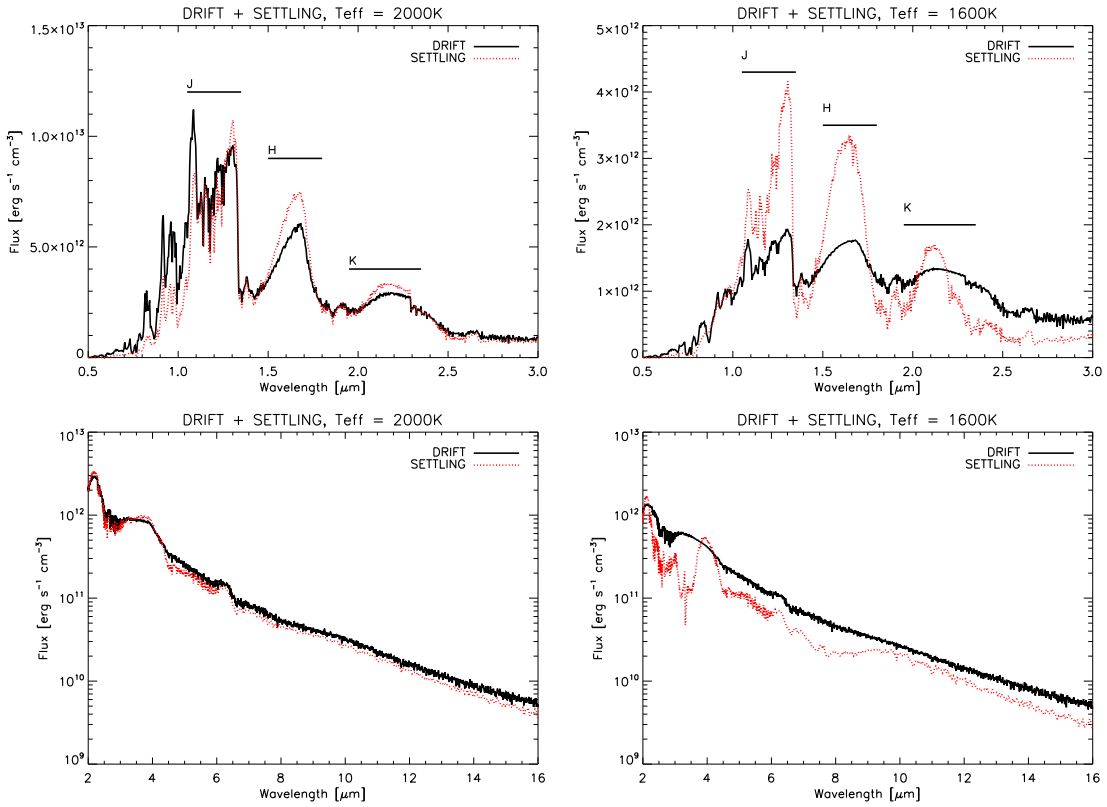

Figure 4.32: Emergent spectra of DRIFT(black) and SETTLINGmodels (red) with $T_{\rm eff} = 1600$ (right) and 2000 K (left), $\log g = 5.0$, and [Fe/H]= 0.0 in near (top panel) and mid infrared (bottom panel).

4.6.2 Spectral comparison with COND and DUSTY models

Spectral features of the different PHOENIX models with $T_{\rm eff} = 2400$ and 2000 K, $\log g = 5.0$, and solar composition are shown in Figure 4.33. Spectra for $T_{\rm eff} = 2400$ K are nearly identical, because the dust clouds are optically thin. At $T_{\rm eff} = 2000$ K, the first deviations appear: The COND model produces more flux in the J-band, because there is no dust present. Water bands are stronger than in corresponding DUSTY and DRIFT models. The DRIFT model suppress more flux in H-band than the COND and DUSTY models.

The differences in the models are obvious, if $T_{\rm eff}$ drops down to 1600 K. Figure 4.34 (left) shows very suppressed fluxes in J and K-bands of the DUSTY model, even stronger than the suppression seen in the DRIFT model. The flux in J-band is more than three times larger in the COND model. The suppressed radiation finds other ways to leave the atmosphere: The right figure shows the spectra in the mid infrared. It is seen, that the two dust rich atmospheres DRIFT and DUSTY emit much more flux in that spectral range. The CH_4 feature at 8 μm exists only in the COND model.

The $J - K$ diagram of all COND, DUSTY, SETTLING, and DRIFT models with $\log g = 5.0$ and [Fe/H]= 0.0 (Figure 4.35) makes clear that DRIFT models lie between

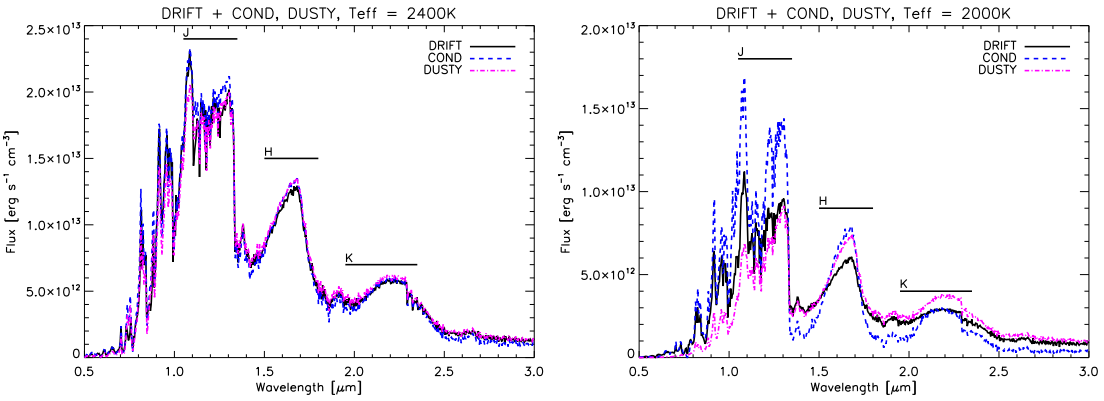

Figure 4.33: Comparison of DRIFT spectra (black) with COND (blue), and DUSTY models (magenta) with $T_{\rm eff} = 2400$ (left) and 2000 K (right). Major differences occur at $T_{\rm eff} = 2000$ K.

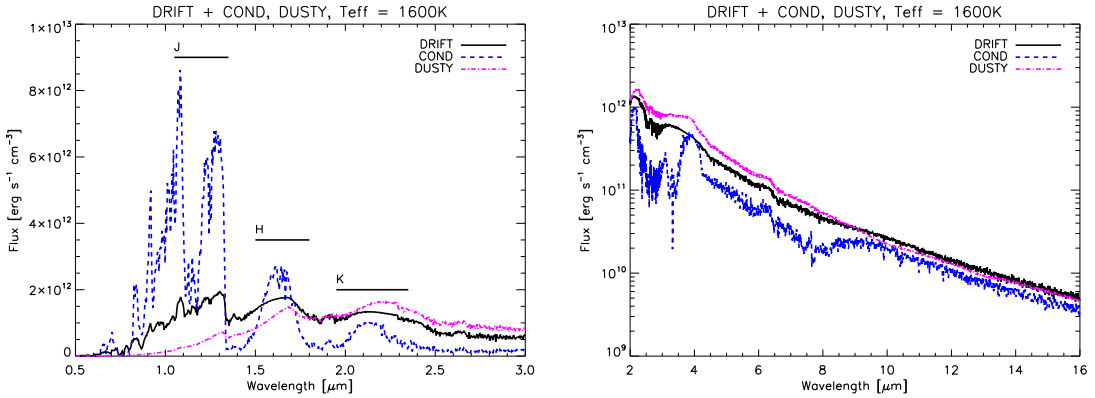

Figure 4.34: Comparison of DRIFT spectra (black) with COND (blue), and DUSTY models (magenta) with $T_{\rm eff} = 1600$ in the near (left) and mid infrared (right).

SETTLING and DUSTY(in terms of $J - K$), where dust clouds become optically thick ($T_{\rm eff} < 2000$ K). They also agree well with observations, which is seen in section 4.6.4.

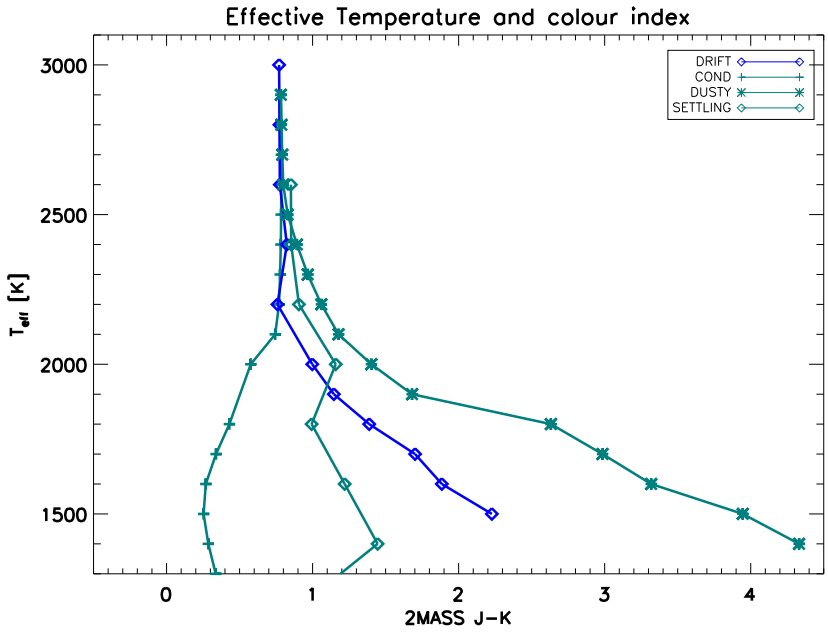

Figure 4.35: 2MASS $J - K$ colour indices of all PHOENIX models in the range of $T_{\rm eff} = 3000 \ldots 1300$ K. The limiting properties of COND (+) and DUSTY models ($\star$) are seen. SETTLING (cyan $\diamond$) and DRIFT models (blue $\diamond$) lie in between.

4.6.3 Modelling DENIS J0205-1159

All the comparisons made in the previous sections are comparisons with model atmospheres and synthetic spectra only. In order to check if the new models are valid, comparisons to obversations are required.
DENIS J0205-1159 (D0205) was first discoverd by Delfosse et al. (1997) and categorized as L7 with $J - K = 1.53$. It turned out, that D0205 is a binary consisting of identical dwarfs (Leggett et al., 2001). Their effective temperatures had been determined to be 1650 K (Golimowski et al., 2004), 1563 K (Vrba et al., 2004), and 1601 K (Dahn et al., 2002). Spectra of D0205 were taken e.g. by Leggett et al. (2001); Reid et al. (2001) and are available electronically.

An ad hoc comparison was done with a SETTLING and DRIFT model with

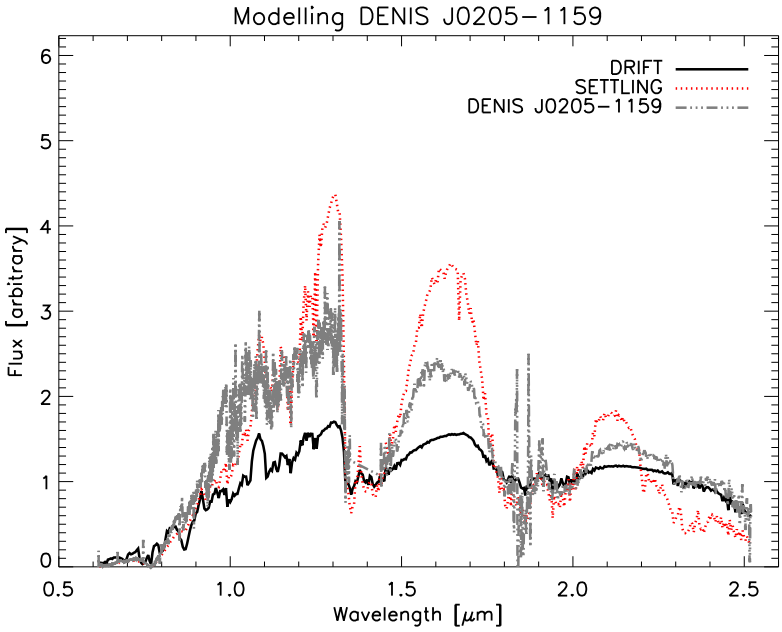

Figure 4.36: Near infrared spectrum of DENIS J0205-1159 (gray) and arbitrary scaled fluxes of a DRIFT (black) and SETTLING model (red) with $T_{\rm eff} = 1600$, $\log g = 5.0$, and [Fe/H]= 0.0.

$T_{\rm eff} = 1600$ K, $\log g = 5.0$, and [Fe/H]= 0.0. The model has an $J - K$ colour index of 1.88. Figure 4.36 shows the spectrum of D0205 (gray) in the range from 0.5 to 2.5 μm. The flux of D0205 and the DRIFT (black) and SETTLING spectra (red) is scaled arbitrarily and is normalized to the water bands at 1.4 and 1.9 μm.
Both models do not fit: Fluxes of the SETTLING model are too large, either in the J- and H-band and partially in the K-band. On the other hand, the flux of the DRIFT model is suppressed again by dust in all bands. Only the CO band head at 2.3 μm fits.
Comparisons with DUSTY models are presented in Leggett et al. (2001). They found the best fit for $T_{\rm eff} = 1900$ K and $\log g = 5.5$, which contradicts with results of $T_{\rm eff}$ given above. A fit with a DRIFT model with $J-K$ more similar to D0205 was carried out, because the model with $T_{\rm eff} = 1600$ K has too much dust in its atmosphere, if the

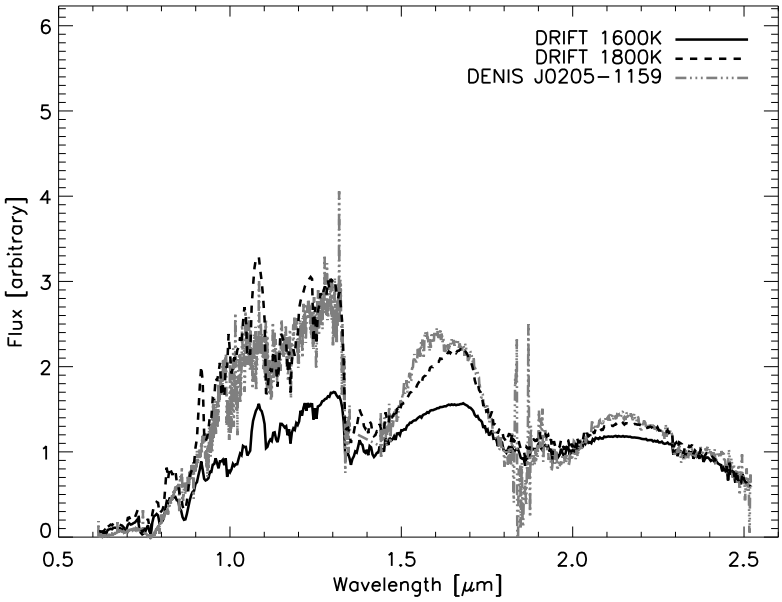

Figure 4.37: Near infrared spectrum of DENIS J0205-1159 (gray) and arbitrary scaled fluxes of a DRIFT models (black) with $T_{\rm eff}$ = 1600 (solid) and 1800 K (dashed), $\log g = 5.0$, and [Fe/H]= 0.0.

relation of section 4.5.2 is taken into account. A model with $J-K = 1.39$ is compared to the data, shown in Figure 4.37. The (rescaled) model spectrum with $T_{\rm eff} = 1800$ K fits much better. The spectrum is shifted towards the blue: The flux in J is too high and the flux in H and K too low. Additionally, there is a shift in the peaks of the H- and K-band. However, the overall fit is remarkably good.
It can be concluded, that $J-K$ colour indices give reasonable first guesses for spectral comparisons. As the amount of dust in DRIFT models is high, best fits lead to a shift in effective temperature of about 200 K. This is also true for the DUSTY models, as seen in Leggett et al. (2001).

4.6.4 Colour indices J-K of other dust models and observations

At the end of this chapter, colour indices of different dust models are shown for comparison. Synthetic spectra of models with $\log g = 5.0$ and [Fe/H]= 0.0 from Allard, Ackerman & Marley, Burrows, and Tsuji have been used[3] and have the following parameters:

- Ackerman & Marley (2001): $f_{\rm sed} = 3$
- Tsuji (2005): $T_{\rm cr} = 1800$ K
- Burrows et al. (2006): $a_0 = 100\,\mu$m

[3]See section 1.2 for a comparison of the different assumptions and additional references.

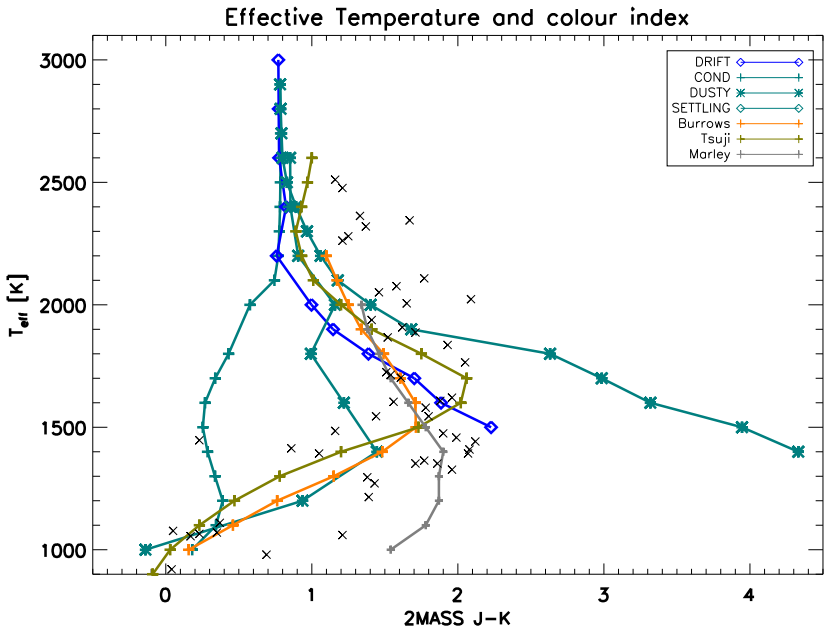

Figure 4.38: Colour indices $J-K$ (2MASS) of different dust models. Colour indices of models with $\log g = 5.0$ and [Fe/H]$= 0.0$ by Burrows (orange), Tsuji (green), and Marley (gray) are shown. For comparison, COND (cyan +), DUSTY (cyan $\star$), SETTLING (cyan $\diamond$), and DRIFT (blue) models are shown also. Observed data are indicated with gray $\times$.

A selection of observed L and T-dwarfs with given $T_{\rm eff}$ from Kirkpatrick (2005) are added to diagram 4.38. All models lie within the COND and DUSTY limits and reproduce the turning point (maximum of $J-K$, $(J-K)_{\rm max}$) from L to T-dwarfs. The $T_{\rm eff}(J-K_{\rm max})$ ranges from 1700 K (Tsuji) to 1400 K (Marley). The representation of colour indices works well in all models. At $T_{\rm eff} > 2000$ K, indices are too low by about 0.5, but selection effects on the observed objects might play a role here.
More interesting results of the DRIFT models are expected with further development of the code, which allows reaching lower $T_{\rm eff}$ and, therefore, the transition into the T-dwarf regime.

Chapter 5

Outlook

This is the first time that atmospheres of oxygen-rich brown dwarfs of late-M and L types were calculated self consistently with a non-equilibrium dust model connected to the model atmosphere code PHOENIX.
Due to this integration of the dust model and the atmosphere code, the radiative feedback adjusts the atmosphere of brown dwarfs and determines the dust properties. There are no free parameter needed in order to describe the dust formation. All dust properties in the presented models can be explained by nucleation, growth and evaporation, gravitational drift, and mixing.
It was shown that there is a type of optimum in the mean grain size. There is only a small dependency on the effective temperature, which influences the maximum mean grain radius, which reaches about 0.5 up to 1.5 μm.
Expected colour indices for brown dwarfs are reproduced quite well. The scattering of $J-K$ which is seen, e.g., in Stephens & Leggett (2004) might be explained with different element abundances and (less effective) with different $\log g$.
The dust formation in current DRIFT models is very strong. There are indications, that too much dust is formed. E.g. methane absorption in cool dwarfs (T-type, $T_{\rm eff} \lesssim$ 1600 K) cannot be observed It might be possible, that the treatment of the mixing plays a major role in this issue. Small variations in the overshoot parameter β result in large changes in n_d. It should be confirmed that β is independent of the local gas pressure or effective temperature. On the other hand, there might be a need of a complete different treatment of mixing, i.e., a kind of diffusion of the undepleted gas into the upper layers. This means, that the mixing term in the the dust moment equation has to be reformulated. If the problem of elemental mixing is solved, it might be possible that calculations towards lower effective temperatures can be performed without problems. The transition from L- to T-dwarfs might be reproduced without any changes in the self-consistent method.
The column density of dust $N = \int n_d(z)dz$ is an indication for the total amount of dust in the atmosphere and can be roughly estimated using $J-K$ photometrie for L-dwarfs. This measure might be used for comparisons with other dust models or in order to simplify spectral fitting.

Appendix A

Appendix

A.1 Basic Equations

A.1.1 Characteristics of J^*

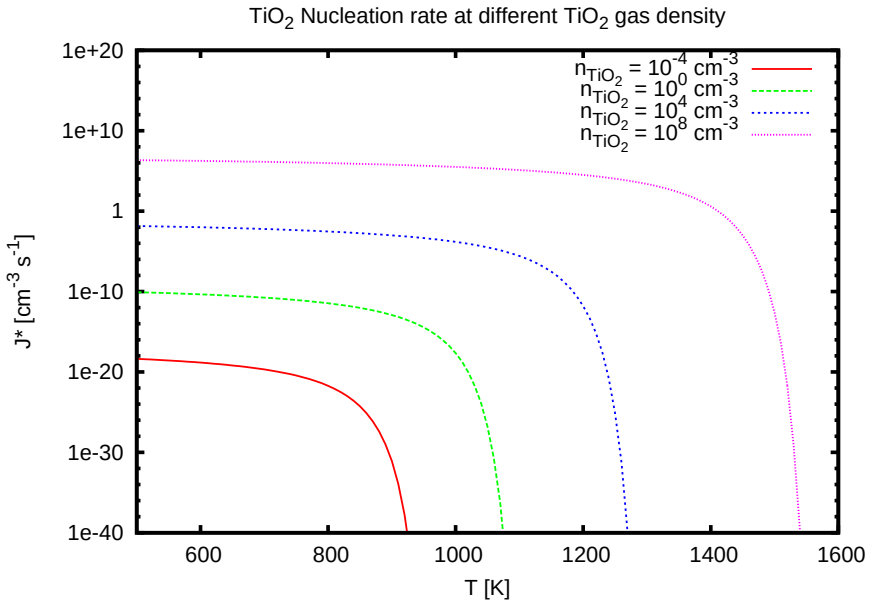

Figure A.1: Temperature dependence of the nucleation rate J^* [cm^{-3} s^{-1}] of TiO_2, for four given number densities of TiO_2: $n_{TiO_2} = 10^{-4}$, 1, 10^4, and 10^8 cm^{-3}.

As shown in the first chapter, the nucleation rate J^* of TiO_2 can be expressed as

$$J^* = \frac{n_{TiO_2}}{\tau} Z \exp\left[(N_* - 1)\ln S - \left(\frac{T_\Theta}{T}\right)(N_* - 1)^{2/3}\right],$$

where J^* is essentially a function of the number density of gaseous TiO_2 (n_{TiO_2}) and temperature T. The temperature dependency of some values of n_{TiO_2} is shown in Figure A.1. The number density of TiO_2 ranges from 10^{-4}, 1, 10^4, to 10^8 particles per cm^3. Typical values in a model atmospheres with $T_{\rm eff} = 2000$ K range from about

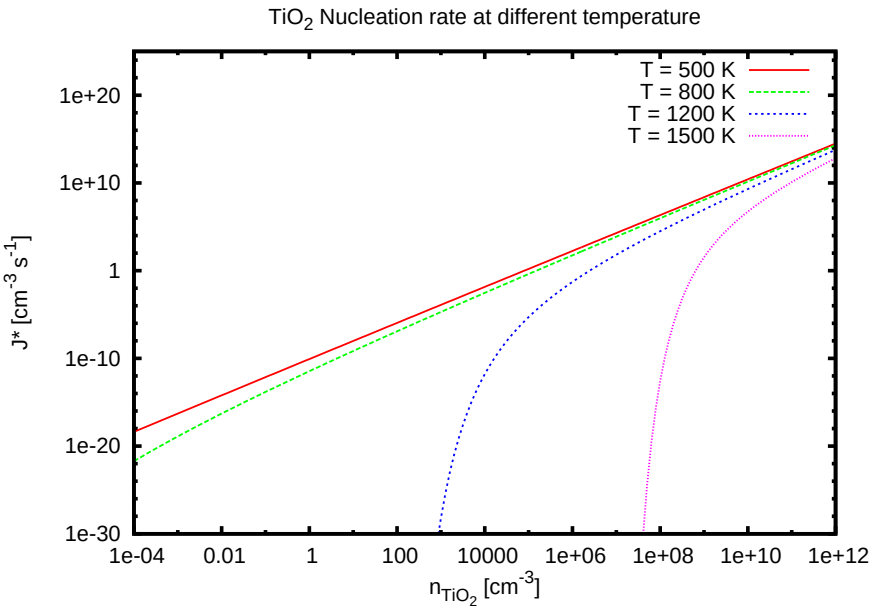

Figure A.2: Nucleation rate J^* [cm^{-3} s^{-1}] of TiO_2, dependent of number density of TiO_2 with four given temperatures: $T = 500$, 800, 1200, and 1500 K.

$1.5 \cdot 10^{-5}$ to $3 \cdot 10^{10}$ gaseous TiO_2 molecules per cm^3. Depending on the TiO_2 density, the nucleation rate is only approximately linear at sufficiently low temperatures
Values of J^* at four fixed temperatures ($T = 500$, 800, 1200, 1500 K) and variable n_{TiO_2} are shown in Figure A.2. At sufficiently low temperatures or high densities, $J^* \propto n^2_{TiO_2}$ is a good approximation as the exponential part approaches unity.

A.2 Approach

A.2.1 Implementation

This chapter describes roughly the implementation of the new dust module and gives information for experienced PHOENIX users and developers. The implementation is based on the PHOENIX release `15.01`.

Using the DRIFT module

In order to use the DRIFT module, some settings in the `phoenix` namelist have to be changed. The module is invoked, if `use_drift` is set true (`t`). The default is `use_drift = f`. In this case, the known dust routines (COND, DUSTY, SETTLING) can be used. In addition, the calculation of the dust opacity has to be selected (`driftOpac = t`). These settings in the namelist are sufficient in order to activate the DRIFT module. The value for β is reflected in `driftOvershoot` and defaults to 2.2. Other settings concerning DRIFT and their default values are shown in table A.1. It is not recommended to change any of these values.

Namelist parameter			
Variables	Type	Default	Description
Main switches:			
`use_drift`	logical	F	Activates the dust module DRIFT.
`driftOpac`	logical	F	If `false`, dust opacity is ignored.
`driftExport`	logical	T	Writes exchange file, overrides `use_drift=.false.`
Overshooting:			
`driftOvershoot`	real	2.2	Overshoot parameter β
Assumptions:			
`driftDustType`	integer	0	0: Volume fraction dependent optical properties 1: "astrophysical silicate" optical properties
`driftEMT`	integer	2	Effective medium theory: 0: volume weighted sum 1: Lorentz-Lorenz 2: Bruggeman 3: Maxwell-Garnet
`driftMieType`	integer	1	Mie routine: 0: Small particle limit 1: MIEX (Wolf) 2: MIEV (Wiscombe)
`driftRefMode`	integer	0	Physical reference frame in exchange files: 0: $\rightarrow$ 3 1: z [cm] 2: T [K] 3: $P_{\rm gas}$ [dyn cm^{-2}] 4: ρ [g cm^{-}3]
`driftSingleSize`	logical	F	F: Uses grain size distribution
Testing/debugging:			
`driftEveryIter`	integer	1	DRIFT invoked every `EveryIter` iteration.
`driftFirstIter`	integer	1	Counting of `EveryIter` starts at that iteration.
`driftHydroFirst`	logical	T	F: In first iteration, PHOENIX uses the atmosphere structure in the exchange file. (Very dangerous!)
`driftOpacFac`	real	1.0	Dust opacity is multiplied with `OpacFac`.
`driftOpacStep`	real	0.0	`OpacFac=OpacFac+OpacStep` in next iteration.
`driftOpacMax`	real	1.0	`OpacFac` limits to `OpacMax` (for `OpacStep`>0).
`driftReadOpacs`	logical	F	Read dust opacities from last iteration.
`driftSWTest`	logical	F	After running `static_weather`, PHOENIX stops.
`driftSWVersion`	integer	0	0: Current version of DRIFT. (Should not be changed)

Table A.1: Parameters in PHOENIX namelist used for control of dust module. Locical values F means`.false.`, T `.true.`. For abbreviation, the prefix ``drift'' is omitted in the description. For the most of the variables, the default values are sufficient (except for `use_drift` and `driftOpac`) and should not be changed, except for testing or debugging purposes. "real" means always `real(kind=8)` or `REAL*8` resp.

Filelist

File	Description
`2Drift.data`	Exchange file, passed to DRIFT every iteration
`2Phoenix.data`	Exchange file, passed to PHOENIX every iteration
`*.nk`	Optical data of dust species, e.g. `MgO.nk`
`out3_*.dat`	Results of the DRIFT module, generated every iteration
`driftresults.dat`	Dust properties of the latest iteration, generated every iteration
`miexresults.dat`	Optical properties of the latest iteration, generated every iteration

Table A.2: List of files used/generated by PHOENIX or the DRIFT module.

Getting the results

Results can be obtained in the usual `fort.6` and `fort.7` files. More results are found in the files as shown in table A.2. Every file is written in `ASCII` format. Optical data (`*.nk`) are available in the directory referred by the system variable `$ALGAMDAT2`.
The most useful file might be `driftresults` which contains `layer` lines (plus one header line) with the following layer dependent properties:

1. Atmosphere structure: $P_{\rm gas}$ [bar], T [K], $\tau_{\rm std}$, z [cm]
2. Main dust properties:
   $<a>$ [cm], n_d [cm^{-3}], $\chi_{\rm net}$ [cm s^{-1}], J^* [cm^{-3} s^{-1}], ρ_d [g cm^{-3}]
3. Grain compsition: Volume fractions of each dust species
4. Grain size distribution: $a_1,\ a_2$ [cm], $N_1,\ N_2$ [cm^{-3}]
5. Saturation ratios of each dust species
6. Flux: $F_{\rm conv},\ F_{\rm total}$ [erg s^{-1}]
7. Velocities: $v_{\rm conv},\ v_{\rm drift}$ [cm s^{-1}]
8. Accelerations: $a_{\rm total},\ a_{\rm dust}$ [cm s^{-2}]
9. Mixing: $\tau_{\rm mix}$ [s]

Developing PHOENIX+DRIFT

A complete description of the implementation or printing parts of the source code would exceed the scope of this work. Changes in the source code of PHOENIX concerning DRIFT can be found easily if the string `use_drift` is searched. The DRIFT module is developed by the authors of Woitke & Helling (2003, 2004); Helling & Woitke (2006); Helling et al. (2007).
In PHOENIX, the implementation of DRIFT affects mainly the source files

- `phoenix.f` (main logic)
- `FPPRESS/ppress.f` (depletion of elements)

- `KAPCAL/vcapcnt.f` (adjusting opacities)
- `KAPCAL/kapcal.f` (dito)

Additional source files can be found in the directory `DRIFT/`.

Variables which are used in PHOENIX are located in the FORTRAN modules `drift` (see table A.3) and `miexchg` (table A.4). The data transfer between PHOENIX and DRIFT is performed to 100% via the exchange files `2Drift.data` and `2Phoenix.data`, which are generated during processing.

DRIFT module

Variables	Type	Default	Description
Static parameters:			
`maxElementCount` **E**	integer	nvemx[1]	Numbers of elements
`maxLayers` **L**	integer	layer[1]	Atmosphere layers
`maxWave` **W**	integer	601	Wavelength points[2]
`maxDustComponents` **D**	integer	20	Maximum dust species
Namelist parameters,	**see table A.1**		
Dust properties:			
`driftAQuer`	real(**L**)	-	Grain radii <a> [cm]
`driftN`	real(**L**)	-	Dust number density n_d [cm-3]
`driftRhoD`	real(**L**)	-	Dust material density ρ_d [g cm^{-3}]
`driftTauMix`	real(**L**)	-	Mixing time scale $\tau_{\rm mix}$ [s]
`driftVQuer`	real(**L**)	-	Drift velocity $v_{\rm drift}$ [cm s-1]
`driftChinet`	real(**L**)	-	growth rate $\chi_{\rm net}$ [cm s^{-1}]
`driftJstar`	real(**L**)	-	nucleation rate J^* [cm^{-3} s^{-1}]
`driftSat`	real(**D**,**L**)	-	Saturation ratio S
`driftVolFrac`	real(**D**,**L**)	-	Volume fractions of dust grains
`driftRefract`	complex(**W**,**L**)	-	Refractive indices m of dust
`driftDustRefract`	complex(**D**,**W**)	-	Refractive indices m of each species
`driftEheu`	real(**E**,**L**)	-	Depleted element abundances
`driftDist`	real(4, **L**)	-	Parameters of $f(a)$ $\rightarrow$`driftDistMode`
`driftEheu`	real(**E**,**L**)	-	Depleted element abundances
`driftDustMoment`	real(4, **L**)	-	Dust moments, (i,:) = L_{i-1}
Misc.:			
`driftConsideredElements`	logical(**E**)	-	Considered element abundances
`driftDist`	real(4, **L**)	-	Parameters of $f(a)$ $\rightarrow$`driftDistMode`
`driftDistMode`	integer	1	Grain size distribution: 1: $f(a) = \sum_1^2 N_i \delta(a - a_i)$ 2: $f(a)_{AAA,BBB,CCC}$ 3: $f(a)_{N,a1,sigma}$
`driftDustName`	string(**D**)	-	Name of dust components
`driftLogg`	real	-	$\log g$ of read DRIFT model
`driftRef`	real(4,4)	-	Boundaries of physical reference frame, see (`RefMode`): (:,1): min property of PHOENIX (:,2): max property of PHOENIX (:,3): min property of DRIFT (:,4): max property of DRIFT
`driftTeff`	real	-	$T_{\rm eff}$ of read DRIFT model
`driftTime`	real	-	Time [s] spend in DRIFT
`driftWave`	real(**W**)	-	Wavelengths of dust opacities

Table A.3: Main definitions of module `drift`, found in `./driftmod.f`. Most of the defined variables are also found in the namelist variables.

MIEXCHG module

Variables	Type	Default	Description
mieNmax **W**	integer	601	Wavelength points
mieNlayer **L**	integer	256	Atmosphere layers
mieUsed	logical	F	Indicates, if Mie routine was used this run
mieCalcDone	logical(**L**)	F	T: Mie calculation done in layer
mieRmin	real	-	Minimum grain radius [μm]
mieRmax	real	-	Maximum grain radius [μm]
mieTime	real	-	Time of Mie run [s]
mieN	integer	-	Number of wavelength points
mieR	real(**L**)	-	Grain radius [μm]
mieLambda	real(**L**,**W**)	-	Wavelength points [Å]
mieQext	real(**L**,**W**)	-	Extinction efficiency $Q_{\rm ext}$
mieQsca	real(**L**,**W**)	-	Scattering efficiency $Q_{\rm sca}$
mieQabs	real(**L**,**W**)	-	Absorption efficiency $Q_{\rm abs}$
mieQbk	real(**L**,**W**)	-	Background scattering $Q_{\rm bk}$
mieCext	real(**L**,**W**)	-	Extinction cross section $C_{\rm ext}$ [m^2]
mieCsca	real(**L**,**W**)	-	Scattering cross section $C_{\rm sca}$ [m^2]
mieCabs	real(**L**,**W**)	-	Absorption cross section $C_{\rm abs}$ [m^2]
mieCbk	real(**L**,**W**)	-	Background scattering cross section $C_{\rm bk}$ [m^2]
mieQpr	real(**L**,**W**)	-	Radiation pressure efficiency factor

Table A.4: Main definitions of module `miexchg`, found in `./miexchg.f`.

A.2.2 Growth reactions

The following growth reactions are considered:

1 TiO_2	$\leftrightarrow$ 1 TiO_2[s]
1 TiO + 1 H_2O	$\leftrightarrow$ 1 TiO_2[s] + 1 H_2
1 Ti + 2 H_2O	$\leftrightarrow$ 1 TiO_2[s] + 2 H_2
1 TiS + 2 H_2O	$\leftrightarrow$ 1 TiO_2[s] + 1 H_2S + 1 H_2
2 Mg + 1 SiO + 3 H_2O	$\leftrightarrow$ 1 Mg_2SiO_4[s] + 3 H_2
2 MgOH + 1 SiO + 1 H_2O	$\leftrightarrow$ 1 Mg_2SiO_4[s] + 2 H_2
2 $Mg(OH)_2$ +1 SiO	$\leftrightarrow$ 1 Mg_2SiO_4[s] + 1 H_2O + 1 H_2
2 Mg + 1 SiS + 4 H_2O	$\leftrightarrow$ 1 Mg_2SiO_4[s] + 1 H_2S + 3 H_2
2 MgOH + 1 SiS + 2 H_2O	$\leftrightarrow$ 1 Mg_2SiO_4[s] + 1 H_2S + 2 H_2
2 $Mg(OH)_2$ + 1 SiS	$\leftrightarrow$ 1 Mg_2SiO_4[s] + 1 H_2 + 1 H_2S
1 SiO_2	$\leftrightarrow$ 1 SiO_2[s]
1 SiO + 1 H_2O	$\leftrightarrow$ 1 SiO_2[s] + 1 H_2
1 SiS + 2 H_2O	$\leftrightarrow$ 1 SiO_2[s] + 1 H_2 + 1 H_2S
1 Fe	$\leftrightarrow$ 1 Fe[s]
1 FeO + 1 H_2	$\leftrightarrow$ 1 Fe[s] + 1 H_2O
1 FeS + 1 H_2	$\leftrightarrow$ 1 Fe[s] + 1 H_2S
1 $Fe(OH)_2$ + 1 H_2	$\leftrightarrow$ 1 Fe[s] + 2 H_2O
2 AlOH + 1 H_2O	$\leftrightarrow$ 1 Al_2O_3[s] + 2 H_2
2 AlH + 3 H_2O	$\leftrightarrow$ 1 Al_2O_3[s] + 4 H_2
1 Al_2O + 2 H_2O	$\leftrightarrow$ 1 Al_2O_3[s] + 2 H_2
2 AlS + 3 H_2O	$\leftrightarrow$ 1 Al_2O_3[s] + 2 H_2S + 1 H_2
2 AlO_2H	$\leftrightarrow$ 1 Al_2O_3[s] + 1 H_2O
1 MgO	$\leftrightarrow$ 1 MgO[s]
1 Mg + 1 H_2O	$\leftrightarrow$ 1 MgO[s] + 1 H_2
2 MgOH	$\leftrightarrow$ 2 MgO[s] + 1 H_2
1 $Mg(OH)_2$	$\leftrightarrow$ 1 MgO[s] + 1 H_2O
1 Mg + 1 SiO + 2 H_2O	$\leftrightarrow$ 1 $MgSiO_3$[s] + 2 H_2
2 MgOH + 2 SiO + 2 H_2O	$\leftrightarrow$ 2 $MgSiO_3$[s] + 3 H_2
1 $Mg(OH)_2$ + 1 SiO	$\leftrightarrow$ 1 $MgSiO_3$[s] + 1 H_2
1 Mg + 1 SiS + 3 H_2O	$\leftrightarrow$ 1 $MgSiO_3$[s] + 1 H_2S + 2 H_2
2 MgOH + 2 SiS + 4 H_2O	$\leftrightarrow$ 2 $MgSiO_3$[s] + 2 H_2S + 3 H_2
1 $Mg(OH)_2$ + 1 SiS + 1 H_2O	$\leftrightarrow$ 1 $MgSiO_3$[s] + 1 H_2S + 1 H_2

A.2.3 Molecule sets in PHOENIX

Calculation have been performed with two molecule sets in PHOENIX. The large set comprises 318 species and the reduced set 47, which turned out to be sufficient for this work. However, no significant differences concerning calculation time were found.

Large molecule set used in PHOENIX (318 species):
COH_2, CNOH, OH, CH, NH, C_2, CN, CO, MgH, CaH, SiH, TiO, H_2O, H_2, N_2, NO, CO_2, O_2, ZrO, VO, MgS, SiO, AlH, HCl, HF, SH, TiH, AlO, BO, CrO, LaO, MgO, ScO, YO, SiF, NaCl, CaOH, HCN, C_2H_2, CH_4, CH_2, C_2H, HCO, NH_2, LiOH, C_2O,

AlOF, NaOH, MgOH, AlO_2, Al_2O, AlOH, SiH_2, SiO_2, SH_2, OCS, KOH, TiO_2, TiOCl, VO_2, FeF_2, YO_2, ZrO_2, BaOH, LaO_2, C_2H_4, C_3, SiC_2, CH_3, C_3H, NH_3, C_2N_2, C_2N, CaF_2, AlOCl, Si_2C, CS_2, $CaCl_2$, AlF, CaF, Si_2, SiS, CS, AlCl, KCl, CaCl, TiS, TiCl, SiN, AlS, Al_2, FeO, FeF, SiC, TiF_2, FeH, LiCl, LiOCl, NS, NaH, SO, S_2, AlC, AlN, CP, CaO, CaS, FeCl, B_2, BC, BCl, BF, BH, BN, BS, BaCl, BaF, BaO, BaS, BeCl, BeF, BeH, BeN, BeO, BeS, Mg_2, MgN, MnO, MnS, PN, TiN, VN, ZrN, Na_2, NaO, NbO, NiO, NiS, PO, SrO, P_2, PS, ScS, SrS, YS, ZrS, Cl_2, CoCl, CuCl, FCl, MgCl, NiCl, OCl, PCl, SCl, SiCl, SrCl, NiH, ZrCl, CrH, CrN, Cu_2, CuF, CuH, CuO, CuS, F_2, KF, LiF, MgF, NF, NaF, OF, PF, SF, SrF, TiF, ZrF, FeS, KH, LiH, MnH, PH, SrH, ZrH, $AlBO_2$, AlClF, $AlCl_2$, AlF_2, $AlOF_2$, Al_2O_2, $BeBO_2$, OBF, HBO, HBO_2, HBS, BH_2, BO_2H_2, BH_3, BO_3H_3, KBO_2, $LiBO_2$, $NaBO_2$, BO_2, $BaCl_2$, BaF_2, BaO_2H_2, BaClF, $BeCl_2$, BeF_2, BeOH, BeH_2, BeO_2H_2, Be_2O, Be_3O_3, CNCl, CHCl, CHF, CHP, CH_3Cl, KCN, NaCN, BeC_2, C_2HCl, C_2HF, $Na_2C_2N_2$, CaO_2H_2, MgClF, SiH_3Cl, $FeCl_2$, K_2Cl_2, $MgCl_2$, Na_2Cl_2, $TiOCl_2$, $SrCl_2$, $TiCl_2$, $ZrCl_2$, $TiCl_3$, $ZrCl_3$, $ZrCl_4$, CrO_2, SiH_3F, TiOF, SiH_2F_2, MgF_2, SrF_2, ZrF_2, TiF_3, ZrF_4, N_2O, NHO_3, FeO_2H_2, SrOH, $K_2O_2H_2$, $Li_2O_2H_2$, MgO_2H_2, $Na_2O_2H_2$, SrO_2H_2, PH_2, PH_3, SiH_4, Si_2N, PO_2, SO_2, ClOH, ClO_2, OHF, HO_2, NOH, O_3, S_2O, O_2H_2, SiH_3, NO_2H, SO_3, LiNaO, PSF, PF_2, PCl_3, SF_6, COF_2, CrO_3, $NiCl_2$, P_4, Si_3, NO_2, NO_3, CsCl, CsOH, Cs_2, CsF, RbCl, OH^-, CH^-, C_2^-, CN^-, SiH^-, H_2^-, SH^-, CS^-, FeO^-, BO^-, $AlCl_2^-$, AlF_2^-, $AlOF_2^-$, CO_2^-, NO^+, H_2^+, TiO^+, ZrO^+, $AlOH^+$, $BaOH^+$, HCO^+, $CaOH^+$, Al_2O^+, $SrOH^+$, H_3O^+, H_3^+

Reduced molecule set used in PHOENIX (47 species):
H_2, CO, CO_2, H_2O, N_2, SiO, CH_4, TiO, VO, TiO_2, TiS, SiS, SiO_2, H_2S, MgO_2H_2, FeH, FeO, FeS, FeO_2H_2, AlOH, AlH, AlS, AlO_2, AlO, CH, NH, OH, MgH, CaH, SiH, C_2, CN, NO, OH^-, CH^-, C_2^-, CN^-, SiH^-, H_2^-, SH, FeO^-, CO_2^-, NO^+, H_2^+, TiO^+, $AlOH^+$, SH^-

A.3 Results

A.3.1 Large variations in β

In contrast to section 4.2.4, the gradient of mixing time scale β which defaults to 2.2, was changed larger. The results are shown in Figure A.3: Beta was changed to 1.1 and 3.3 and its corresponding models ($T_{\text{eff}} = 2300$ K) are compared with a standard model with $\beta = 2.2$. A smaller gradient ($\beta = 1.1$) results in much shorter mixing time scales. Therefore, much more "fresh" elements are available for dust formation, resulting in much number larger dust densities. The change in the temperature structure indicates that dust is not neglectable anymore. On the other hand, if β is set to 3.3, less than a number fraction of 1/10 of dust particles is formed, relative to a model with $\beta = 2.2$.

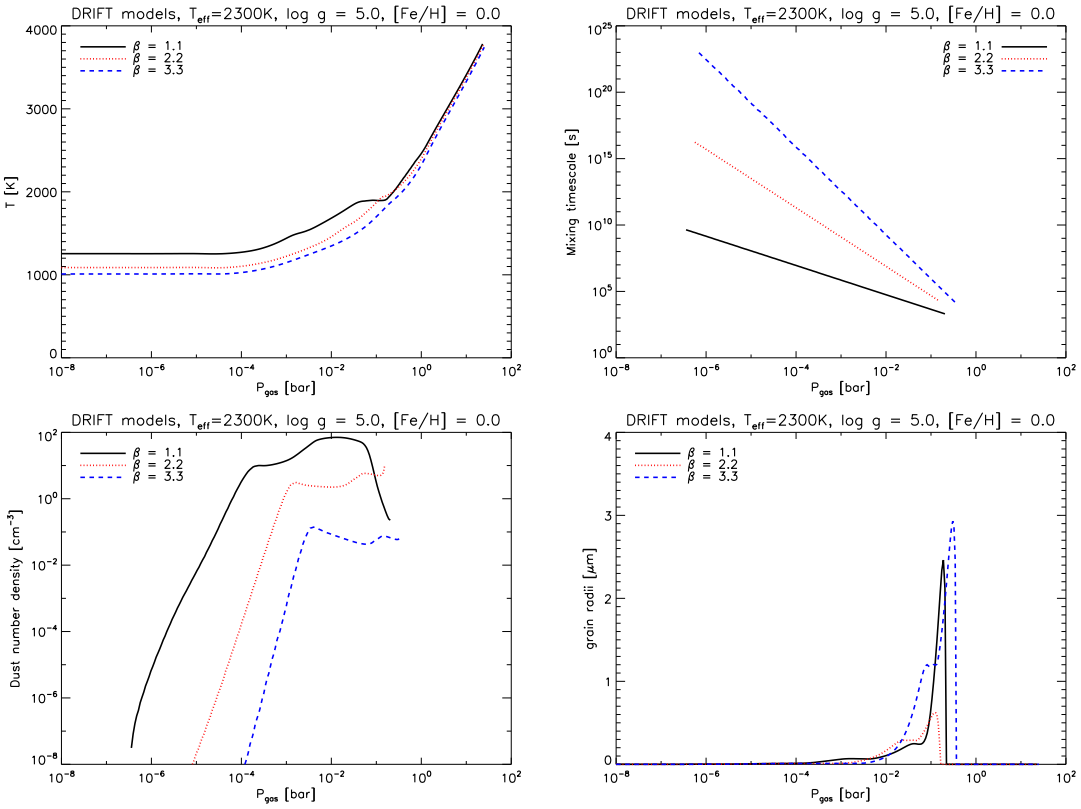

Figure A.3: Influence of different gradients β in determing the mixing time scale $\tau_{\rm mix}$ on dust formation is shown on a model with $T_{\rm eff} = 2300$ K. Temperature structure of models with different $\beta = 1.1$, 2.2 and 3.3 is shown in the top left picture. Corresponding mixing time scale $\tau_{\rm mix}$ is on the right picture. In the lower panel, dust number densities and mean grain radii are presented. Deviations of dust number densities related to $n_d(\beta = 2.2)$ are larger than one order of magnitude.

A.4 Data

A.4.1 Optical data

The subsequent plots show the used complex refractive indices ($m = n + ik$) of the dust species used in this work. Treatment of these data is described in chapter 2.2.1.

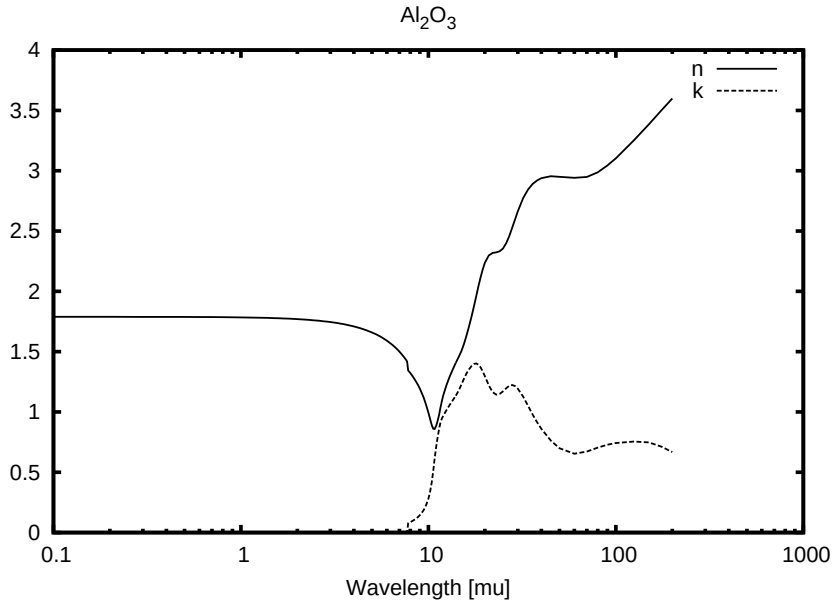

Figure A.4: Optical data of corundum (Al_2O_3) (Palik, 1991; Begemann et al., 1997)

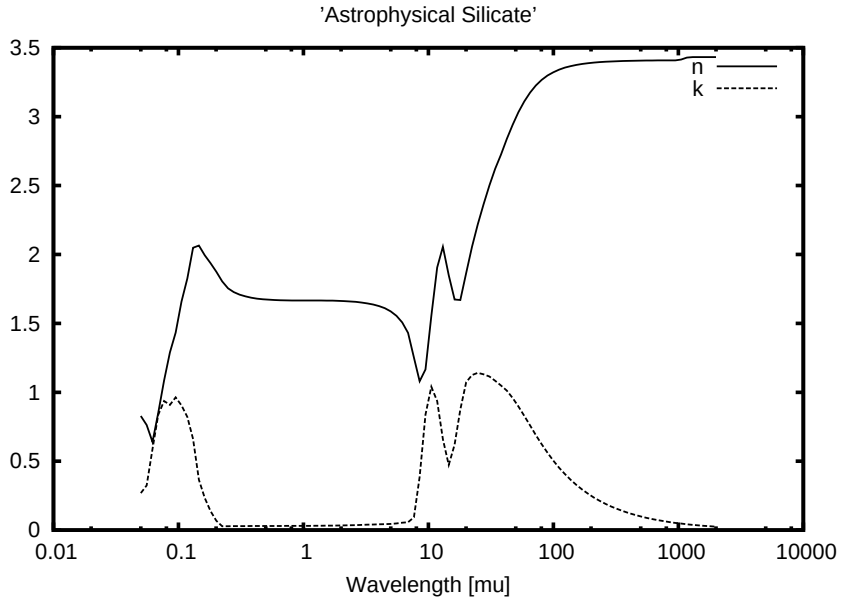

Figure A.5: Optical data of "astrophysical silicate" (Draine, 1985)

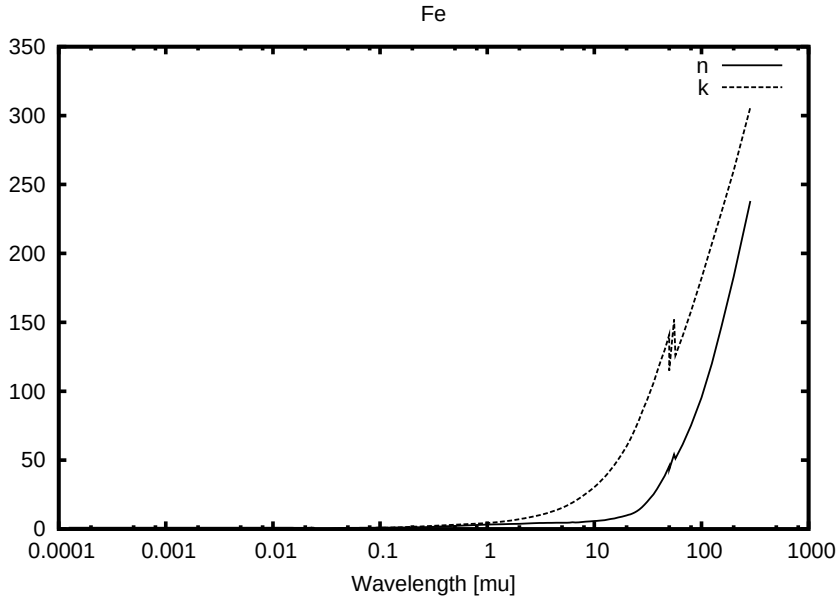

Figure A.6: Optical data of iron (Fe) (Palik, 1985, 1991)

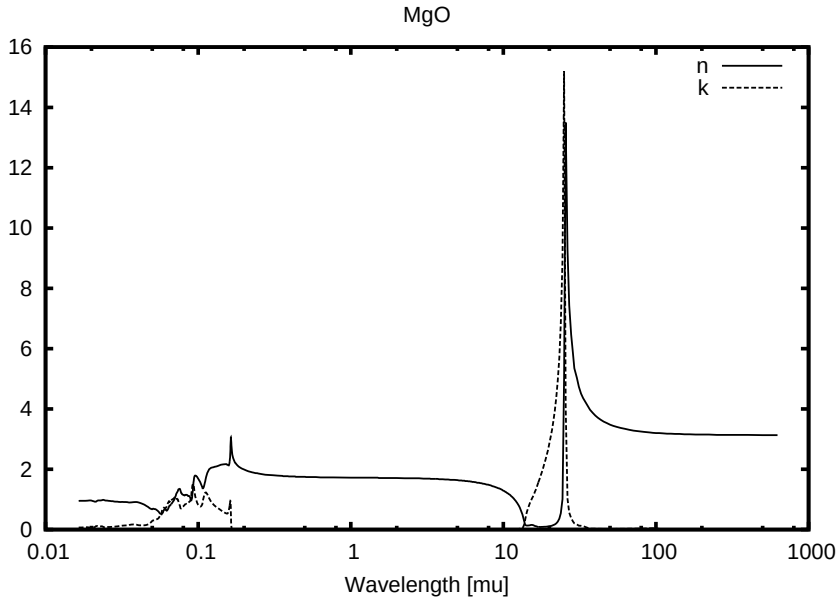

Figure A.7: Optical data of MgO (Palik, 1985, 1991)

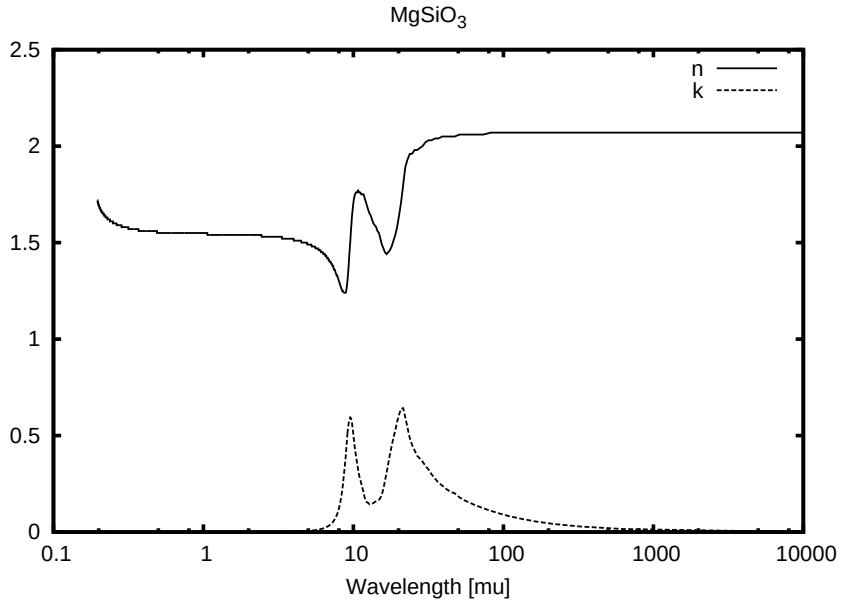

Figure A.8: Optical data of $MgSiO_3$ (Jäger et al., 2003)

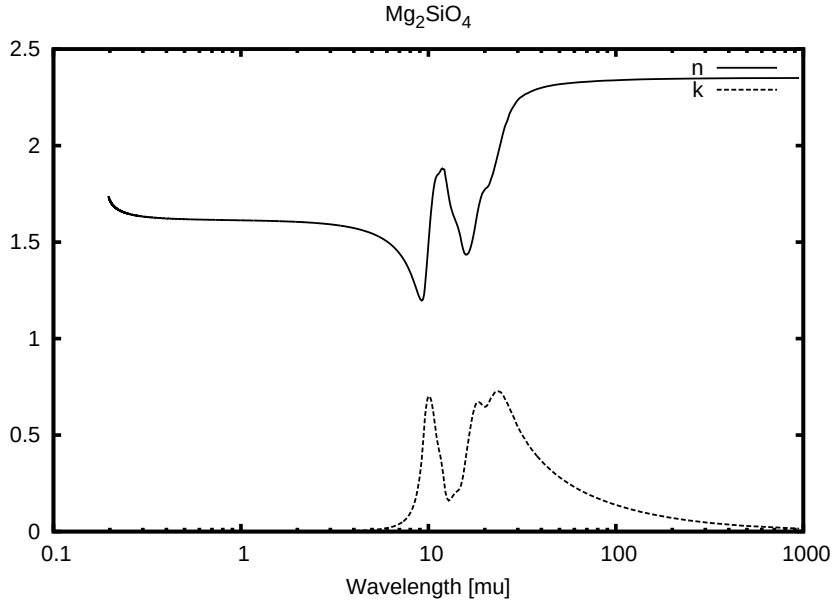

Figure A.9: Optical data of Mg_2SiO_4 (Jäger et al., 2003)

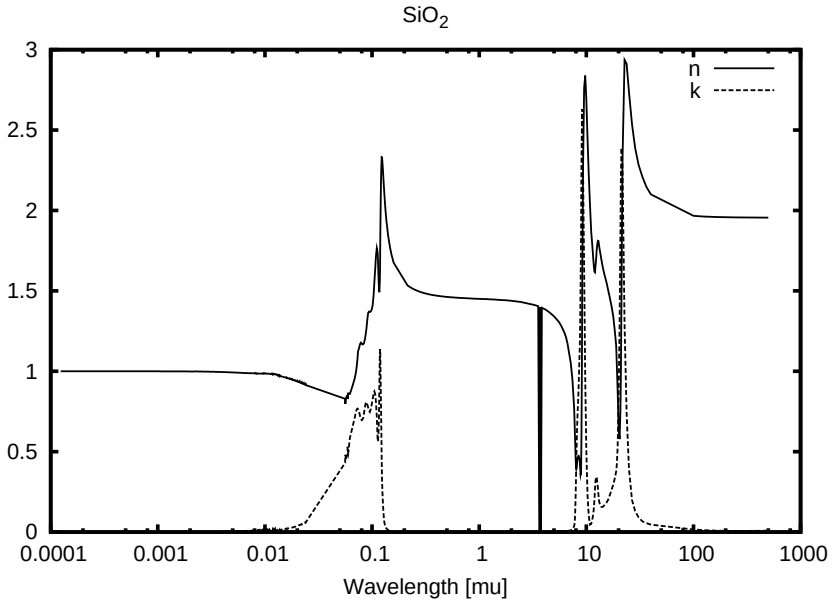

Figure A.10: Optical data of SiO_2 (Palik, 1985, 1991)

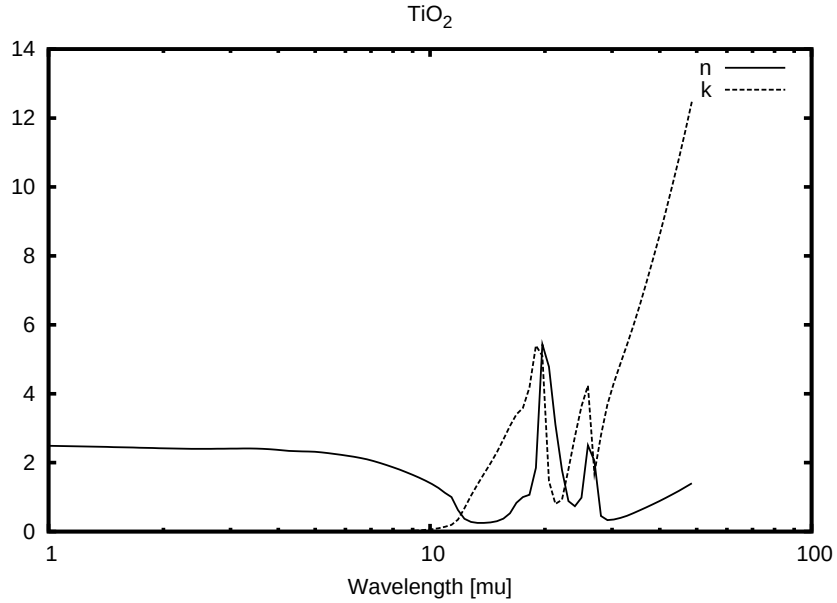

Figure A.11: Optical data of rutile (TiO_2) (Posch, 1999)

List of Figures

List of Tables

Bibliography

Ackerman, A. S. & Marley, M. S. 2001, Precipitating Condensation Clouds in Substellar Atmospheres, Astrophysical Journal, 556, 872

Allard, F., Guillot, T., Ludwig, H., et al. 2003, in IAU Symposia, Vol. 211, Brown Dwarfs, ed. E. Martín, International Astronomical Union (San Francisco: Astronomical Society of the Pacific), 325–332

Allard, F. & Hauschildt, P. H. 1995, Model atmospheres for M (sub)dwarf stars. 1: The base model grid, Astrophysical Journal, 445, 433

Allard, F., Hauschildt, P. H., Alexander, D. R., & Starrfield, S. 1997, Model Atmospheres of Very Low Mass Stars and Brown Dwarfs, Annual Review of Astronomy and Astrophysics, 35, 137

Allard, F., Hauschildt, P. H., Alexander, D. R., Tamanai, A., & Schweitzer, A. 2001, The Limiting Effects of Dust in Brown Dwarf Model Atmospheres, Astrophysical Journal, 556, 357

Allard, F., Hauschildt, P. H., Baraffe, I., & Chabrier, G. 1996, Synthetic Spectra and Mass Determination of the Brown Dwarf GI 229B, Astrophysical Journal Letters, 465, L123+

Allard, F., Hauschildt, P. H., & Schweitzer, A. 2000, Spherically Symmetric Model Atmospheres for Low-Mass Pre-Main-Sequence Stars with Effective Temperatures between 2000 and 6800 K, Astrophysical Journal, 539, 366

Aspnes, D. E., Theeten, J. B., & Hottier, F. 1979, Investigation of effective-medium models of microscopic surface roughness by spectroscopic ellipsometry, Phys. Rev. B, 20, 3292

Baron, E. & Hauschildt, P. H. 1998, Parallel Implementation of the PHOENIX Generalized Stellar Atmosphere Program. II. Wavelength Parallelization, Astrophysical Journal, 495, 370

Becker, R. & Döring, W. 1935, Kinetische Behandlung der Keimbildung in übersättigten Dämpfen, Ann. Phys. (Leipzig), 24, 719

Begemann, B., Dorschner, J., Henning, T., et al. 1997, Aluminum Oxide and the Opacity of Oxygen-rich Circumstellar Dust in the 12–17 Micron Range, Astrophysical Journal, 476, 199

Biermann, L. 1932, Untersuchungen über den inneren Aufbau der Sterne, IV. Konvektionszonen im Inneren der Sterne, Veroeffentlichungen der Universitaets-Sternwarte zu Goettingen, 2, 220

Boren, C. F. & Huffman, D. R. 1983, Absorption and Scattering of Light by Small Particles (Wiley-Interscience, New York)

Bronstein, I. N. & Semendjajew, K. A. 1997, Taschenbuch der Mathematik, 3rd edn. (Thun; Frankfurt am Main: Harri Deutsch)

Brown, P. D., Duley, W. W., Jones, A. P., & Williams, D. A. 1989, HAC-coated silicate grains and PAHs in diffuse clouds and low-velocity shocks, Monthly Notice of the Royal Astronomical Society, 241, 753

Bruggeman, D. A. G. 1935, The calculation of various physical constants of heterogeneous substances. I. The dielectric constants and conductivities of mixtures composed of isotropic substances, Annalen der Physik, Leipzig, 24, 636

Burgasser, A. J., Kirkpatrick, J. D., Brown, M. E., et al. 2002, The Spectra of T Dwarfs. I. Near-Infrared Data and Spectral Classification, Astrophysical Journal, 564, 421

Burrows, A., Burgasser, A. J., Kirkpatrick, J. D., et al. 2002, Theoretical Spectral Models of T Dwarfs at Short Wavelengths and Their Comparison with Data, Astrophysical Journal, 573, 394

Burrows, A., Hubbard, W. B., Lunine, J. I., & Liebert, J. 2001, The theory of brown dwarfs and extrasolar giant planets, Reviews of Modern Physics, 73, 719

Burrows, A. & Sharp, C. M. 1999, Chemical Equilibrium Abundances in Brown Dwarf and Extrasolar Giant Planet Atmospheres, Astrophysical Journal, 512, 843

Burrows, A., Sudarsky, D., & Hubeny, I. 2006, L and T Dwarf Models and the L to T Transition, Astrophysical Journal, 640, 1063

Cannon, C. J. 1973, Frequency-Quadrature Perturbations in Radiative-Transfer Theory, Astrophysical Journal, 185, 621

Chabrier, G. & Baraffe, I. 2000, Theory of Low-Mass Stars and Substellar Objects, Annual Review of Astronomy and Astrophysics, 38, 337

Chase, M. W., Davies, C. A., Downey, J. R., et al. 1985, JANAF Thermochemical Tables, 3rd. ed., Journal of Physical Chemistry Reference Data, 14

Clayton, R. N., Onuma, N., & Mayeda, T. K. 1971, in Lunar and Planetary Science Conference, 1417–+

Cooper, C. S., Sudarsky, D., Milsom, J. A., Lunine, J. I., & Burrows, A. 2003, Modeling the Formation of Clouds in Brown Dwarf Atmospheres, Astrophysical Journal, 586, 1320

Dahn, C. C., Harris, H. C., Vrba, F. J., et al. 2002, Astrometry and Photometry for Cool Dwarfs and Brown Dwarfs, Astronomical Journal, 124, 1170

Delfosse, X., Tinney, C. G., Forveille, T., et al. 1997, Field brown dwarfs found by DENIS, Astronomy and Astrophysics, 327, L25

Dominik, C., Sedlmayr, E., & Gail, H.-P. 1993, Dust formation in stellar winds. VI. Moment equations for the formation of heterogeneous and core-mantle grains, Astronomy and Astrophysics, 277, 578

Draine, B. T. 1985, Tabulated optical properties of graphite and silicate grains, Astrophysical Journal, Supplement, 57, 587

Draine, B. T. 2003, Interstellar Dust Grains, Annual Review of Astronomy and Astrophysics, 41, 241

Draine, B. T. & Salpeter, E. E. 1977, Time-dependent nucleation theory, The Journal of Chemical Physics, 67, 2230

Epchtein, N., de Batz, B., Capoani, L., et al. 1997, The Deep Near-Infrared Southern Sky Survey (DENIS)., The Messenger, 87, 27

Fabian, D., Jäger, C., Henning, T., Dorschner, J., & Mutschke, H. 2000, Steps toward interstellar silicate mineralogy. V. Thermal Evolution of Amorphous Magnesium Silicates and Silica, Astronomy and Astrophysics, 364, 282

Ferguson, J. W., Alexander, D. R., Allard, F., et al. 2005, Low-Temperature Opacities, Astrophysical Journal, 623, 585

Gail, H.-P., Keller, R., & Sedlmayr, E. 1984, Dust formation in stellar winds. I - A rapid computational method and application to graphite condensation, Astronomy and Astrophysics, 133, 320

Gail, H.-P. & Sedlmayr, E. 1988, Dust formation in stellar winds. IV - Heteromolecular carbon grain formation and growth, Astronomy and Astrophysics, 206, 153

Gauger, A., Sedlmayr, E., & Gail, H.-P. 1990, Dust formation, growth and evaporation in a cool pulsating circumstellar shell, Astronomy and Astrophysics, 235, 345

Golimowski, D. A., Leggett, S. K., Marley, M. S., et al. 2004, L' and M' Photometry of Ultracool Dwarfs, Astronomical Journal, 127, 3516

Grevesse, N., Noels, A., & Sauval, A. J. 1992, in Coronal Streamers, Coronal Loops, and Coronal and Solar Wind Composition, 305–308

Hauschildt, P. H. 1992, A fast operator perturbation method for the solution of the special relativistic equation of radiative transfer in spherical symmetry, Journal of Quantitative Spectroscopy and Radiative Transfer, 47, 433

Hauschildt, P. H., Allard, F., & Baron, E. 1999a, The NextGen Model Atmosphere Grid for $3000 \leq T_{\rm eff} \leq =$10,000 K, Astrophysical Journal, 512, 377

Hauschildt, P. H., Allard, F., Ferguson, J., Baron, E., & Alexander, D. R. 1999b, The NEXTGEN Model Atmosphere Grid. II. Spherically Symmetric Model Atmospheres for Giant Stars with Effective Temperatures between 3000 and 6800 K, Astrophysical Journal, 525, 871

Hauschildt, P. H., Barman, T. S., Baron, E., & Allard, F. 2003, in ASP Conf. Ser. 288: Stellar Atmosphere Modeling, ed. I. Hubeny, D. Mihalas, & K. Werner, 227–+

Hauschildt, P. H. & Baron, E. 1999, Numerical solution of the expanding stellar atmosphere problem, Journal of Computational and Applied Mathematics, 109, 41

Hauschildt, P. H., Baron, E., & Allard, F. 1997, Parallel Implementation of the PHOENIX Generalized Stellar Atmosphere Program, Astrophysical Journal, 483, 390

Hauschildt, P. H., Lowenthal, D. K., & Baron, E. 2001, Parallel Implementation of the PHOENIX Generalized Stellar Atmosphere Program. III. A Parallel Algorithm for Direct Opacity Sampling, Astrophysical Journal, Supplement, 134, 323

Hayashi, C. & Nakano, T. 1963, Evolution of Stars of Small Masses in the Pre-Main-Sequence Stages, Progress of Theoretical Physics, 30, 460

Helling, C., Oevermann, M., Lüttke, M. J. H., Klein, R., & Sedlmayr, E. 2001, Dust in brown dwarfs. I. Dust formation under turbulent conditions on microscopic scales, Astronomy and Astrophysics, 376, 194

Helling, C. & Woitke, P. 2006, Dust in brown dwarfs. V. Growth and evaporation of dirty dust grains, Astronomy and Astrophysics, 455, 325

Helling, C. & Klein, R. & Luettke, M. & Sedlmayr, E. 2001, in Hyperbolic Problems: Theory - Numeric - Applications, Freistuehler, Warnecke (eds), II, p.515 (2001), Birkhaeuser Verlag

Helling et al. 2007, in prep.

Iatì, M. A., Cecchi-Pestellini, C., Williams, D. A., et al. 2001, Porous interstellar grains, Monthly Notice of the Royal Astronomical Society, 322, 749

Jäger, C., Dorschner, J., Mutschke, H., Posch, T., & Henning, T. 2003, Steps toward interstellar silicate mineralogy. VII. Spectral properties and crystallization behaviour of magnesium silicates produced by the sol-gel method, Astronomy and Astrophysics, 408, 193

Jeong, K. S. 2000, PhD thesis, Technische Universität Berlin, Dust shells around oxygen-rich Miras and long-period variables

Jones, H. R. A. & Tsuji, T. 1997, Spectral Evidence for Dust in Late-Type M Dwarfs, Astrophysical Journal Letters, 480, L39+

Kirkpatrick, J. D. 2005, New Spectral Types L and T, Annual Review of Astronomy and Astrophysics, 43, 195

Kirkpatrick, J. D., Reid, I. N., Liebert, J., et al. 1999, Dwarfs Cooler than "M": The Definition of Spectral Type "L" Using Discoveries from the 2 Micron All-Sky Survey (2MASS), Astrophysical Journal, 519, 802

Knapp, G. R., Leggett, S. K., Fan, X., et al. 2004, Near-Infrared Photometry and Spectroscopy of L and T Dwarfs: The Effects of Temperature, Clouds, and Gravity, Astronomical Journal, 127, 3553

Krüger, D. & Sedlmayr, E. 1997, Two-fluid models for stationary dust driven winds. II. The grain size distribution in consideration of drift., Astronomy and Astrophysics, 321, 557

Kumar, S. S. 1963, The Structure of Stars of Very Low Mass., Astrophysical Journal, 137, 1121

Le Sergeant D'Hendecourt, L. B. & Lamy, P. L. 1980, On the size distribution and physical properties of interplanetary dust grains, Icarus, 43, 350

Leggett, S. K., Allard, F., Geballe, T. R., Hauschildt, P. H., & Schweitzer, A. 2001, Infrared Spectra and Spectral Energy Distributions of Late M and L Dwarfs, Astrophysical Journal, 548, 908

Leggett, S. K., Golimowski, D. A., Fan, X., et al. 2002, Infrared Photometry of Late-M, L, and T Dwarfs, Astrophysical Journal, 564, 452

Lodders, K. 1999, Alkali Element Chemistry in Cool Dwarf Atmospheres, Astrophysical Journal, 519, 793

Lodders, K. 2002, Titanium and Vanadium Chemistry in Low-Mass Dwarf Stars, Astrophysical Journal, 577, 974

Lodders, K. 2003, Solar System Abundances and Condensation Temperatures of the Elements, Astrophysical Journal, 591, 1220

Ludwig, H.-G., Allard, F., & Hauschildt, P. H. 2002, Numerical simulations of surface convection in a late M-dwarf, Astronomy and Astrophysics, 395, 99

Ludwig, H.-G., Allard, F., & Hauschildt, P. H. 2006, Energy transport, overshoot, and mixing in the atmospheres of M-type main- and pre-main-sequence objects, Astronomy and Astrophysics, 459, 599

Makse, H. A., Gland, N., Johnson, D. L., & Schwartz, L. M. 1999, Why Effective Medium Theory Fails in Granular Materials, Physical Review Letters, 83, 5070

Marley, M. S., Gelino, C., Stephens, D., Lunine, J. I., & Freedman, R. 1999, Reflected Spectra and Albedos of Extrasolar Giant Planets. I. Clear and Cloudy Atmospheres, Astrophysical Journal, 513, 879

Marley, M. S., Seager, S., Saumon, D., et al. 2002, Clouds and Chemistry: Ultracool Dwarf Atmospheric Properties from Optical and Infrared Colors, Astrophysical Journal, 568, 335

Maxwell Garnett, J. C. 1904, Colours in Metal Glasses and in Metallic Films, Royal Society of London Philosophical Transactions Series A, 203, 385

Mie, G. 1908, Beiträge zur Optik trüber Medien, speziell kolloidaler Metallösungen, Annalen der Physik, Leipzig, 25, 377

Mihalas, D. 1970, Stellar atmospheres, 1st edn. (San Francisco: Freeman)

Mihalas, D. 1978, Stellar atmospheres, 2nd edn. (San Francisco: Freeman)

Min, M., Waters, L. B. F. M., de Koter, A., et al. 2006, The shape and composition of interstellar silicate grains, ArXiv Astrophysics e-prints

Nakajima, T., Oppenheimer, B. R., Kulkarni, S. R., et al. 1995, Discovery of a Cool Brown Dwarf, Nature, 378, 463

Nakajima, T., Tsuji, T., & Yanagisawa, K. 2004, Spectral Classification and Effective Temperatures of L and T Dwarfs Based on Near-Infrared Spectra, Astrophysical Journal, 607, 499

Oppenheimer, B. R., Kulkarni, S. R., Matthews, K., & Nakajima, T. 1995, Infrared Spectrum of the Cool Brown Dwarf GL:229B, Science, 270, 1478

Ossenkopf, V. 1991, Effective-medium theories for cosmic dust grains, Astronomy and Astrophysics, 251, 210

Palik, E. D. 1985, Handbook of optical constants of solids (Academic Press Handbook Series, New York: Academic Press, 1985, edited by Palik, Edward D.)

Palik, E. D. 1991, Handbook of optical constants of solids II (Boston: Academic Press, 1991, edited by Palik, Edward D.)

Patzer, A. B. C., Chang, C., Sedlmayr, E., & Sülzle, D. 1999, Ab initio thermodynamic properties for different isomers of the Al O molecule, European Physical Journal D, 6, 57

Posch, T. 1999, private communication by Woitke & Helling (2004)

Posch, T., Kerschbaum, F., Fabian, D., et al. 2003, Infrared Properties of Solid Titanium Oxides: Exploring Potential Primary Dust Condensates, Astrophysical Journal, Supplement, 149, 437

Preibisch, T., Ossenkopf, V., Yorke, H. W., & Henning, T. 1993, The influence of ice-coated grains on protostellar spectra, Astronomy and Astrophysics, 279, 577

Press, W. H. & Flannery, B. P. 1988, Numerical Recipes in C, 1st edn. (Cambridge: Press Syndicate of the University of Cambridge)

Reid, I. N., Burgasser, A. J., Cruz, K. L., Kirkpatrick, J. D., & Gizis, J. E. 2001, Near-Infrared Spectral Classification of Late M and L Dwarfs, Astronomical Journal, 121, 1710

Rossow, W. B. 1978, Cloud microphysics - Analysis of the clouds of Earth, Venus, Mars, and Jupiter, Icarus, 36, 1

Rutten, R. J. 2002, in Stellar Atmosphere Modeling

Scharmer, G. B. 1981, Solutions to radiative transfer problems using approximate lambda operators, Astrophysical Journal, 249, 720

Sengupta, S. & Krishan, V. 2001, Probing Dust in the Atmosphere of Brown Dwarfs through Polarization, Astrophysical Journal Letters, 561, L123

Sharp, C. M. & Huebner, W. F. 1990, Molecular equilibrium with condensation, Astrophysical Journal, Supplement, 72, 417

Skrutskie, M. F., Cutri, R. M., Stiening, R., et al. 2006, The Two Micron All Sky Survey (2MASS), Astronomical Journal, 131, 1163

Stephens, D. C. & Leggett, S. K. 2004, JHK Magnitudes for L and T Dwarfs and Infrared Photometric Systems, Publications of the Astronomical Society of the Pacific, 116, 9

Sudarsky, D., Burrows, A., & Pinto, P. 2000, Albedo and Reflection Spectra of Extrasolar Giant Planets, Astrophysical Journal, 538, 885

Tarter, J. C. 1976, in Bulletin of the American Astronomical Society, 517–+

Tsuji, T. 2002, Dust in the Photospheric Environment: Unified Cloudy Models of M, L, and T Dwarfs, Astrophysical Journal, 575, 264

Tsuji, T. 2005, Dust in the Photospheric Environment. III. A Fundamental Element in the Characterization of Ultracool Dwarfs, Astrophysical Journal, 621, 1033

Tsuji, T., Nakajima, T., & Yanagisawa, K. 2004, Astrophysical Journal, 607, 511

Tsuji, T., Ohnaka, K., & Aoki, W. 1996a, Dust formation in stellar photospheres: a case of very low mass stars and a possible resolution on the effective temperature scale of M dwarfs., Astronomy and Astrophysics, 305, L1+

Tsuji, T., Ohnaka, K., Aoki, W., & Nakajima, T. 1996b, Evolution of dusty photospheres through red to brown dwarfs: how dust forms in very low mass objects., Astronomy and Astrophysics, 308, L29

Unsöld, A. 1955, Physik der Sternatmosphären, mit besonderer Berücksichtigung der Sonne. (Berlin, Springer, 1955. 2. Aufl.)

Vrba, F. J., Henden, A. A., Luginbuhl, C. B., et al. 2004, Preliminary Parallaxes of 40 L and T Dwarfs from the US Naval Observatory Infrared Astrometry Program, Astronomical Journal, 127, 2948

Witteborn, F. C., Bregman, J. D., Lester, D. F., & Rank, D. M. 1982, A search for fragmentation debris near Ursa Major Stream stars, Icarus, 50, 63

Woitke, P. & Helling, C. 2003, Dust in brown dwarfs. II. The coupled problem of dust formation and sedimentation, Astronomy and Astrophysics, 399, 297

Woitke, P. & Helling, C. 2004, Dust in brown dwarfs. III. Formation and structure of quasi-static cloud layers, Astronomy and Astrophysics, 414, 335

Wolf, S. & Voshchinnikov, N. V. 2004, Mie scattering by ensembles of particles with very large size parameters, Computer Physics Communications, 162, 113

Wright, E. L. 1989, Fractal dust grains around R Coronae Borealis stars, Astrophysical Journal Letters, 346, L89

Acknowledgments

Danksagungen

Ich bedanke mich bei den vielen Menschen, die mich darin unterstützt haben, daß diese Arbeit ein Erfolg wurde. Besonders bedanke ich mich bei

Prof. Dr. Peter Hauschildt für die Themenvergabe, die Betreuung der Arbeit und die sehr angenehme Atmosphäre in der Arbeitsgruppe, die nicht zuletzt durch reichhaltige Gruppentreffen innerhalb und außerhalb des Instituts gefördert wird,

Dr. habil. Christiane Helling für die geduldige Einarbeitung in das Thema, die äußerst angenehme und produktive Zusammenarbeit, sowie für die umfangreiche und konstruktive Kritik und die kritische Hinterfragung meiner Ergebnisse,

Dr. Peter Woitke für die geduldige Einarbeitung in das Thema, die äußerst angenehme und produktive Zusammenarbeit, sowie für die unermüdliche Hilfe bei der Suche nach numerischen Fallstricken,

Dr. Andreas Schweitzer für die zahlreichen kleinen hilfreichen Tipps und die Beseitigung technischer Fallstricke, was zu etlicher Zeitersparnis führte und natürlich für den Meinungsaustausch in Sachen Musik und Computertechnologie,

meinem Bürokollegen, Dipl.-Phys. Ansgar Gaedke, für die sehr angenehme und arbeitsfördernde Atmosphäre,

Dipl.-Phys. Sebastian Knop und Dipl.-Phys. Daan van Rossum für den Wissensaustausch an der weißen Tafel,

den Mitarbeiterinnen und Mitarbeitern der Sternwarte im Hauptgebäude für die Bewältigung bürokratischer Hürden und ihrer tatkräftigen organisatorischen Unterstützung,

den Teilnehmern der regelmäßigen *Physikertreffen*,

Dipl.-Ing. Fabian Wenzel für den interdisziplinären Erfahrungsaustausch,

Dipl.-Phys. Christine Johnas für die zahlreichen Fragen, Beratungen und Gespräche, sowie für die Hilfe und moralische Unterstützung,

meinen Eltern für ihre vielseitige Unterstützung und das Mitfiebern in der Endphase.

Diese Arbeit wurde von der Deutschen Forschungsgemeinschaft als Projekt DFG Ha 3457/3-1 gefördert.